Spin waves with high energy and momentum in ultrathin Co-films studied by spin-polarized electron energy loss spectroscopy

Dissertation

zur Erlangung des akademischen Grades

doctor rerum naturalium (Dr. rer. nat.)

vorgelegt der

Mathematisch-Naturwissenschaftlich-Technischen Fakultät
(mathematisch-naturwissenschaftlicher Bereich)
der Martin-Luther-Universität Halle-Wittenberg

von Herrn Markus Etzkorn
geb. am: 07. November 1975 in: Bonn

Gutachter

1. Prof. Dr. J. Kirschner

2. Prof. Dr. W. Widdra

3. Prof. Dr. C. Back

Halle (Saale), den 31.1.2005

Contents

Chapter 1

Introduction

In the last decades, magnetism at surfaces and in thin films has attracted great attention. Here, the magnetic as well as other properties of materials have been found to often differ quantitatively and sometimes even qualitatively from their bulk counterparts. These studies are of fundamental interest and some discoveries led to important applications now used in every days life, e.g. magneto-resistance phenomena [1–3] used in data storage. Most of the studies have focused on static magnetism but recently also the dynamics receives a growing interest. For the magnetization dynamics the collective magnetic excitations, called spin waves, are of major importance. These excitations are quasi-particles which have a magnetic moment, a wave vector, and an energy. The latter two are linked together by a characteristic dispersion relation. Spin waves have been studied with several experimental techniques, each having certain strengths and weaknesses. The regions in energy/wave vector/thickness-space that are accessible by established techniques are shown in Fig. 1.1 as colored areas. Spin waves in thin ferromagnetic films have been studied by ferromagnetic resonance (FMR), Brillouin light scattering (BLS) and also by time domain methods [4]. All these methods have in common that only long wavelength spin waves can be studied, having a wave vector of the order of 10^{-2}Å^{-1}, at most (dark and light green areas in Fig. 1.1). High wave vector spin waves can be investigated by inelastic neutron scattering (blue area) [5], but the weak interaction of neutrons with matter prohibits measurements on ultrathin films or at surfaces [6]. Due to the limitation of the established techniques, spin waves in about 99% of the Brillouin zone in ultrathin films remained unexplored experimentally (Fig. 1.1). This region is, however, of high interest because here the wavelength of spin waves is of the order of atomic distances. Thus, their study allows direct access to magnetic properties on the atomic scale. This region is also interesting from a theoretical point of view. While, low wave vector spin waves can be described in a macroscopic, phenomenological theory, high wave vector spin waves need a microscopic treatment of the solid. So far, no experimental technique has been available to test the validity of such theoretical calculations in thin films.

In this work, spin-polarized electron energy loss spectroscopy (SPEELS) is introduced as a suitable technique to access the "terra incognita" presented in Fig. 1.1. In the experiment, a monochromatic, spin-polarized electron beam is scattered inelastically from
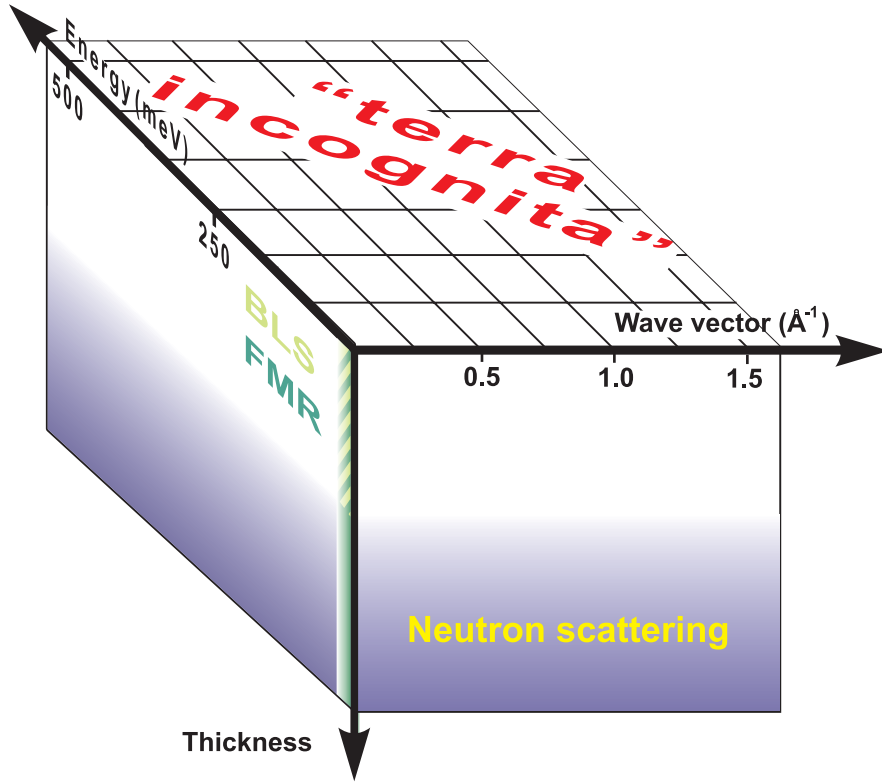
Figure 1.1: Schema of the regions in wave vector/energy/thickness-space in which spin waves have been studied using established experimental techniques (marked by color). Non of these techniques has been able to measure high wave vector spin waves in a single thin film or at surfaces, i.e. in the "terra incognita".

a magnetized sample and the scattered electrons are analyzed with respect to their wave vector and energy transfer during scattering. The use of electrons as scattering particles has certain merits. Because of the strong interaction between low energy electrons and matter, electron scattering is highly surface sensitive. This has been used for several decades in many surface sensitive techniques [7]. In addition, electron scattering is known for the relative easy realization of high energy and high wave vector transfers. This is because of the favorable relation between energy and momentum of a free electron. Thus, the basic idea to study spin waves by electron scattering is evident and it has been proposed already about half a century ago [8]. For decades, attempts have been made by several groups to accomplish such an experiment [9]. Only recently, a first signature of spin waves has been found in SPEEL-spectra [10]. This experiment has led to the study presented in the following. First well resolved, dispersive spin wave losses obtained by inelastic electron scattering are reported in this work. We are presently able to study spin wave excitations with wave vector transfers up to (and beyond) the surface Brillouin zone boundary on films as thin as 2.5 atomic layers. From the signal to noise ratio one could speculate that the sensitivity limit for the detection of spin waves by SPEELS lies far below

this thickness. Up to now, several systems have been investigated by SPEELS [11–15]. In this work, the focus lies on the investigation of spin waves in Co-films. The spin waves are studied in two crystallographic Co structures, fcc Co and hcp Co, stabilized by the substrates Cu(001) and W(110), respectively.

The work is organized as follows. In chapter 2, an introduction to magnetic excitations is given focusing on spin waves and their theoretical description. This chapter also includes an overview of different experimental techniques used to study spin waves and a short introduction into electron scattering. The experimental set-up, especially the SPEEL-spectrometer and its components, is described in chapter 3. In chapter 4, the main experimental results of our investigation of spin waves by SPEELS are presented which are discussed in chapter 5. Here, the experimental findings are also compared to results obtained in other experimental and theoretical studies.

Chapter 2

Magnetic excitations and electron scattering

This chapter is divided into two parts. In the first section, a short introduction to different kinds of interactions between magnetic moments in solids is given. These interactions govern the statics as well as the dynamics of magnetic systems. The dynamics is determined by different magnetic excitations. The theoretical description of these will focus on the collective excitations, i.e. spin waves, since these are the subject of this work. The second part of the chapter gives an overview of different existing experimental techniques that allow the investigation of magnetic excitations and a summary of the main results obtained from these studies. The chapter ends with a brief introduction into electron scattering.

2.1   Interactions of spins in solids

In this thesis, we concentrate our study on Co, a 3d-metal in which the orbital contributions to the magnetic moments are strongly quenched by the crystalline field [16]. Thus, the magnetic moments are dominated by the contribution of the electron spin. Therefore, in the following we consider the spin moment, only.

   A spin has a projection of its magnetic moment along one direction (chosen as z) of size $\vec{\mu}_{\mathrm{S}} = -\mathrm{g}\mu_{\mathrm{B}}\mathrm{S}_{\mathrm{z}}$, with g the gyromagnetic ratio, μ_{B} the Bohr magneton, and $\mathrm{S}_{\mathrm{z}} = \pm\frac{1}{2}$. The magnetic moment feels an external magnetic field $\vec{\mathrm{B}}$ via the Zeeman term $\mathrm{H}_Z = \mathrm{g}\mu_{\mathrm{B}}\mathrm{S}_{\mathrm{z}}\vec{\mathrm{B}}$. Since a spin itself produces a dipolar magnetic field, two spins couple by a dipole-dipole interaction. These interactions range over long distances, but they are relatively weak. In typical cases, they lead to magnetic order at temperatures below 1 K [17]. Since magnetic order is also observed at much higher temperatures, a stronger interaction between spins has to be present. It was discovered by Heisenberg that the strong interaction between spins is caused by the exchange interaction, which is of quantum mechanical origin [18]. The exchange interaction is a consequence of the Pauli exclusion principle and the fact that electrons are indistinguishable. The combination of these two principles leads to the

necessity that the total wave function of a two electron system has to be antisymmetric under the exchange of the two electrons. Therefore, the symmetry of the wave function in spin space effects the real space and vise versa. Since electrons are charged particles, it might be energetically more favorable to have an antisymmetric wave function in real space. The Coulomb interaction then favors a parallel alignment of the spins. Because the driving force is the strong electrostatic force rather than a weak direct spin-spin interaction, the exchange interaction can lead to relatively high ordering temperatures. The exchange interaction is based on the possibility that two electrons can physically exchange, which requires an overlap of the electron wave functions. Therefore, though the exchange interaction is strong, it is of short range. In a localized moment picture, it can be described by the Heisenberg Hamiltonian:

$$H = -\sum_{ij} J_{ij} \vec{S}_i \cdot \vec{S}_j. \tag{2.1}$$

Here, J_{ij} is the exchange coupling constant between the spins $\vec{S}_i$ and $\vec{S}_j$. The definition is such that ferromagnetic order is supported for $J_{ij} > 0$. This model has the advantage that it explains all kinds of magnetic order in a natural way. It is successfully applied in several magnetic systems for example in rare earth elements. Due to the localized moment description it is, however, at best a crude approximation in the case of magnetic 3d-metals. We come back to this point in section 2.2.2.

Another interaction is the spin-orbit interaction. It leads to a coupling of the spin moment to the crystal lattice. The interaction is a relativistic effect and typically small in 3d-metals. Nevertheless, it gives rise to for example the magnetocrystalline anisotropy, so that magnetic moments in a ferromagnet prefer to arrange in certain crystallographic directions.

2.2   Theoretical description of magnetic excitations

Magnetic excitations are either of single particle or collective character. In the localized moment picture, a flip of the direction of a single spin costs the full exchange energy for each surrounding neighbor, as can be seen from equation 2.1. As will be shown later, collective excitations can exist at significantly lower energies. Therefore, these spin waves play an important role for example for the thermodynamic properties of magnets.

Spin waves are quantized. In literature a quantum is often called magnon, however, throughout this work the term spin wave will be used. Spin waves are quasi-particles which carry a wave vector $\vec{q}$, an energy E and a magnetic moment of $1g\mu_B$. In a simple picture, a spin wave can be considered as a quantum of spin reversal spread coherently over the whole crystal [19]. This can be illustrated in a classical, localized moment picture as sketched in Fig. 2.1. Each spin is slightly canted out of its equilibrium position and precesses around this position. Neighboring spins have a fixed phase relation in the precession, which is determined by the wave vector of the spin wave. Spin waves have a characteristic dispersion, which links their energy to their wave vector. Depending
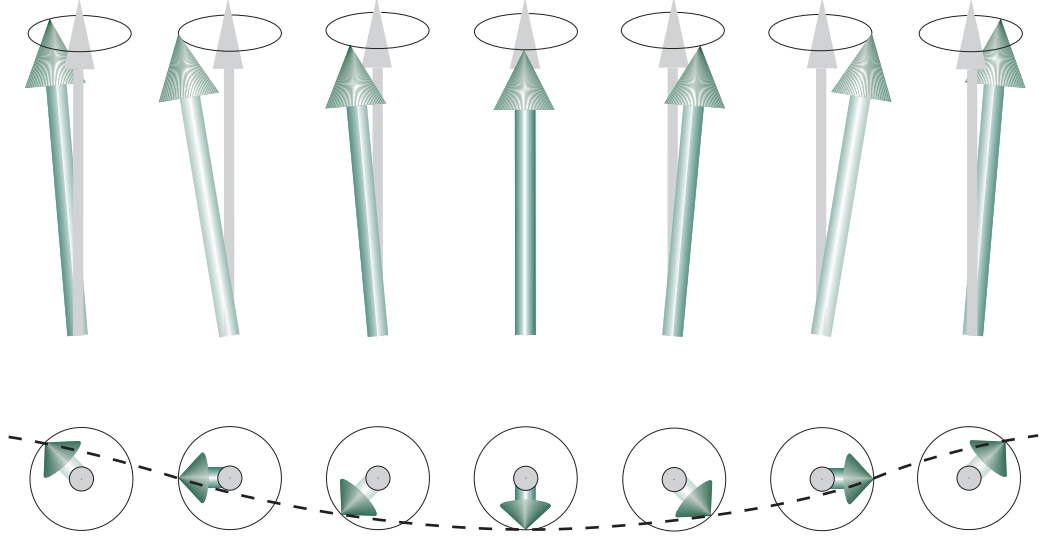
Figure 2.1: Side and top view of a spin wave in a simple classical picture. Each spin is slightly tilted out of its equilibrium position and rotates around this position. The wave vector of the spin wave determines the phase relation between neighboring spins. This leads to the wave like modulation visible in the top view.

on the wave vector, different magnetic interactions determine the spin wave energy. As discussed above, the exchange interaction is typically much stronger than other magnetic interactions. Nevertheless, due to its relatively short range other interactions, like the long ranged dipole-interaction, can become important at sufficiently small wave vectors. As a rule of thumb, in 3d-ferromagnets one is in this so called dipole regime for wave vectors below $q < 10^{-3} \text{Å}^{-1}$ [19]. For wave vectors above $q > 10^{-2} \text{Å}^{-1}$, the exchange interaction can be safely assumed to be the only interaction that determines the spin wave energy [19].

For the different regimes, different theoretical approaches are used to describe spin waves. For the dipole or small wave vector regime, a macroscopic continuum model description is sufficient [17]. Due to the macroscopic quantities involved, the microscopic details of the system under investigation are rather irrelevant. Contrary to this, a true microscopical description is needed in the exchange dominated regime, where the wavelength can become comparable to the atomic distances in a crystal. As will be shown later, the spin waves investigated in this work are solely exchange dominated. The following discussion thus concentrates on theoretical descriptions of this regime. Two different approaches have been developed: The Heisenberg model, in which localized magnetic moments are assumed and an itinerant electron model, where the moments are carried by delocalized electrons. These are the two extreme cases since in the former model the electrons are localized in real space, while in the latter they are localized in reciprocal space. Measurements of high wave vector spin waves provide the possibility to test the accuracy of the theoretical models, since these spin waves are sensitive to details of the

underlying description [20].

2.2.1   Spin waves within the Heisenberg description

For the moment, we stay in the localized magnetic moment description. This picture is not expected to be truly valid for the mobile conduction electrons which carry the magnetic moments in Co, however, it provides a simple description of the underlying physical properties. We will use the Heisenberg model later several times, for example to calculate spin wave dispersions. Therefore, an example for the derivation of the spin wave dispersion within a nearest neighbor Heisenberg model is given in the following.

It was found by Bloch that the Heisenberg Hamiltonian (equation 2.1) allows low energy collective excitations of spins [21, 22]. Considering these collective excitations Bloch could explain the well known $T^{\frac{3}{2}}$-law of the variation of the magnetization at low temperatures. A quantum mechanical description of spin waves within the Heisenberg model can be found for example in Ref. [23]. It is, however, rather technical and a classical solution of the problem yields exactly the same result. In the following, we therefore stay within the classical description. To simplify the calculations, we consider only nearest neighbor interactions and an exchange coupling constant that is the same in the entire system. Thus, the sum in equation 2.1 runs only over nearest neighbors and $J_{ij} = J$. For a magnetic moment $\vec{\mu}_i$ at position i one can write the exchange interaction of each of its neighbor j as an effective magnetic field $\vec{B}_{ij}$ of the size

$$\vec{B}_{ij} = -\frac{2J}{g\mu_B}\vec{S}_j \tag{2.2}$$

acting on $\vec{\mu}_i$ [16].[1] The sum of the torques $\sum_j \vec{\mu}_i \times \vec{B}_{ij}$ defines the rate of change of the angular momentum $\hbar\vec{S}_i$:

$$\hbar\frac{d\vec{S}_i}{dt} = -g\mu_B \sum_j \vec{S}_i \times \vec{B}_i = 2J \sum_j \vec{S}_i \times \vec{S}_j \tag{2.3}$$

and thus for each component:

$$\hbar\frac{dS_i^x}{dt} = 2J \sum_j [S_i^y S_j^z - S_j^y S_i^z] \tag{2.4}$$

and cyclic permutations. We define the direction of the z-axis as parallel to the magnetization axis and allow the magnetic moments to deviate only little from this direction. Therefore, $S^z \approx S$ and $S^x, S^y \ll S$, so that the products of S^x and S^y can be neglected, then

$$\hbar\frac{dS_i^x}{dt} = 2JS \sum_j [S_i^y - S_j^y], \tag{2.5}$$

---

[1]The factor of two results from the fact that the sum in equation 2.1 runs twice over the same pair of spins.

$$\hbar \frac{dS_i^y}{dt} = 2JS \sum_j [S_j^x - S_i^x]. \tag{2.6}$$

The two equations can be decoupled by choosing $S^+ = S^x + iS^y$ and $S^- = S^x - iS^y$. Since both yield the same result, except a time reversal, we treat only S^+ and obtain

$$i\hbar \frac{dS_i^+}{dt} = 2JS \sum_j [S_i^+ - S_j^+]. \tag{2.7}$$

We are later interested in the solution of equation 2.7 in terms of surface spin waves. To derive the dispersion of these spin waves we introduce a surface and make the ansatz $S_i^+ = A_i e^{(i(\vec{Q}_\parallel \vec{R}_i - \omega t))}$. Here, A_i is the amplitude of the spin wave at position $\vec{R}_i$, $\vec{Q}_\parallel$ is the wave vector parallel to a surface, and ω is the angular frequency of the spin wave. Inserting S^+ into equation 2.7 and dividing the result by $e^{(i(\vec{Q}_\parallel \vec{R}_i - \omega t))}$ we obtain

$$\hbar\omega A_i = 2JS \sum_j [A_i - A_j e^{i(\vec{Q}_\parallel(\vec{R}_j - \vec{R}_i))}]. \tag{2.8}$$

Equation 2.8 can be used as a starting point to derive the spin wave dispersion in an arbitrary crystalline structure. Later we will investigate spin waves in thin fcc Co-films. Thus, as a case example, we calculate the spin wave dispersion for an semi-infinite fcc crystal with a (001)-surface. In this crystal, 12 nearest neighbors exist in the bulk at positions $\langle \frac{a_0}{2}, \frac{a_0}{2}, 0 \rangle$, where a_0 is the lattice constant (here, $a_0 = 3.61$ Å^{-1}). At the surface 4 neighbors are missing. $\vec{Q}_\parallel$ is chosen to be along the [110]-direction so that $|\vec{Q}_\parallel| = \sqrt{2}q_x = \sqrt{2}q_y$. The amplitude of the spin waves is constant in each layer and differs only between the layers. Thus, we introduce a layer index n, where n = 1 stands for the surface layer. In this case, we derive from equation 2.8

$$n = 1 : \hbar\omega A_1 = 2JS[8A_1 - 4A_1\cos^2(\vec{Q}_\parallel \frac{a_0}{2\sqrt{2}}) - 4A_2\cos(\vec{Q}_\parallel \frac{a_0}{2\sqrt{2}})], \tag{2.9}$$

$$n > 1 : \hbar\omega A_n = 2JS[12A_n - 4A_n\cos^2(\vec{Q}_\parallel \frac{a_0}{2\sqrt{2}}) - 4A_{n-1}\cos(\vec{Q}_\parallel \frac{a_0}{2\sqrt{2}}) - 4A_{n+1}\cos(\vec{Q}_\parallel \frac{a_0}{2\sqrt{2}})]. \tag{2.10}$$

These equations can be summarized in the form:

$$\begin{pmatrix} a & b & & & 0 \\ b & c & b & & \\ & b & c & b & \\ & & b & c & . \\ & & & . & . & . \\ 0 & & & & . & . \end{pmatrix} \begin{pmatrix} A_1 \\ A_2 \\ A_3 \\ A_4 \\ . \\ . \end{pmatrix} = 0. \tag{2.11}$$

Here, $b = 8JS(\cos(\vec{Q}_\parallel \frac{a_0}{2\sqrt{2}}))$, $c = -\hbar\omega + 8JS[3 - \cos^2(\vec{Q}_\parallel \frac{a_0}{2\sqrt{2}})]$ and $a = c - 8JS$. This system of equations has an infinite set of solutions. One of these solutions is a surface

spin wave mode, for which the excitation amplitude decays exponentially into the bulk, $A_{n+1} = A_n e^{-\alpha \frac{a_0}{2}}$. The other solutions are bulk spin wave modes, here $A_{n+1} = A_n e^{i(\vec{q}_\perp \frac{a_0}{2})}$, where $\vec{q}_\perp$ is the wave vector perpendicular to the surface. Let us consider the solution of the bulk modes first, here

$$\hbar\omega = 8JS[3 - \cos^2(\vec{Q}_\parallel \frac{a_0}{2\sqrt{2}}) - 2\cos(\vec{Q}_\parallel \frac{a_0}{2\sqrt{2}})\cos(\vec{q}_\perp \frac{a_0}{2})]. \qquad (2.12)$$

For a semi-infinite system, one thus obtains a continuum of bulk modes for each given $Q_\parallel$. In contrast, for the surface mode one obtains

$$n = 1 : \hbar\omega = 8JS[2 - \cos^2(\vec{Q}_\parallel \frac{a_0}{2\sqrt{2}}) - e^{-\alpha \frac{a_0}{2}}\cos(\vec{Q}_\parallel \frac{a_0}{2\sqrt{2}})], \qquad (2.13)$$

$$n > 1 : \hbar\omega = 8JS[3 - \cos^2(\vec{Q}_\parallel \frac{a_0}{2\sqrt{2}}) - e^{-\alpha \frac{a_0}{2}}\cos(\vec{Q}_\parallel \frac{a_0}{2\sqrt{2}}) - e^{\alpha \frac{a_0}{2}}\cos(\vec{Q}_\parallel \frac{a_0}{2\sqrt{2}})]. \qquad (2.14)$$

Inserting these two equation into each other, one can determine the decay factor

$$e^{-\alpha \frac{a_0}{2}} = \cos(\vec{Q}_\parallel \frac{a_0}{2\sqrt{2}}). \qquad (2.15)$$

Note that the decay factor depends on $\vec{Q}_\parallel$. Thus, the surface localization increases with $\vec{Q}_\parallel$ and the highest localization is reached at the surface Brillouin zone boundary. The spin wave dispersion for the surface mode is given by

$$\hbar\omega = 8JS[2 - 2\cos^2(\vec{Q}_\parallel \frac{a_0}{2\sqrt{2}})] = 8JS[1 - \cos(\vec{Q}_\parallel \frac{a_0}{\sqrt{2}})]. \qquad (2.16)$$

In the experiments shown later, the films under investigation were only a few atomic layers thick. This can be taken into account in the theoretical description by introducing a second surface. Then, the crystal consists of a slab of n-layers and the matrix given in equation 2.11 contains n rows only. In this case both, the upper left and the lower right corner of the matrix have the entry a. From this $(n \times n)$-matrix n discrete spin wave modes result, two of which are surface modes. These two modes correspond to the in-phase and out-of-phase precession of the magnetic moments in the two surface layers. An analytical solution of a slab which consists of more than 3 layers is tedious, but a numerical solution is relatively simple. The results of the above calculations for a fcc Co semi-infinite crystal as well as for an 8 ML slab are shown in Fig. 2.2 a). In Fig. 2.2 b) the dispersions obtained from similar calculations for hcp Co are presented, since this system is also under investigation later. The only degree of freedom in these calculations is the value of JS. For the two dispersions shown, we have chosen JS = 15 meV. The gray regions in Fig. 2.2 illustrate the continuum of bulk modes allowed for each $\vec{Q}_\parallel$. The eight dispersions of the spin waves in the slab are represented by solid lines. The two surface modes of the slab calculations are the lowest energy branches of the slab system. The surface mode for the semi-infinite crystal lies almost exactly on top of the surface mode of the slab and is therefore not shown here. Noticeable differences in the dispersion of the surface mode of a semi-infinite crystal and a slab occur only for very thin slabs.
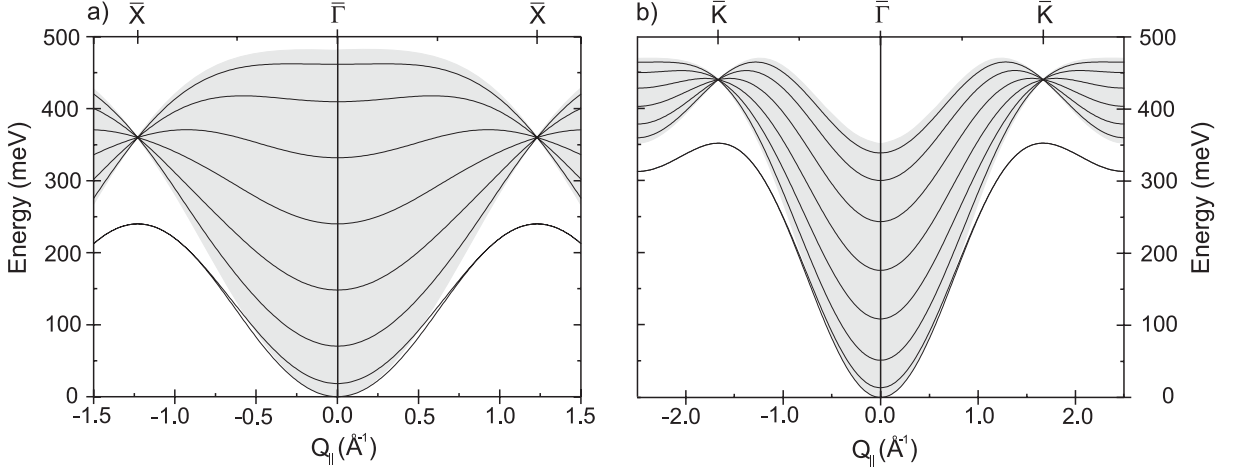
Figure 2.2: Spin wave dispersions calculated within a nearest neighbor Heisenberg model as a function of $\vec{Q}_\parallel$ for an 8 ML slab and a semi-infinite crystal. In a) calculations have been performed for a fcc crystal with a (001)-surface and in b) for a hcp crystal with a (0001)-surface [24]. In these calculations JS = 15 meV. The symbols on the top axis mark the important points in the surface Brillouin zone. The systems presented in the figure correspond to the systems under investigation in this work (see chapter 4).

Like other surface excitations, surface spin waves can only exist as unperturbed modes, when no bulk mode is present at the same point in wave vector and energy space [17]. In principle, surface spin waves for a given wave vector can lie at higher or lower energies compared to the bulk spin waves, several cases are for example discussed in Ref. [25]. Using the simple argument of the reduced number of neighbors at the surface, one would expect that the surface mode lies below the bulk modes for exchange dominated spin waves, as in the above case.

Several interesting, characteristic properties of spin wave dispersions are included in Fig. 2.2. For example, for one spin wave branch the spin wave energy goes to zero for vanishing wave vector. This branch is called acoustic branch. For all other modes, the magnetic moments in some layers process in an out-of-phase condition compared to the magnetic moments in other layers. Therefore, these modes always have a finite spin wave energy, even at $\vec{Q}_\parallel = 0$. They are referred to as optical modes.

The spin wave energy of the acoustic branch at small wave vectors can be approximated by

$$\hbar\omega = 4JSa^2\vec{Q}_\parallel^2 = D\vec{Q}_\parallel^2. \tag{2.17}$$

Here, a is the nearest neighbor distance and D is the so called spin wave stiffness. In many experiments, the wave vector transfer is limited to small values so that equation 2.17 is valid. In these cases, the quantity published in literature is typically the spin wave stiffness.

The Heisenberg model is valuable, especially due to its simplicity. It has already been mentioned that it is not expected to be applicable to an itinerant electron system

like Co. Nevertheless, we will see in chapter 4 that several of our results are described surprisingly well by this model. Other findings, however, can only be understood in an itinerant electron description. Therefore in the following, an introduction into magnetic excitations in an itinerant electron model is given, with emphasis on the differences to the above mentioned results.

2.2.2 Magnetic excitations in itinerant electron ferromagnets

In the 3d-magnetic metals, the conduction electrons that are the carriers of magnetic moments have to be considered as freely moving in a periodic potential. This leads to a description of electrons which are arranged in bands. Each electron is located in k-space rather than at a particular position in the crystal. The successful discussion of magnetism in such itinerant electron systems goes back to Stoner [26, 27]. Under certain circumstances, called Stoner criterium, it is energetically favorable to arrange itinerant electrons in exchange split and not in spin degenerated bands. This results in a higher occupation of states for electrons of one spin direction (majority electrons) compared to the other spin direction (minority electrons). Thus, part of the spin moments are uncompensated and the system is magnetic. The interaction responsible for the magnetic order is again the exchange interaction. The Stoner criterium is fulfilled for Fe, Co and Ni, which explains why these elements order ferromagnetically, while other 3d-metals do not. The Stoner theory also explains the non integer value of magnetic moments per atom in these elements in a natural way.

A draw back of this theory is that the ordering temperature is overestimated by at least half an order of magnitude [28]. The magnetic excitations allowed in the model are the so called Stoner excitations. In these excitations, an electron of a given spin hops from an occupied state below the Fermi-energy (E_F) into an empty state above E_F with opposite spin, leaving a hole behind. In the Stoner model, no interaction between the excited electron and the hole is taken into account. This leads to an overestimation of the minimum energy for magnetic excitations which results in an underestimation of the drop of the magnetization with temperature. The consideration of low energy collective excitations within the itinerant electron model are needed to describe the experimentally observed Curie temperatures. Collective excitations were introduced by Slater [29] for an itinerant electron insulator, in which all spins in the system are aligned parallel to each other except one. He found that the lowest energy magnetic excitations of such a system are of collective nature. This state can be described by the superposition of single particle states and represents the correlated motion of the spin-reversed electron and the hole it left in the sea of aligned electrons [30]. The correlated electron hole pair has a spin moment of $1g\mu_B$ and a defined wave vector. It was found that its properties are similar to the spin wave excitations in the localized model [29]. The extension of the model derived by Slater to itinerant metals has been performed by Herring and Kittel [31, 32]. The general finding is that collective excitations exist in an itinerant electron system and that they are identical to the well-defined spin waves in a localized model in the limit of low wave vectors and low energies. For example, in this limit a quadratic dispersion relation
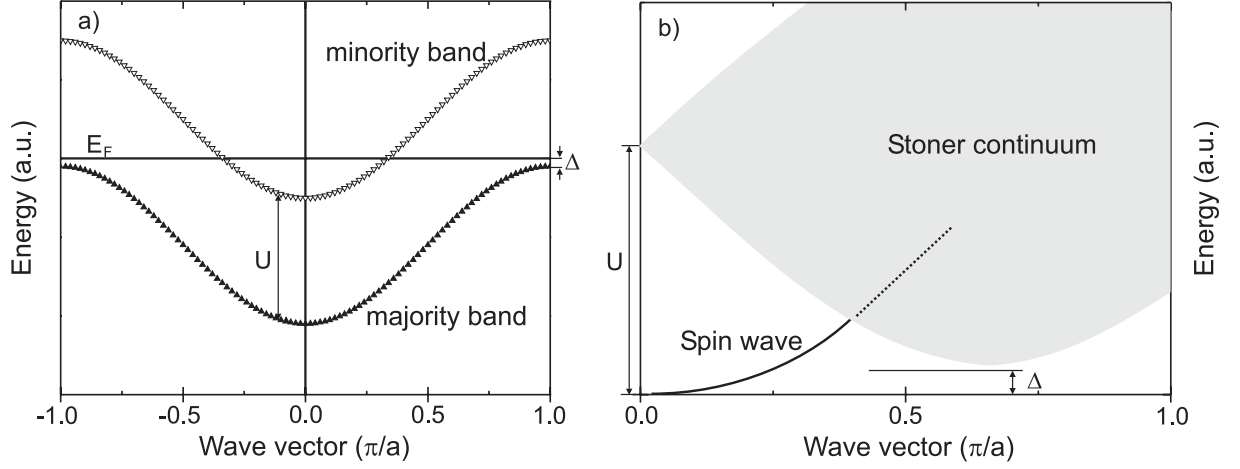
Figure 2.3: a) Pair of exchange split bands with the majority band completely below the Fermi-energy E_F (by the amount Δ) to represent a strong ferromagnet. The exchange splitting parameter U is assumed to be constant in the entire Brillouin zone. In b) the gray region shows the low energy part of the Stoner spectrum calculated for the band shown in a). At q = 0 the creation of a Stoner excitation costs an energy which is equal to U. The minimum energy of the Stoner excitations is equal to Δ and is located at some higher wave vector. To give some general idea, a possible spin wave dispersion is also shown in b). This dispersion was not calculated from the bands shown in a).

of these excitations was found [31, 32], as in the Heisenberg model (see equation 2.17). At high wave vectors and energies, Stoner excitations are possible in the system as well. A correlated electron hole pair that is created in the region where Stoner excitations are possible can easily decay into such uncorrelated states. Therefore, in the region in which Stoner excitations are possible, the collective excitations are not well-defined long living spin waves, but they are strongly damped [33].

The general concept of magnetic excitations in itinerant ferromagnets is summarized in Fig. 2.3. In Fig. 2.3 a) a simple representation of one pair of exchange split bands is presented. The exchange splitting is assumed to be identical to U over the entire wave vector range. The majority band lies completely below E_F to represent a strong ferromagnet. The energy and wave vector transfer needed to excite an electron from an occupied majority state to an unoccupied minority state is shown in Fig. 2.3 b) as a gray area. In this gray area single particle Stoner excitations are possible. For strong ferromagnets, the minimum energy for Stoner excitations is given by the distance between the majority band and E_F, the Stoner gap Δ. For Co, realistic parameters for U and Δ are of the order of 1 eV and 0.2 eV, respectively [34, and references therein]. A possible acoustic spin wave branch is also shown in Fig. 2.3 b) as a black line. When the spin wave branch enters the Stoner continuum it is strongly damped. This range of the dispersion is presented as a dotted line.

The real physical situation is only partly described by Fig. 2.3. For example, realistic band structures consist of more than one band and s-bands of both spin characters cross

the Fermi-edge so that no true overall Stoner gap exists. In our studies, we investigate spin waves at surfaces by electron scattering. In this case, additional effects have to be considered. It has been theoretically predicted that in inelastic electron scattering experiments, the creation of free electron like Stoner excitations is as probable as a creation of d-electron Stoner excitations [35][2]. In addition, at the surface the wave vector perpendicular to the surface is not conserved due to the loss of translational invariance. This leads to drastic changes compared to what has been shown in Fig. 2.3. Even at the small $\vec{Q}_\parallel$ spin waves can decay into Stoner excitations with $\vec{q}_\perp > 0$ [36].

With the advance of theory it became feasible to calculate the above described magnetic excitation spectrum in bulk itinerant ferromagnets on the basis of ab initio calculations [37]. It is, however, computationally too demanding to extent these calculations to surfaces and to thin film systems. Therefore, for thin films two other approaches are used, both starting from an ab initio calculation of the underlying band structure. One frequently used approach is based on the adiabatic approximation, in which the electron motion is decoupled from the spin motion (see for example Ref. [38–44, and references therein]). This means that the damping of spin waves by Stoner excitations is not taken into account. As discussed above, this is a good approximation in itinerant electron systems only in the limit of low wave vector and low energy spin waves. In principle, these calculations map the itinerant ferromagnetism onto a Heisenberg like description. Several publications gave values for the exchange coupling constants derived this way [42, 43, 45].

The other approach goes beyond the adiabatic approximation. This is a non trivial extension of the model using the adiabatic approximation, because one has to take into account the full dynamics of the system [10, 20, 36, 46–54]. This description includes the damping of spin waves caused by Stoner excitations and therefore this theory is expected to be valid throughout the Brillouin zone. The quantity derived in these calculations is the linear response function of magnetic excitations in the solid, the transverse magnetic susceptibility χ. This quantity contains all information, i.e. the dispersion and the spectral weight, of magnetic excitations. In other words, χ assigns an intensity to every point in graph 2.3 b). So far, these calculations were only possible using an empirical tight binding description of the underlying band structure [36, 48, 50, 54].

In a recent series of publications, Mills and coworkers applied this theory to magnetic thin films of Fe, Ni, and Co [10, 20, 36, 50–54]. These calculations showed that the damping of spin waves caused by Stoner excitations is strong in these films. As shown in the last section, within the Heisenberg model one expects as many spin wave modes at a given $\vec{Q}_\parallel$ as layers are contained in the film (see Fig. 2.2). In the itinerant electron theory that goes beyond the adiabatic approximation, this picture changes drastically. Instead of a number of discrete modes each of zero width, the theoretical calculations show only one single broad feature [52, 54]. This arises from the strong damping of the different modes. They overlap and can hardly be distinguished from each other [54].

In this section, two different theoretical concepts of magnetism have been introduced, in which high wave vector spin waves show a different behavior. In the following, we

---

[2]The calculations have been performed for Fe, however, it can be assumed that similar effects may also occur in Co and Ni.

will concentrate on spin waves in Co, in which the electrons have itinerant character. Nevertheless, we will discuss our results to some extent in a nearest neighbor Heisenberg model. Of course, several questions concerning the validity of such a description arise. As discussed above, high wave vector spin waves in this system are expected to be heavily damped. It is expected that this damping influences not only the spectral shape of the spin waves but also effects the dispersion [20]. In addition, in the Heisenberg model rigid magnetic moments are allocated to each lattice point. Thus, the model will break down when changes within the spin density on the atomic scale are significant. Another questionable assumption is that only nearest neighbor interactions are included in our calculations. As will be shown later, it seems possible to take the influence of the above mentioned criticism into account to some extent by an *effective* nearest neighbor exchange coupling constant in the Heisenberg model.

2.3 Established experimental methods to study spin wave excitations

In the following section, different experimental techniques will be introduced which are used to study spin wave excitations. The description is limited to three important techniques: inelastic neutron scattering (INS), Brillouin light scattering (BLS), and ferromagnetic resonance (FMR). The focus lies on INS. The accessible wave vector and energy transfer range in these experiments is similar to the range investigated later in our electron scattering experiments. Findings obtained from all three techniques are compared to our results in section 5.4.

In all scattering techniques (INS, BLS, and SPEELS) the approach to detect spin wave signals is similar. A particle with known energy is scattered under defined conditions from a sample and afterwards is analyzed with respect to its wave vector and energy transfer during scattering. Usually, either the wave vector transfer (constant q-scan) or the energy transfer (constant E-scan) is kept fixed, while the other is varied. These measurements correspond to a scan along a vertical or horizontal line in Fig. 2.2 or Fig. 2.3. Due to energy and momentum conservation laws, the intensity caused by spin wave excitations appear in the scan only at points (in q- and E-space) where the scan line intersects with a branch of a spin wave.

A very important and well established method is INS. For the development of this technique half of the shared Noble prize in 1994 was given to B. N. Brockhouse. By INS spin waves can be studied in a large portion of the Brillouin zone. For high wave vector and high energy transfers, however, these experiments become tedious even with advanced neutron sources. For this reason, only a few INS studies of high wave vector spin waves in 3d-ferromagnets have been performed [55–59]. One general property of neutrons is their weak interaction with matter, which becomes a disadvantage when thin films or surfaces are the subject of interest. While static structural (magnetic) information can be obtained in favorable cases with a possible monolayer sensitivity [60], measurements of spin wave excitations in ultrathin films or at surfaces are practically out of range [6].
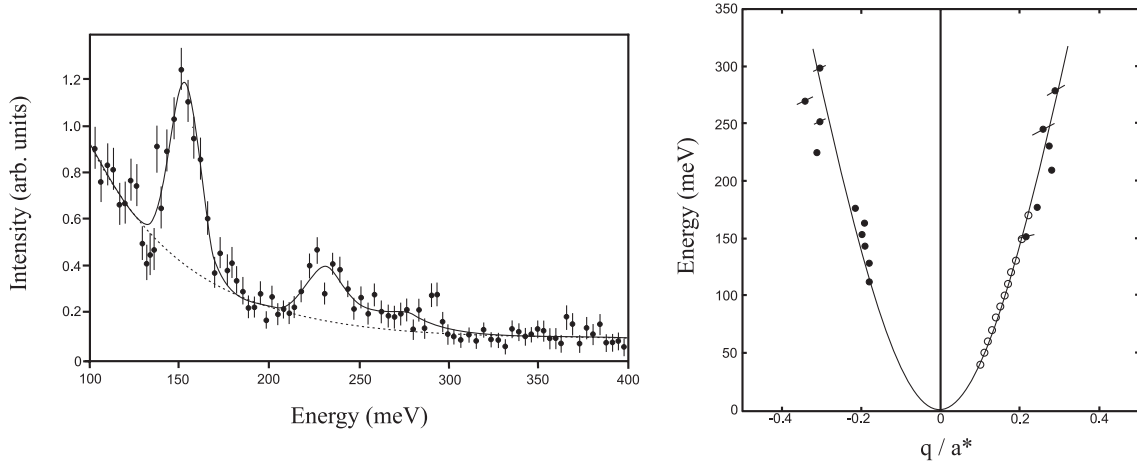
Figure 2.4: Example of recent neutron scattering measurements of spin wave excitations in hcp Co [59]. The left side shows a time-of-flight spectrum, transformed back into energy space, for details see Ref. [59]. On the right side, the resulting spin wave dispersion is shown. The wave vector is normalized in this graph so that the Brillouin zone boundary is at $q/a^* = 0.5$. The solid line is a fit obtained by a nearest neighbor Heisenberg model.

Neutrons scatter from matter mainly because of two interactions of approximately equal strength. Neutrons interact with the atomic nucleus resulting in structural information. This interaction will not be discussed here, since it is not of interest in this work. The second interaction is the dipolar coupling between the spin of the neutron and the magnetic field created by the (uncompensated) electron spins [61]. The creation or annihilation of a spin wave takes place via the coupling of the neutron to the fluctuations of this field [62]. It can be shown that the cross section for magnetic inelastic neutron scattering is directly proportional to the imaginary part of the transverse susceptibility [63–65]. As discussed above, this quantity yields the complete information of the magnetic excitations in the system, the spin wave and Stoner excitations. In neutron experiments, however, the signal obtained from Stoner excitations is weak and due to their broad structure Stoner excitations can typically not be distinguished from the background. The broadening or disappearance of spin waves at higher wave vectors is often interpreted as a sign of the merging of the spin wave branch into the Stoner continuum [55, 66].

A recent example of high wave vector and high energy spin wave excitations investigated by INS is shown in Fig. 2.4 [59]. The experiments were performed on hcp Co using a time-of-flight technique. The peaks visible in the spectrum in Fig. 2.4 a) belong to energy losses caused by spin wave excitations with different wave vector transfers in different Brillouin zones. The information measured in different Brillouin zones can be back folded into the first Brillouin zone. The resulting dispersion relation is shown in Fig. 2.4 b). In these measurements, the dispersion could be followed up to about $\frac{2}{3}$ of the Brillouin zone. The solid line is a fit to the data using a dispersion relation calculated within a nearest neighbor Heisenberg model. A good agreement between the measured dispersion and this model was found [59]. The INS studies showed a broadening of the

spin wave peaks due to itinerant effects. Nevertheless, the spin wave losses were relatively well-defined up to the highest wave vectors investigated.

BLS and FMR are used to study spin waves with long wavelength. Both techniques probe several similar properties of magnetic materials. In FMR the sample is exposed to an alternating magnetic field in the micro wave regime and an additional static magnetic field. Under certain conditions, a coherent procession of the magnetic moments in the system may be possible. This resonant excitation leads to a drop in the reflected or transmitted microwave power. This effect was discovered by Griffiths [67] and explained by Kittel [68]. The spin waves are created by the coupling of the magnetic moments in the solid to the external field [69]. Due to the high index of refraction of metals for micro waves, these waves travel almost perpendicular to the surface and thus, $\vec{Q}_{\parallel} \approx 0$ [70]. BLS exploits the inelastic scattering of light from matter [71]. A photon couples to a spin wave due to the change of the magneto-optical constants in the solid in the presents of a spin wave [72]. Here, mainly the electrical field of the photon couples to the spin wave via the spin-orbit interaction [4]. The first experimental realization of BLS has been performed by Sandercock and Wettling [73]. In BLS, the possible wave vector transfer parallel to the surface is limited by the wave vector of the incident light which is of the order of $\vec{Q}_{\parallel} \approx 10^{-3} \text{Å}^{-1}$.

With the quoted wave vector regime both techniques, BLS and FMR, can determine the macroscopic magnetic quantities of a sample, e. g. the anisotropy. In addition, in both techniques standing spin wave modes perpendicular to the surface have been observed in films with thicknesses of several nanometer or thicker [74, 75]. This leads to the possibility to study spin waves with higher wave vectors, up to $\vec{q}_{\perp} \approx 10^{-2} \text{Å}^{-1}$ [4]. Using these standing modes, the spin wave stiffness of the material can be determined by BLS and FMR. The experiments are typically performed in air, but experiments in ultra high vacuum are also possible. Both techniques can be used to study ultrathin films. The draw back of BLS and FMR is the limitation to small wave vectors.

2.4   Electron scattering

This section gives a brief introduction into electron scattering. The discussion is limited to monochromatic low energy ($\approx$ 10 eV) electrons scattered from crystalline metallic surfaces. Due to the strong interaction of low energy electrons with electrons in the solid, the mean free path is limited to a few atomic layers. Therefore, low energy electrons have a true surface sensitivity. This is the major reason why electrons have been used extensively in almost all kinds of surface studies [7, 76]. The section is divided into two parts. The first part deals with elastic electron scattering and summarizes the interactions between an electron and the matter. The second part treats inelastic scattering focusing on magnetic excitations.
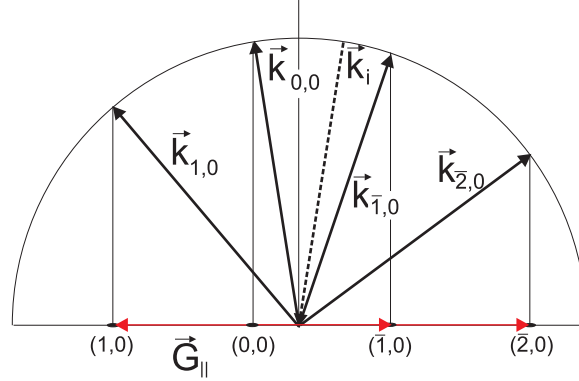
Figure 2.5: The Ewald construction provides a graphical solution to an elastic scattering event on a two dimensional periodic lattice, for which $\vec{K}_\parallel^f = \vec{K}_\parallel^i + \vec{G}_\parallel$. Here, $\vec{K}_\parallel^i$ and $\vec{K}_\parallel^f$ are the wave vector components parallel to the surface of the incident and the outgoing electron, respectively and $\vec{G}_\parallel$ is a reciprocal lattice vector of the two dimensional reciprocal lattice.

2.4.1 Elastic electron scattering

A free electron with a kinetic energy E_{kin} has a wave vector which is given by the de Broglie relation $k = \frac{(2mE_{kin})^{\frac{1}{2}}}{\hbar}$, where m is the electron mass. For example, an electron of a kinetic energy of 10 eV has a wave vector of $k \approx 1.6$ Å^{-1}. This corresponds to a wavelength of $\lambda = \frac{2\pi}{k} \approx 3.9$ Å, which is of the order of a typical lattice constant. Therefore, scattering of electrons from the periodic structure of a crystalline surface results in interference effects. This interference pattern is determined by the arrangement of the atoms at the surface. Due to the limited penetration depth, the scattering electrons mainly experience the lattice periodicity parallel to the surface. For the moment, we assume that the electrons scatter from a perfect two dimensional periodic structure. The two dimensional translational invariance in real space implicates the same invariance in reciprocal space. The resulting structure in reciprocal space is a two dimensional array of rods standing perpendicular to the surface. The distance between the reciprocal lattice rods is given by the two dimensional reciprocal lattice vector $\vec{G}_\parallel$. In a scattering process, the wave vector component parallel to the surface is conserved except for multiples of the reciprocal lattice vector so that the two dimensional Laue condition $\vec{K}_\parallel^f = \vec{K}_\parallel^i + \vec{G}_\parallel$ is fulfilled. Here, $\vec{K}_\parallel^i$ and $\vec{K}_\parallel^f$ are the wave vector components parallel to the surface for the incident and the outgoing beam, respectively. Due to the missing periodicity perpendicular to the surface, the perpendicular wave vector component $\vec{k}_\perp$ of the scattering electron is not conserved. Graphically, this can be illustrated in the Ewald construction [7] shown in Fig. 2.5. At each position where a sphere of radius $|\vec{k}_i|$ cuts one of the reciprocal lattice rods, the diffraction condition is fulfilled. Thus, the positions of the diffraction spots contain information of the underlying lattice. This is for example used in low energy electron diffraction (LEED) measurements.

The translational symmetry in the reciprocal space implies that two points that are

connected by $\vec{G}_{\parallel}$ have the same properties. One can therefore divide the reciprocal space into unit cells, i.e. surface Brillouin zones, which are the complementary structures to the Wigner-Seitz cells in real space [16]. The complete periodic information of the system is contained in each surface Brillouin zone.

The penetration depth of low energy electrons is not limited to the first atomic layer, but extents deeper into the crystal. The exact penetration depth depends on the kinetic energy and the material scattered from as well as possibly on the spin direction of the incoming electrons. The mean free path for Co is about 7 Å (9 Å) for minority (majority) electrons with energies of several eV above the work function [77, 78]. Therefore, the electrons are exposed to the first few repetitions of the periodic structure perpendicular to the surface. This leads to a weakly defined third Laue condition and to a modulation of the intensities along each reciprocal lattice rod [79].

The discussion above was limited to the kinematic approximation, where each electron is scattered only once before it leaves the crystal. As a consequence of the strong interaction of electrons with matter, electrons are, however, on average scattered several times before they leave the crystal. These multiple scattering processes are taken into account in the dynamical scattering theory. The description can be improved by considering the extended charge and spin distribution around each atom, as well as the work function [79]. The scattering of an electron from a crystal is a complicated many-body problem which cannot be solved without any approximations. A natural and quite successful approach is the reduction to an one-particle problem, where the electron is exposed to an effective potential created by all others. The interactions are then represented by the combination of an effective electrostatic and an effective magnetic potential [76, 80].

Typically, by considering only single scattering events, one obtains a rough description of the results of an electron scattering experiment. Of course, this simplified description of the scattering processes cannot provide a quantitative analysis of experimental findings. Nevertheless, in the following our results are mainly discussed within the framework of the kinematic model.

The strong interaction between electrons and matter is mainly caused by the Coulomb interaction which is strong and in principle of long range. When an additional electron is embedded into a metal, it is shielded by the proper arrangement of the surrounding charge. In this case, the Coulomb interaction becomes short ranged. The interaction of the electron spin with the solid consists mainly of two types: the exchange and the spin-orbit interaction. Both interactions have been discussed in a different context in section 2.1. In the scattering terminology these have a slightly different meaning, since here a free electron enters and leaves a crystal. The underlying physical concept, however, stays the same.

The exchange interaction results from the fact that electrons are undistinguishable. The electron detected after a scattering event can either be identical to the incoming electron or this electron can be exchanged with an electron from the solid. In the case that the crystal is a ferromagnet this leads, for example, to polarization effects of the scattered electron beam [76, 81, 82]. The magnetic scattering processes which result from the exchange interaction obey some characteristic symmetry considerations. For example,

the polarization caused by this interaction changes sign when the magnetization of the sample is reversed.

The spin-orbit coupling leads to different scattering potentials for incoming electrons of different spin character, even for non magnetic crystals. The strength of the spin-orbit interaction increases with the atomic number of the atom scattered from. In our SPEELS-experiments, we will see that the spin-orbit coupling can be neglected for Co, whereas for W it is important. The spin-orbit interaction obeys certain symmetry laws, too. For example, the argument of time reversal requires that the interaction changes sign when incoming and outgoing beams are interchanged.

2.4.2 Inelastic electron scattering

When electrons are scattered from a crystal, they may experience inelastic scattering processes. In that case, a transfer of energy and momentum occurred between the incoming electron and the sample. In an inelastic electron scattering event, the total energy and typically also the total wave vector parallel to the surface is conserved in the system, therefore:

$$\begin{aligned} \vec{K}_\parallel^f &= \vec{K}_\parallel^i - \vec{Q}_\parallel + \vec{G}_\parallel, \\ E_{kin}^f &= E_{kin}^i - E. \end{aligned} \qquad (2.18)$$

Here, $\vec{Q}_\parallel$ and E are the wave vector and the energy transferred to the crystal. This energy and momentum are transferred to an excitation in the sample. The quantities that can be measured in our experimental set-up are the wave vector transfer parallel to the surface $\Delta\vec{K}_\parallel$ and the energy loss E_{loss}. Due to the conservation laws given above, these are related to the wave vector and energy transfered to the crystal by $\Delta\vec{K}_\parallel = \vec{K}_\parallel^f - \vec{K}_\parallel^i = -\vec{Q}_\parallel + \vec{G}_\parallel$ and $E_{loss} = E_{kin}^i - E_{kin}^f = E$. The measured scattered intensity as a function of $\Delta\vec{K}_\parallel$ and E_{loss} therefore contains the information of the excitations possible in the sample. This is the general experimental idea, which will be followed throughout the next chapters.

Inelastic electron scattering is divided into the dipolar[3] and the impact scattering regime. In dipolar scattering an electron is scattered from the electric dipolar field which under certain circumstances is created by vibrations of atoms on the surface. Dipolar scattering is typically strong close to the specular condition, in the so called dipolar lope. The high scattering probability in this region is often used in EELS-experiments [83]. Due to the long range interaction of the dipolar field, the scattering typically takes place long before the electron reached the surface. Therefore, it is sufficient to describe this scattering by macroscopic quantities [83]. All experiments presented in the next chapters were obtained at conditions far away from the dipolar lope where this type of scattering is much less important. Therefore, this interaction will not be considered in more details. For impact scattering, as the name suggests, the incoming electron penetrates into the crystal and is scattered by impact. Because of the close distance between the incoming

---

[3]The name dipolar regime might be confusing. Here it refers to electric dipoles not to be mixed with the magnetic dipolar regime in the spin wave description.
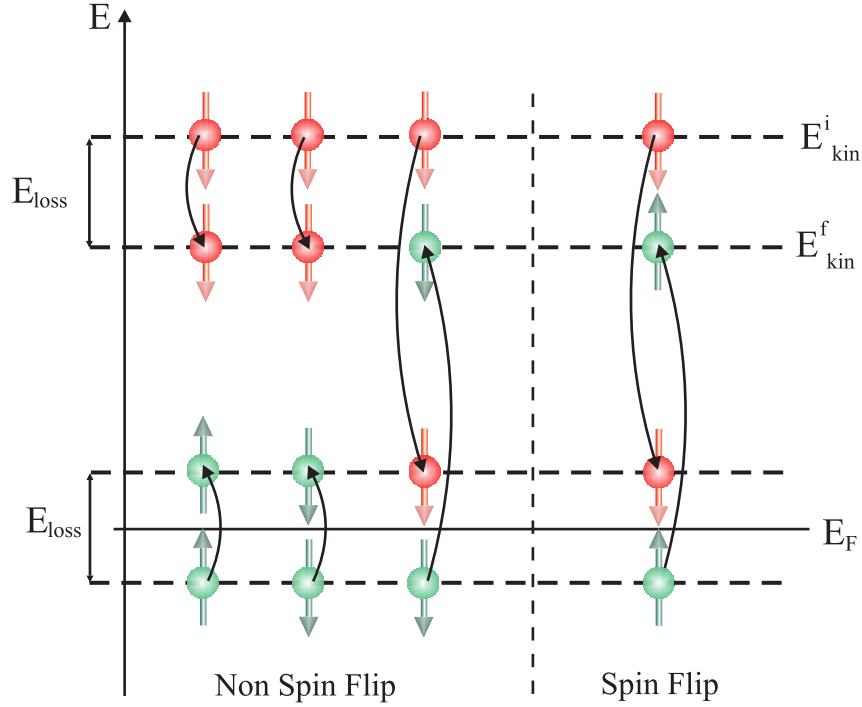
Figure 2.6: Schema of different inelastic exchange scattering processes possible for an incoming $e^\uparrow$-electron. The red electron represents the incoming electron which has an energy E_{kin}^i before the scattering event. The green electron comes from the crystal. E_F and E_{loss} refer to the Fermi-energy and the energy loss in the scattering process, respectively. The electron of the energy $E_{kin}^f = E_{kin}^i - E_{loss}$ is the one that is detected after the event. Note that even in the "spin flip"-channel each electron keeps its spin direction.

electron and the electrons in the sample, exchange processes are possible in the impact regime. In contrast, exchange processes will not take place in dipolar scattering, due to the large distances between the electrons [84]. The description of the impact process demands a truly microscopic model [83]. Although several scattering processes seem to be properly described by such a model, the process of electron scattering by the excitation of a spin wave is not yet understood. Therefore, the following description of magnetic excitations by inelastic electron scattering is phenomenological.

Several excitations of a solid are possible by electron scattering. They can be roughly classified by the energies which are necessary for the excitation. At low energies, the possible excitations are phonon excitations, vibrations of adsorbates on the surface, electron hole pair excitations from conduction band electrons and spin wave excitations. The first three excitations have been studied by EELS for decades, see for example Ref. [83]. The surface sensitivity of EELS, for instance, can be used to study the vibrational excitations of tiny amounts of adsorbates on surfaces. This capability often is a handicap in our experiments, because the measurements require a high cleanliness of the sample surface.

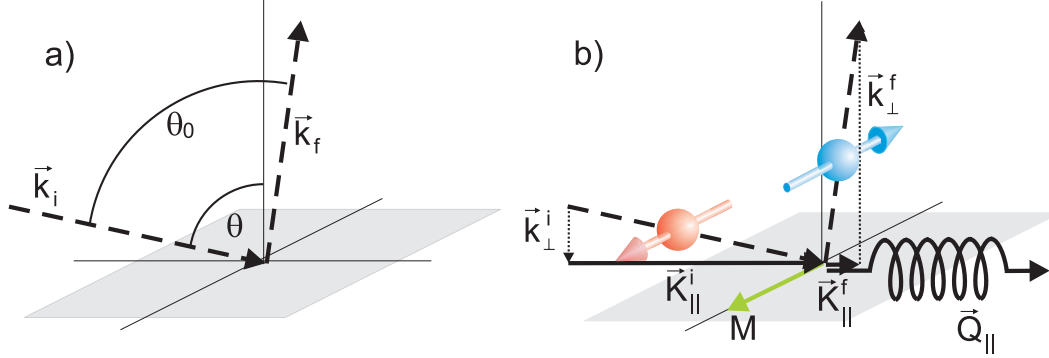Now, we focus on magnetic excitations, the spin waves and the Stoner excitations.

Figure 2.7: a) Illustration of the scattering geometry used in the following. θ_0 defines the angle between the incoming and outgoing electron path. θ is the angle between the surface normal and the incident beam. b) Schematic picture of an electron scattering process in which a spin wave is excited. The wave vector component parallel to the surface is conserved in the scattering process, the component perpendicular to it is not. The creation of a spin wave reduces the magnetization of the sample by $1g\mu_B$. The conservation of the total magnetic moment requires that for the excitation of a spin wave the incoming electron has to be of minority character and the outgoing electron of majority character. Note that by definition the spin and its magnetic moment point into opposite directions.

Beside the conservation of energy and momentum given in equation 2.18 also the total spin moment is conserved during scattering. It is therefore useful to separate the scattering processes in different spin channels defined with respect to the magnetization of the sample. In the following, $e^\uparrow$ ($e^\downarrow$) refers to an incoming electron with a spin moment parallel (anti-parallel) to the spin moment of a majority electron in the solid. Four possible configurations for the outgoing electron exist. The scattered electron can either have the same spin as the incoming electron, marked by $e^{\uparrow\uparrow}$ ($e^{\downarrow\downarrow}$), or can have a reversed spin, $e^{\uparrow\downarrow}$ ($e^{\downarrow\uparrow}$). Due to similarities to polarized neutron scattering, the former two channels are denoted as non spin flip channels and the latter two as spin flip channels. The terms are a bit awkward in electron scattering because in non of the scattering processes discussed here an electron flips its spin. This is illustrated in Fig. 2.6. The scattering process can be a direct scattering process, in which the incoming (red) electron with energy E^i_{kin} is the one that leaves the crystal with energy E^f_{kin} (first two cases in Fig. 2.6). Scattering can also take place in an exchange process where the electron that leaves the crystal is originating from the crystal (green) (third and fourth case in Fig. 2.6). In the latter process, the incoming electron drops into an empty state above E_F and transfers most of its energy to an electron in the crystal. The force acting during this scattering events is the Coulomb force, therefore, each electron keeps its original spin direction. Nevertheless, in the exchange process it is possible that the outgoing electron has the opposite spin compared to the incoming one. From the eye of the beholder, it seems as if the spin of the electron has flipped.

Fig. 2.7 shows a sketch of a possible scattering process in which an electron excites a spin wave. From the geometry defined in Fig. 2.7 a) one obtains

$$-\vec{Q}_{\parallel} + \vec{G}_{\parallel} = \Delta\vec{K}_{\parallel} = \vec{k}_{\mathrm{f}}\sin(\theta_0 - \theta) - \vec{k}_{\mathrm{i}}\sin(\theta). \tag{2.19}$$

In the case presented in Fig. 2.7 b), the excited spin wave is a surface spin wave that has only a wave vector component parallel to the surface. Since the wave vector component perpendicular to the surface is not conserved during the scattering, with the same process sketched in Fig. 2.7 b) also a spin wave with $\vec{q}_{\perp} \neq 0$ could be excited.

Because the total magnetic moment has to be conserved in the scattering process, the excitation of spin waves is only possible in a certain spin channel. In a simple picture, the creation of a spin wave reduces the magnetization of the sample by $1g\mu_{\mathrm{B}}$. To fulfill the conservation law, the creation of a spin wave is thus only possible in the $e^{\downarrow\uparrow}$-channel. Therefore, the incoming electron has to be of $e^{\downarrow}$ (minority) character to be able to excite a spin wave (as indicated in Fig. 2.7 b)). Vice versa, the annihilation of a spin wave is only possible in the $e^{\uparrow\downarrow}$-channel.[4] By this selection rule, spin waves are the only excitations in electron scattering that gives a 100% spin-polarized loss peak. For this reason, it was even suggested to use these excitations as a source of spin-polarized electrons [8]. Though this application seems not promising, the selection rule itself can be used in the experiment to separate spin wave excitations from other excitations. It is sufficient to have a spin-polarized incoming electron beam and a ferromagnetic sample with a defined magnetization direction parallel to the polarization axis. In this particular case, an energy loss caused by the excitation of spin waves is only possible for one spin direction of the incoming electrons. This circumvents the necessity of a "complete" experiment with a spin analysis of the scattered electrons, which is a difficulty in electron scattering experiments due to the notoriously inefficient detectors [85].

Stoner excitations have been extensively studied by SPEELS. First SPEELS-measurements were performed by Hopster (unpolarized incoming electron beam, but spin detector) [82] and Kirschner (exploiting an incoming spin-polarized beam, but no spin detector) [81]. In these measurements, Stoner excitations appear as a broad feature extending from low energies up to several eV. Only little structure as a function of the loss energy has been observed. In most cases, the maximum intensity of the Stoner excitations was found close to the value of the average exchange splitting. Even complete experiments with an incoming spin-polarized electron beam and a spin analysis of the scattered electrons were performed to investigate Stoner excitations [34, 86, 87]. These experiments showed that Stoner excitations are present in both spin flip channels. The excitations had higher intensity for incoming minority electrons. In addition, the non spin flip excitations (simple electron hole pairs) produced a significant amount of the intensity to the spectra. This intensity was found to differ for incoming electrons with majority or minority spin char-

---

[4]The above argument is strictly valid only for zero temperatures and has to break down at T_{C}. In the studies presented in this work, the temperature will be of the order of half T_{C} or lower. At this temperatures, the consideration that the creation of a spin wave is only possible in the $e^{\downarrow\uparrow}$-channel is a good approximation.
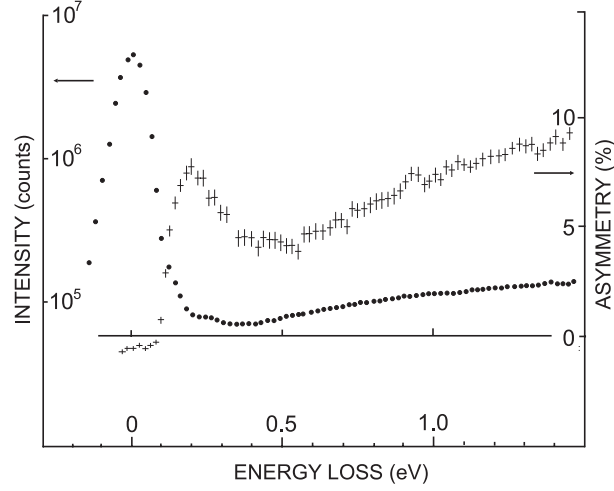
Figure 2.8: First signature of spin waves obtained by SPEELS-measurements. The data are taken from Ref. [90]. The measured intensity is shown as dots. The crosses mark the asymmetry $A = \frac{I^\downarrow - I^\uparrow}{I^\downarrow + I^\uparrow}$. The increase of the asymmetry below 0.4 eV is attributed to spin wave excitations, the increase above 0.5 eV is caused by Stoner excitations.

acter, as well. These effects can be explained by the density of occupied and unoccupied states.

It was shown theoretically that the cross section of Stoner excitations in electron scattering is enhanced compared to neutron scattering [36,50]. It was argued that the response function probed in these two experiments is different because of the different interactions of neutrons and electrons. From the theoretical predictions, both response functions differ mainly in the Stoner contributions and are similar in the spin wave regime [50]. The possible detection of spin waves via inelastic electron scattering was theoretically proposed in the middle of the last century [8]. Several values of the cross section between electrons and spin waves were predicted, see for example Ref. [36,88,89]. The results from these calculations differ significantly. In the latest publication by Mills and colleagues [36], its was estimated that the spin wave intensities in SPEELS should be comparable to the intensity of Stoner excitations. A first experimental signature of spin waves in SPEEL-spectra was found by Kirschner [90]. This result was confirmed by Vernoy and Hopster [91]. In both publications, a spin-polarized incident electron beam was used.[5] The main result of Ref. [90] is shown in Fig. 2.8. A broad maximum, centered around 200 meV, is visible in the asymmetry ($\frac{I^\downarrow - I^\uparrow}{I^\downarrow + I^\uparrow}$) of the two intensities of different incoming electron spin directions. The low energy side of the peak was not resolved due to the limited energy resolution and the study of the spin wave dispersion was not carried out. The possibility to study spin wave excitations by SPEELS, however, was demonstrated in this experiment. In order to explore this possibility in detail, we have undertaken the present study.

---

[5]To discuss the results, we use the same notation that will be used later in our measurements. $I^\uparrow (I^\downarrow)$ denotes the measured intensity for incoming electrons with majority (minority) spin character.

Chapter 3

The experimental set-up

An absolute necessity for surface sensitive experiments is the control of the surface properties and its cleanliness. To meet these prerequisites, the experiments were performed in ultra high vacuum in an apparatus especially designed for this purpose. The spin-polarized electron energy loss spectrometer used for the experiments is introduced in the next section. In addition, a source of spin-polarized electrons is needed. In this work, GaAs-photocathodes were used [92]. The working principle and the preparation of these cathodes are briefly discussed in section 3.2. The sample preparation and characterization is treated at the end of this chapter.

Fig. 3.1 shows an image of the apparatus. The set-up is divided into three chambers. One chamber is used to prepare the GaAs-photocathodes. In another chamber the samples are prepared and characterized. The SPEEL-spectrometer is integrate in the central chamber. The pressure was typically in the low 10^{-11} mbar range in the SPEELS- and GaAs-preparation chamber and in the medium 10^{-11} mbar range in the sample preparation chamber. During the motion of the sample, the cathode, or the analyzer the pressure increased by about one order of magnitude.

In addition to the SPEEL-spectrometer, the vacuum system is equipped with a number of standard in situ preparation and characterization instruments. These are a differentially pumped sputter gun, e-beam assisted ovens for molecular beam epitaxy (MBE), LEED, Auger electron spectroscopy (AES), medium energy (≈ 3 kV) electron diffraction (MEED), a magnetooptical Kerr effect (MOKE) set-up in longitudinal geometry, a mass spectrometer for the analysis of the residual gases, and several leak valves for gases. The methods used to prepare and charaterize the samples are typical for surface science and have been discussed in detail in the literature, see for example Ref. [7, 79, 80, 93].

The sample can be heated by electron bombardment to ≈ 2500 K for a short time or by resistive heating to about 900 K. It can also be cooled by liquid Nitrogen to ≈ 100 K. For the preparation of the GaAs-photocathode, a different manipulator offers resistive heating to about 900 K. The GaAs-preparation chamber is equipped with two Cs-dispensers, a leak valve for O_2-gas and a laser to excite photoelectrons from the cathode.

Sample Preparation chamber   GaAs-Preparation chamber

optical bench   SPEELS-chamber
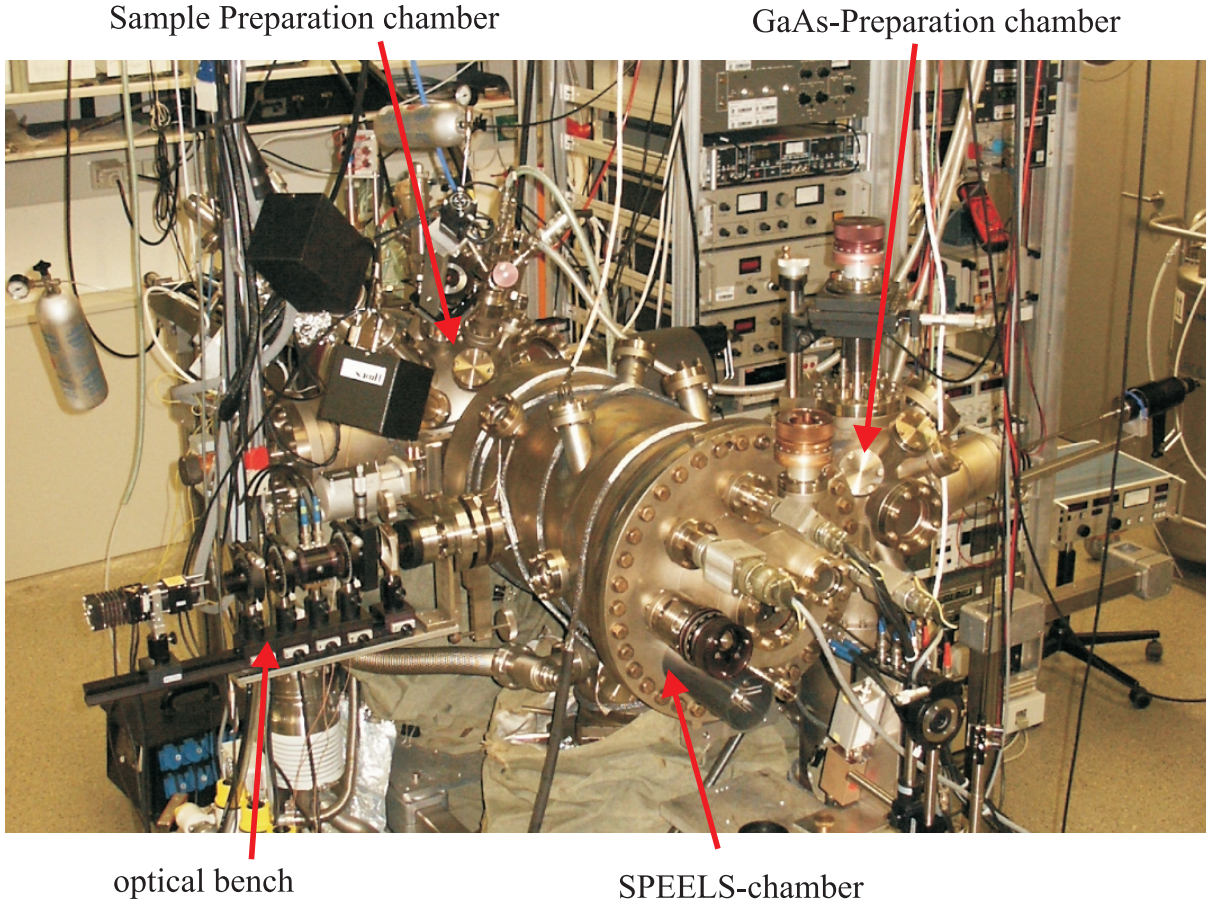
Figure 3.1: Photo of the experimental set-up which consists of three chambers. In the sample and in the GaAs-preparation chamber the sample and the GaAs-photocathodes are prepared and charaterized. For the SPEELS-measurements both are transferred into the SPEELS-chamber. The optical bench holds a laser (wavelength 830 nm) and the optics to create circularly polarized light.

3.1 The spin-polarized electron energy loss spectrometer

In the SPEELS-experiments, spin-polarized electrons are scattered from a sample. The energy and momentum transfer of the scattered electrons is analyzed for the two possible spin directions of the incoming electrons. To realize the experiment, a spin-polarized, monochromatic electron beam is needed that hits the sample under controlled conditions. With the help of an analyzer, the intensity of the scattered electrons in a small window in energy and wave vector space can then be counted. The energy filtering in the monochromators and the analyzer is achieved by using dispersive elements consisting of two curved plates and two slits serving as entrance and exit slit for the electron beam (see Fig. 3.2). Between the curved elements an electrostatic potential is applied. When an electron is
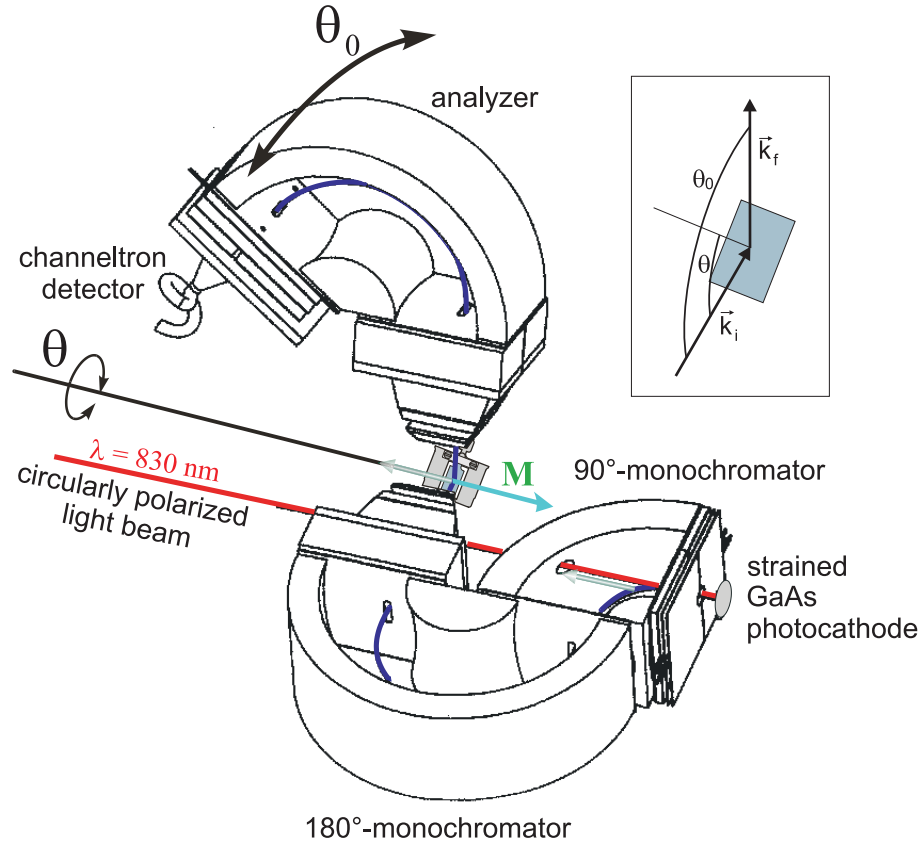
Figure 3.2: Sketch of the spectrometer under operation with a GaAs-photocathode. The circularly polarized light excites a longitudinal spin-polarized electron beam from the cathode (the spin direction is shown by the green arrow). After the electrons have traveled through the electrostatic monochromators, the beam is transversely polarized. Electrons having the proper energy then travel through the analyzer into the detector (the full path is shown in blue). The inset illustrates the definition of the scattering angles θ and θ_0.

traveling from the entrance slit through such a device, it arrives at the exit slit only if it has a certain energy. The energy resolution for a given design of a dispersive element is determined by the kinetic energy of the electrons that are transmitted, the so called pass energy E_{pass}. The energy resolution can, therefore, be changed by applying different potentials to the dispersive elements. This is, however, only possible on the expense of intensity and within certain limits. The dispersive elements also have limited acceptance angles parallel and perpendicular to the dispersive plane. Electrons that enter the device under an angle larger than the acceptance angle are not transmitted. Because of these properties, the dispersive elements are used for both, energy and wave vector filtering.

The spectrometer has been designed by Prof. Ibach for this particular experiment. A sketch of the spectrometer as well as a photo is shown in Fig. 3.2 and Fig. 3.3. The spectrometer consists of three main parts. In the first part, the electron beam is created by either a standard W-filament (unpolarized beam) or a GaAs-photocathode (polarized
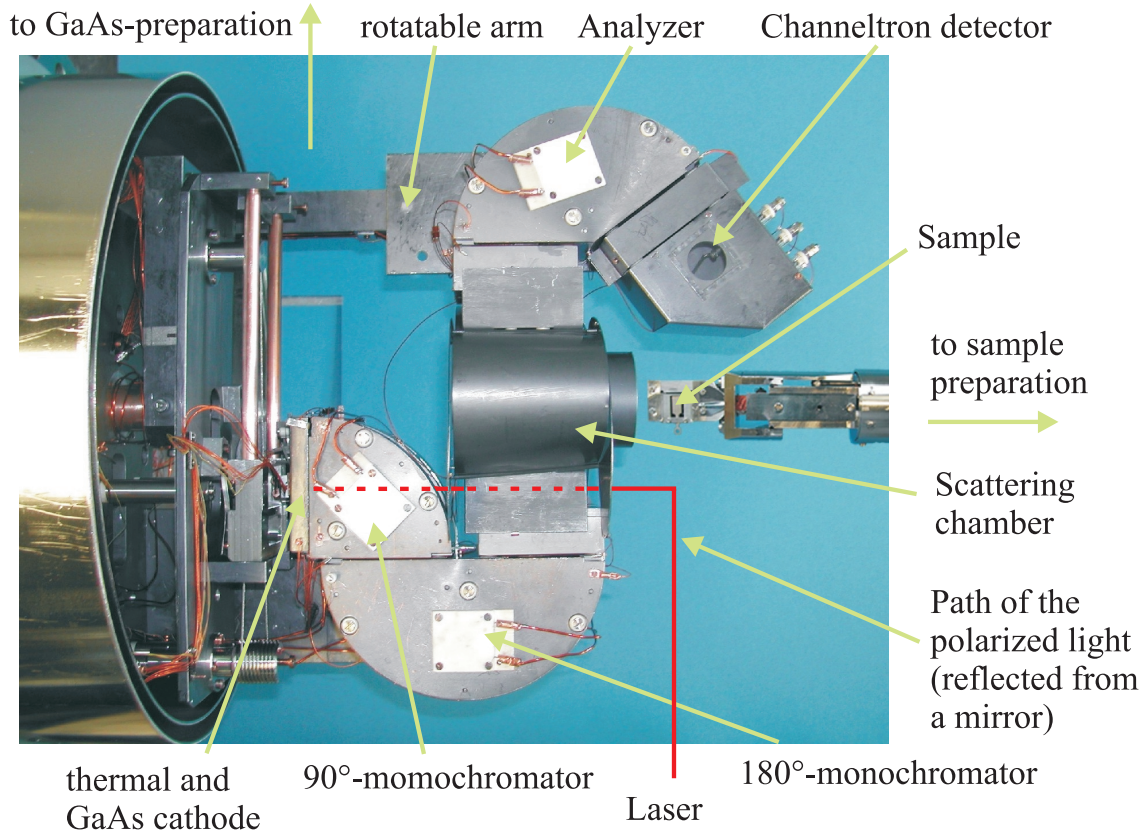
Figure 3.3: Photo of the spectrometer and the head of the manipulator. The main parts are marked with arrows. The complete analyzer and detector unit is mounted on an arm which allows the rotation around the sample position in the scattering chamber. In red, the approximate path of the laser beam to the GaAs-photocathode is shown. The light is reflected from a mirror that is not included in the picture. Both cathodes, a standard W-filament and a GaAs-photocathode, are placed on a slide in order to interchange them and to allow a transfer of the GaAs.

beam). Both cathodes are mounted on a movable slide to allow the transfer of the GaAs-cathode into its preparation chamber and to have the possibility to switch between the two types of cathodes. The second part, the monochromator, consists of a pre-monochromator and a main monochromator with deflection angles of 90° and 180°, respectively. The third part of the spectrometer is the analyzer, which is a standard EELS-monochromator with a deflection angle of 146° [94, 95]. The analyzer and the detector are mounted on an arm so that they can be rotated around the sample position in the scattering plane, as shown in Fig. 3.2. The accessible range of the angle (θ_0) is $80° \leq \theta_0 \leq 280°$. The dimensions and a detailed description of the design of this SPEEL-spectrometer is given in Ref. [96].

The task of the present design is to combine the desired direction of the spins of the electrons at the sample position with the requirements of electron optics to have a sufficiently good performance. One can show that for a dispersive element, as the one used in

this experiment, first order focusing of the electron beam on the exit slit in the dispersion plane is achieved when the total deflection angle is $\approx 146°$ [94, 95]. Monochromators with such an deflection angle have the highest transmission for a given energy resolution. In a spin-polarized EELS one has the additional need to have a defined spin direction of the electrons at the sample position. Typically, a transverse spin-polarized electron beam with the spin direction perpendicular to the scattering plane is preferred. The electron beam that leaves the GaAs-photocathode is longitudinal spin-polarized. The electrostatic potentials do not affect the spin direction. Therefore, the total deflection angle of the monochromator should be an odd multiple of 90°. Without going into details here, it is possible to solve the two contradicting demands partially by combining a 90°- and a 180°-monochromator under certain conditions[1]. For a detailed description of this effect see Ref. [96].

The resulting performance of our spectrometer is shown in Fig. 3.4. The solid symbols are data points obtained with a thermal (blue circles) and a photocathode (red triangles), respectively. The open cycles are taken from the worlds highest performance spectrometer (ULTI100), which was also designed in Jülich [95, 97]. ULTI100 was designed for highest energy resolution, but for an unpolarized electron beam. For the measurements of spin waves, however, high intensities and moderate energy resolution are favorable, because the spin wave signals are expected to be rather weak and intrinsically broad. Therefore, the SPEEL-spectrometer was designed to work with high performance in the energy resolution range between 10-40 meV (full width half maximum (FWHM)). In this working range, the SPEEL-spectrometer matches the performance of ULTI100 with the additional defined spin direction of the electrons at the scattering position.

So far, we have mainly discussed the energy resolution of the spectrometer. The wave vector resolution is of high relevance as well, especially because we are later interested in the dispersion of spin waves. The wave vector resolution is determined by the momentum of the incoming electrons and the angular resolution of the spectrometer. The latter one is defined by the deviations in angle from the nominal scattering conditions under which an electron can be scattered from the sample and is still detected in the channeltron. Along the scattering plane, the angular resolution can be measured by scanning θ through the specular scattering condition. A curve of such a scan performed on W(110) with $\theta_0 = 80°$ and $E_{kin} = 7eV$ is shown in Fig. 3.5. The angular FWHM of the reflected beam is about 2°. The wave vector resolution in the scattering plane depends on the scattering geometry. With the angular resolution shown in Fig. 3.5 and the settings given in the figure caption, one obtains a wave vector resolution in this plane between 0.030 $Å^{-1}$ and 0.040 $Å^{-1}$.

Perpendicular to the scattering plane, our set-up does not allow a direct measurement of the angular resolution. Thus, it has to be calculated. The angular resolution is not determined by the apertures in the scattering chamber, but by the acceptance angle of

---

[1]By applying a bias voltage between the top and the bottom plate of the monochromators the focusing conditions in the dispersion plane change for the monochromators used in this spectrometer. By choosing the proper potentials and dimensions one may obtain focussing at least in the dispersion plane of the monochromators.
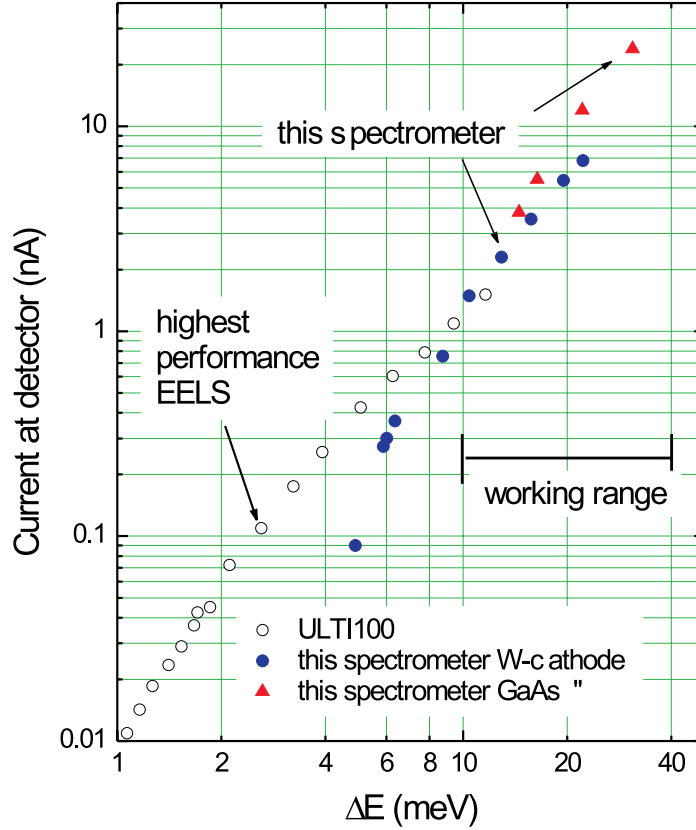
Figure 3.4: Performance of the new SPEEL-spectrometer under thermal and under photocathode operation. The intensities as a function of the energy resolution ΔE (FWHM) is shown for the direct beam configuration ($\theta_0 = 180°$). The open symbols are values of the worlds highest performance EELS, ULTI-100 [95, 97]. The "working range" indicates the energy resolution for which our SPEEL-spectrometer is designed.

the dispersive elements.[2] The total wave vector resolution in this direction, including the monochromator and the analyzer acceptance angle, is about 0.03 Å^{-1} under typical measuring conditions.

In the experiment, the spectrometer was used to measure the intensity of electrons scattered from the sample under a particular angle and with a certain energy transfer. For experimental reasons, the SPEELS-measurements were performed in the "constant q-mode". Thus, a complete loss spectrum was taken for a given wave vector transfer. The energy losses measured in the experiments are small compared to the primary kinetic energy E_{kin}^i of the incoming electrons and hence $k_f \approx k_i$. Therefore, one can approximate $\Delta K_{\parallel} \approx k_i(\sin(\theta_0 - \theta) - \sin(\theta))$. All wave vector transfers mentioned in the following

---

[2]Because the sample and the dispersive elements lie on different potentials, the acceptance angle has to be determined using the Abbe's sine law $\alpha_M y_M \sqrt{E_{pass}} = \alpha_S y_S \sqrt{E_{kin}}$ [83]. Here, α_M and α_S are the acceptance angles of the dispersive element and the angle at the sample, y_M is the dimension of the entrance slit (0,3 mm) and y_S is the beam size at the sample position (about 1 mm).
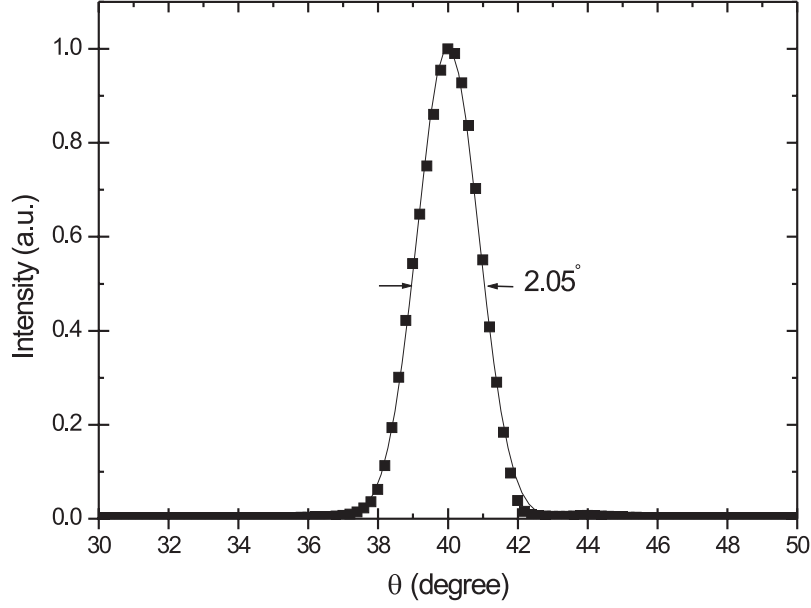
Figure 3.5: Scan of the angle θ over the specular conditions. The beam is reflected from a W(110) crystal with $E_{kin} = 7$eV and $\theta_0 = 80°$. The pass energies of the monochromator and analyzer were about 2.3 eV and 1.2 eV, respectively.

are calculated within this approximation. For the wave vector transfer defined by the scattering geometry, the intensities of the scattered electrons were measured as a function of their energy loss. This was performed by ramping all analyzer potentials while keeping the pass energy constant. The transmitted electrons were counted with a channeltron, working in the single electron counting mode. The SPEEL-spectra shown in the following were recorded by setting a loss energy and then counting the number of electrons scattered under this loss for both possible direction of the incoming electron spins. The number of electrons was counted for one second for both of the incoming spin directions. Then, the analyzer was set to the next loss energy and so on. Once the full spectra was recorded, the measurement was typically repeated several times to give better statistics.

The alignment of the sample to the scattering center was accomplished by optical methods and was crosschecked by measuring the position of diffraction spots. To ensure defined scattering conditions, the difference between the work function of the sample surface and graphite (the surface of the spectrometer) had to be compensated. The work function was measured by detecting the onset of a sample current as a function of the voltage applied to the sample for a fixed incident electron energy. The difference in work functions was corrected by applying an additional voltage to the sample. The measured values of the work function difference are in reasonable agreement with literature values [98–100].
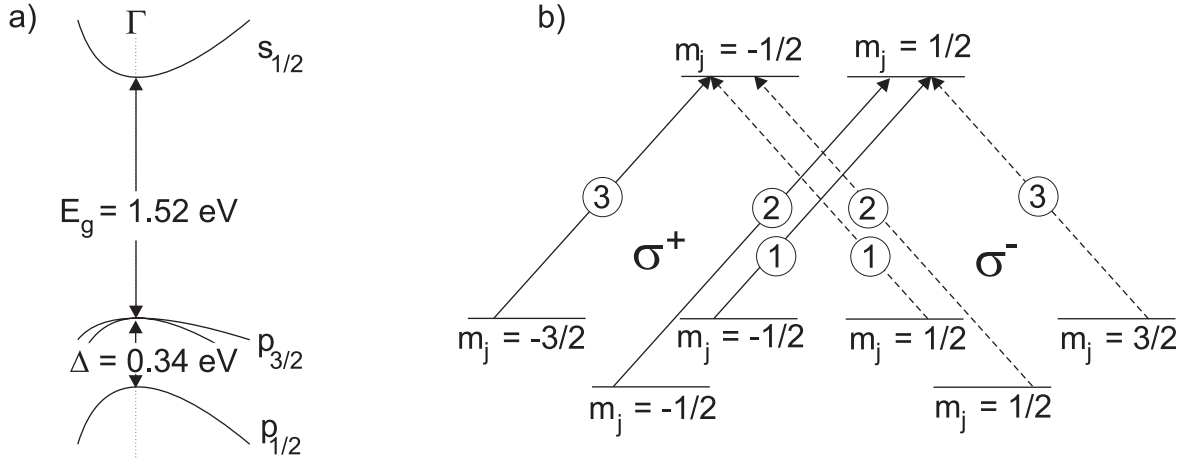
a)

Γ

$s_{1/2}$

$E_g = 1.52$ eV

$\Delta = 0.34$ eV $p_{3/2}$

$p_{1/2}$

b)

$m_j = -1/2$ $m_j = 1/2$

③   ② ②   ③

σ^+ ① ① σ^-

$m_j = -3/2$ $m_j = -1/2$ $m_j = 1/2$ $m_j = 3/2$

$m_j = -1/2$ $m_j = 1/2$

Figure 3.6: a) Schematic diagram of the energy position of the conduction band and the spin-orbit split valance bands for wave vectors close to the origin in GaAs. b) Schema of the energy states for different quantum numbers m_j and the possible transitions for $\sigma^+(\sigma^-)$-circular polarized light, shown as solid (dashed) arrows. The numbers on the arrows mark the relative transition probability. The graph was taken from Ref. [92].

3.2   The GaAs-photocathode

Almost 30 years ago, D. T. Pierce and F. Meier showed that GaAs can be used to create spin-polarized photoelectrons [92]. The underlying physical reason is illustrated in Fig. 3.6 a). Due to the spin-orbit interaction, the GaAs $p_{\frac{1}{2}}$ and $p_{\frac{3}{2}}$-valence bands lie at different energy levels. When illuminating the GaAs with circularly polarized light of the right wavelength, transitions from these bands into the conduction $s_{\frac{1}{2}}$-band are possible (Fig. 3.6 b)). The relative excitation probabilities from the different bands depend on the helicity of the incoming light. The different probabilities are indicated by the numbers on the arrows in Fig. 3.6 b). When the energy of the incident light is tuned close to 1.52 eV, transitions from the $p_{\frac{1}{2}}$-band are not possible anymore. The conduction band will then be populated with more electrons of one spin direction than of the other. The polarization can be defined as P $= \frac{N_\uparrow - N_\downarrow}{N_\uparrow + N_\downarrow}$, where N_i is the number of electrons with spin direction i. The transition probability given in Fig. 3.6 b) yields a polarization of P $= 50\%$. Experimentally, polarizations of 25 to 30% are regularly observed [92]. One way to increase the spin polarization to values higher than 50% is to lift the degeneracy of the two upper valence bands. This is typically done by adding strain to the GaAs-lattice at the surface by growing it epitaxially on the proper substrate [101]. In this way, polarizations of about 90% were experimentally observed [102]. For these strained GaAs the optimum wavelength of the incident light is about 830 nm ($\approx$ 1.49 eV). This cathodes are commercially available [103].

    The occupation of the GaAs-conduction band with electrons of one particular spin direction is one important aspect for the creation of a spin-polarized electron beam, but it is also important to extract these electrons into the vacuum. For a clean GaAs-surface,
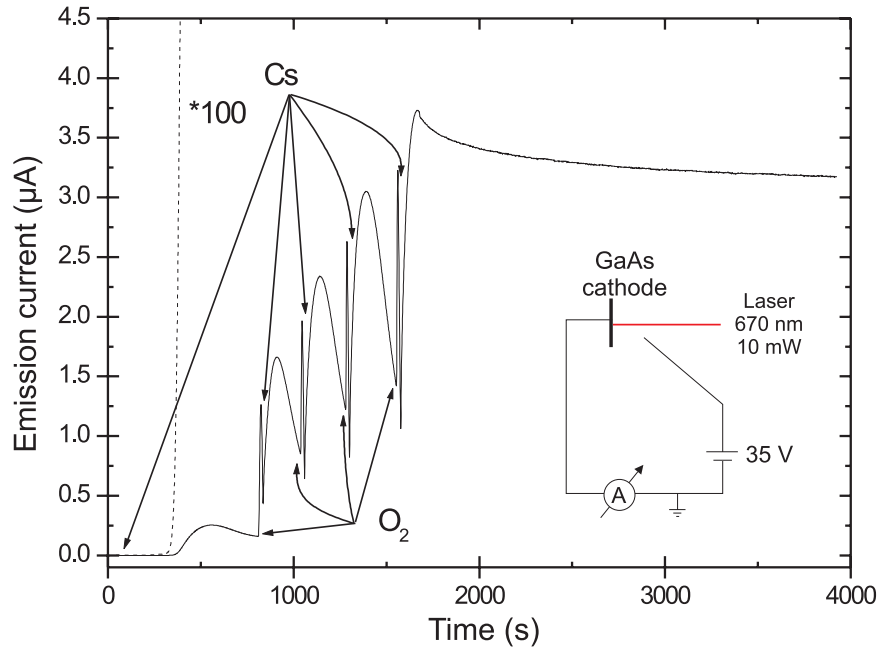
Figure 3.7: Measurement of the photocurrent of a GaAs-cathode during preparation. The arrows mark the points at which Cs- or O_2-exposures are started. The dotted line is an expanded view to show the sharp initial increase in the current. The inset illustrates a schematic set-up of the measurement.

the work function is too high to allow the electrons to escape. The achievement of Pierce and Meier was to lower the work function of GaAs drastically by the adsorbtion of Cs and O on the surface [92]. The recipe to prepare the GaAs-surface differs for each group working with this material. The one used in this work is described in the following.

For each preparation of the cathode, the GaAs was heated to about 620 K for 1 hour. Then the heating power was increased to about 25 W for 5 minutes, which led to an increase in temperature to approximately 850 K. After this surface cleaning procedure, the sample was cooled down to temperatures below 350 K. As the last step of the preparation, the cathode was activated by sequential exposures to Cs and O_2. During these sequences, the photocurrent was measured. An example for the measured photocurrent recorded during the exposures to Cs and O_2 is shown in Fig. 3.7. First, Cs was evaporated and a first maximum arose in the photocurrent. An additional amount of Cs was added until the current dropped to half of its maximum value. Then, the surface was exposed to an O_2-atmosphere of about 10^{-8} mbar. This led to a strong increase of the photocurrent. The O_2-exposure was stop when the current dropped to $\frac{1}{3}$ of the maximum value. This procedure was repeated four times. For the final Cs-layer the evaporation was stopped soon after the maximum photocurrent was reached. This preparation of the photocathodes yielded photocurrents greater than 100 μA in front of the spectrometer, when illuminating the GaAs with $\approx$ 100 mW light with a wavelength of 830 nm. For the measurements, the spectrometer was typically fed by an emission current of 25 μA, due to space charge

limitations of the monochromators. The reduction of the photocurrent was achieved by reducing the incident laser power. Due to contaminations of the surface of the cathode, the photocurrent dropped with time. To obtain a stable emission of the photocurrent, the drop was compensated by increasing the laser power. Depending on the cathode and the amount of dirt produced in the chamber, for example by motion, cathodes could be used about 25 working hours. After this time, the cathode had to be prepared again.

In the experimental set-up, there was no possibility to measure the degree of the spin polarization of the photocurrent directly. Thus, the polarization was determined by electron scattering experiments using the SPEEL-spectrometer. As discussed in section 2.4.1, the interaction of an electron with a sample depends on the electron spin. As a result, the reflectivity of a sample is not only a function of the primary energy E_{kin} but also of the spin of the incident electron. This is shown in Fig. 3.8 for the intensity of the specularly reflected electron beam elastically scattered from a W(110) crystal. The reflected intensities for the two incident electron spin directions ($I^\uparrow$ and $I^\downarrow$) are shown in Fig. 3.8 a). The difference in the two measured intensity curves is caused by the relatively strong spin-orbit interaction in W. The asymmetry ($A = \frac{I^\downarrow - I^\uparrow}{I^\downarrow + I^\uparrow}$) of the two intensities is presented in Fig. 3.8 b). The maximum measured asymmetry is about 65% at about $E_{kin} = 7$ eV. The polarization of the incident electron beam can be estimated by means of the following two considerations. The asymmetry in the scattering probability of the two spin directions cannot exceed 100%. This results in a lower limit of the polarization of our incident electron beam of $P_{min} = 65\%$. An estimation of the upper limit of the spin polarization is more complicated. Literature values for high spin asymmetries of the reflectivity of W are typically about 80% [104–106]. Using this value, we obtain the high polarization limit of our electron beam of $P_{max} = \frac{65}{0.8} = 81\%$. Because no better values are available, we chose the mean value of the two above mentioned polarizations and considered the difference of the two as the error. For this particular photocathode we obtain $P = 73\pm10\%$ from the measurements.

3.3 Sample preparation and characterization

Two different crystalline structures of Co stabilized on two different substrates are discussed in this work. One is fcc Co grown on Cu(001). This is an interesting system, because this crystalline phase is not stable under ambient conditions in bulk Co-crystals. Bulk Co, however, undergoes a phase transition from the low temperature hcp to the high temperature fcc phase at 690 K [107]. As a second system used as comparison, we thus have chosen the stable room temperature phase, the hcp phase. Thin hcp Co-films were obtained by growing Co on W(110).

3.3.1 The system Co on Cu(001)

Co on Cu(001) belongs to the best studied systems in the field of thin film magnetism. Co grows in a layer-by-layer mode on Cu(001) [108]. In the initial stage of growth, before
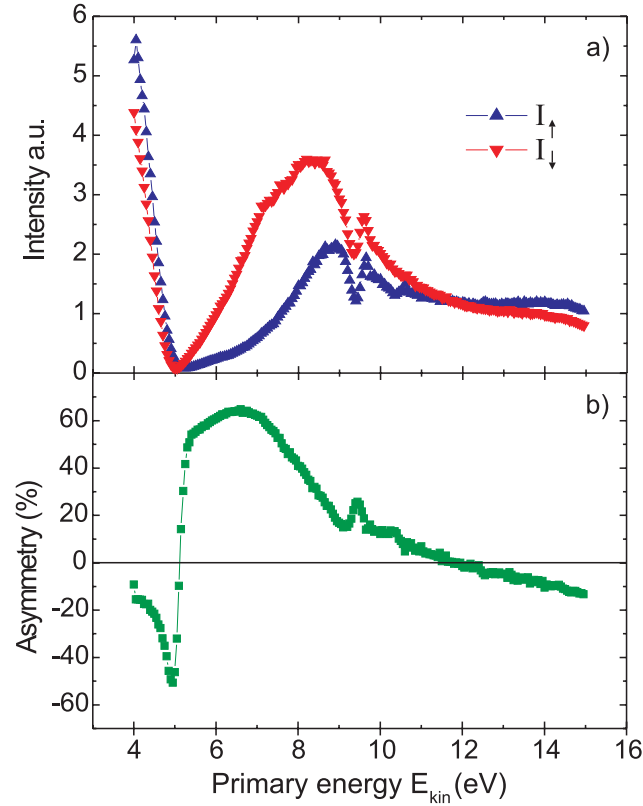
Figure 3.8: a) Measurement of the specularly and elastically scattered electron intensity of the two different spin directions of the incoming electrons as a function of the incoming electron energy. The beam was scattered from a W(110)-crystal. The scattering plane was parallel to the [001]-direction and the angle between incoming and outgoing beam was $\theta_0 = 90°$ (see Fig. 2.7). The asymmetry of the two curves is shown in b). Because of the high intensity of the specularly reflected electron beam, the channeltron was operated in a continuous current mode. Thus, the intensities are given in arbitrary units.

the second layer is completed, deviations from the ideal layer-by-layer growth have been found [109, 110]. In this thickness range also surface alloying was observed [100]. The fcc phase of Co is stabilized by pseudomorphic growth on the fcc Cu-substrate up to thicknesses of 20 monolayers (ML) [109]. The lattice missmatch is about 2% between fcc Co (3.548 Å) and fcc Cu (3.615 Å) [110]. Co adopts the unit cell size of Cu in the plane at least up to 10 ML. Thus, Co is expanded by 2% in the film plane [110,111]. This results in a small compression of the out-of-plane lattice constant of the Co-film of about 2% [110]. Strictly speaking, Co therefore has a face centered tetragonal structure, but this small distortion is neglected in the subsequent discussion. A known problem in this system is the instability of the Co-film against Cu-diffusion to the surface, due to a higher surface free energy of Co [112,113]. This can result in a "sandwich"-structure where one ML Cu sits on top of the Co-film [109]. Even for film thicknesses of 4 ML Co, Cu can diffuse to the top via the formation of pinholes, when the film is heated to about 490 K [114].
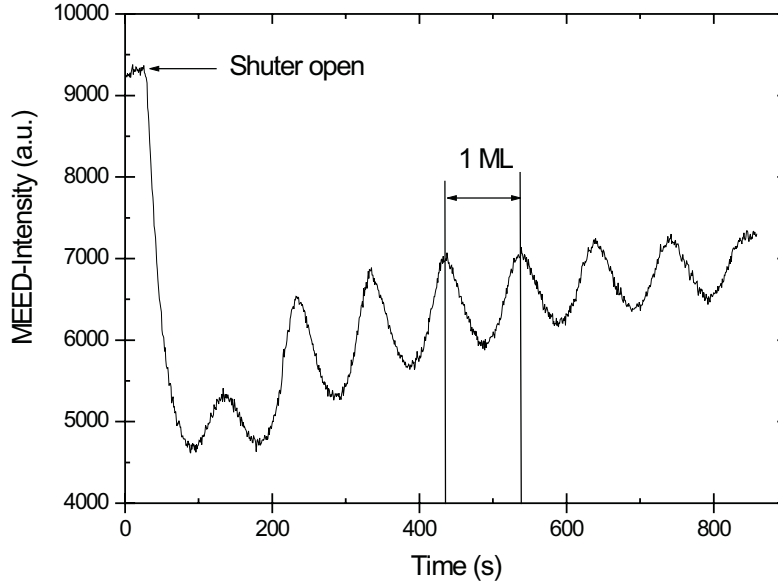
Figure 3.9: Intensity of the specularly reflected MEED-spot as a function of time measured during Co-deposition. The oscillation period is determined by the growth of an additional ML.

The magnetic easy axis in Co lies in the surface plane along $\langle 110 \rangle$. Measurements of the Curie temperature (T_C) as a function of film thickness show that 1 ML Co has already a T_C of about 200 K [115]. T_C increases significantly with increasing film thickness, so that ferromagnetic order at room temperature is achieved for film thicknesses of about 1.5 ML [115]. Due to the already mentioned problem of interdiffusion, the T_C of films thicker than about 2 ML cannot be measured directly. For bulk Co $T_C = 1388$ K [16].

For the experiments in the present study, the sample was prepared using the following procedure. The single crystal Cu-substrate was cleaned by sputtering with 3 kV Ar-ions and a flux of about 3.5 $\frac{\mu A}{cm^2}$ for one hour. Afterwards, the substrate was annealed at 820 K for 10 minutes. The Cu-surface showed a sharp LEED-pattern and no traces of contamination could be seen with AES. Co was deposited by electron beam assisted MBE. The substrate was kept at 300 K during deposition. The thickness calibration was performed by the monolayer period oscillations measured in the MEED-intensity [79]. A typical MEED-measurement taken during the growth of Co on Cu(001) is shown in Fig. 3.9. The thickness calibration was not done on films used for SPEELS-measurements, because we found an increased contamination level on the Co-surface after MEED-measurements. Thus, the main error in the thickness calibration is given by the instability of the Co-source. The uncertainty in subsequent depositions was found to be within 10%. Thicknesses of films quoted in this work are given within this error. The thickness was crosschecked by the absolute Kerr ellipticity signal of the MOKE-measurements. Samples with Co-thicknesses of more than 4 ML have been annealed after deposition to 450 K for 5 minutes. This annealing is known to produce smoother surfaces [116]. The influence of the annealing on
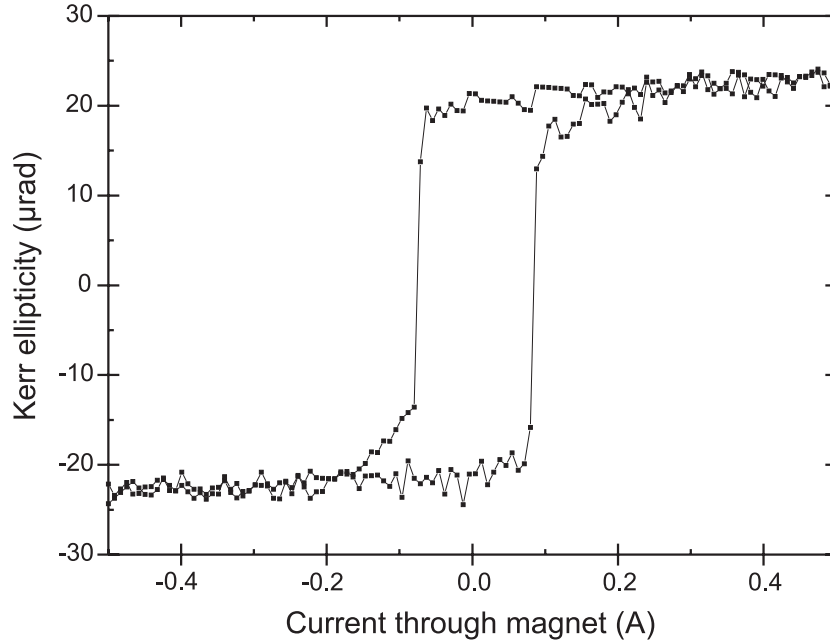
Figure 3.10: Typical longitudinal MOKE measurement of the Kerr ellipticity as a function of the applied magnetic field for 2.5 ML Co on Cu(001). The field was applied along [$\bar{1}$10]-direction.

the SPEEL-spectra will be discussed later.

After the preparation procedure and before the SPEELS-measurements, all samples were exposed to an external magnetic field to magnetize them in a defined direction. Simultaneously, longitudinal MOKE-measurements were performed. A typical MOKE-curve for a 2.5 ML Co-film on Cu(001) taken with the field applied along [$\bar{1}$10]-direction is presented in Fig. 3.10. The measurement shows an easy axis loop as expected from literature [117]. The squareness of the loop shows that the film is almost in the saturated state at remanence. This is important for the SPEELS-measurements, because it results in the maximum possible sensitivity to magnetic scattering. After the sample was magnetized, it was transferred to the SPEELS-champer and the potentials of the spectrometer were optimized. The duration between the deposition of a film and the start of the first SPEELS-measurement was typically 20 minutes when the sample was not annealed and 1 hour when the sample was annealed. After the SPEEL-spectra were taken, MOKE-measurements were performed once again. AES-measurements were only done after SPEELS-measurements to avoid unnecessary contaminations of the surface.

3.3.2   The system Co on W(110)

Co on bcc W(110) is also a well studied system. Co grows in a quasi layer-by-layer mode on W(110) [99, 118]. In the sub-monolayer range, Co grows pseudomorphicaly on the substrate [119, 120]. For thicker films, Co forms a hcp structure with a (0001)-surface.
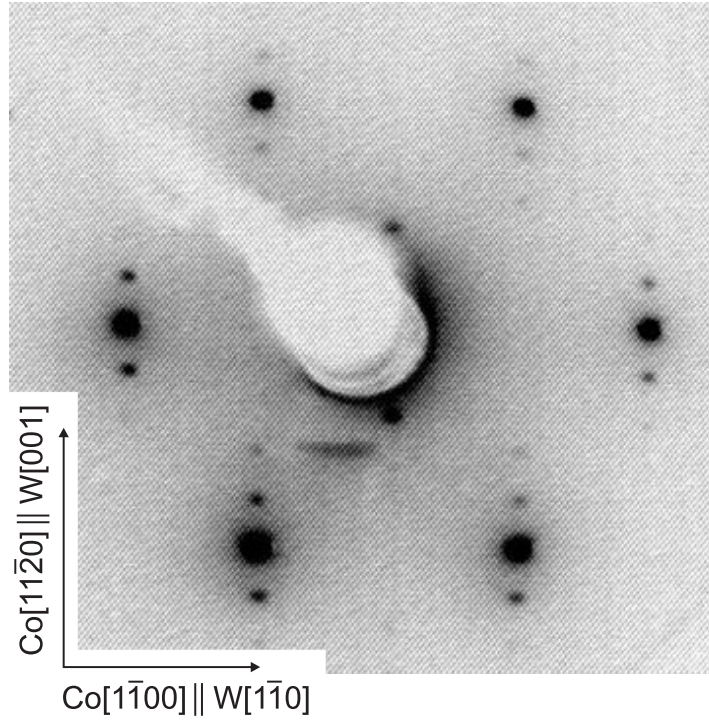
Figure 3.11: LEED pattern of 3.3 ML Co on W(110). The lattice misfit along W[001] causes the formation of a superstructure in this direction. Along W[1$\bar{1}$0] the Co adopts the underlying lattice constant. The picture was taken with a primary electron energy of 143 eV.

The Co[11$\bar{2}$0]-axis lies parallel to W[001] [118, 121]. Assuming the bulk lattice constants of W (3.165 Å) and Co (2.507 Å), one can calculate the lattice misfit to about 21% along Co[11$\bar{2}$0]‖W[001] and 3% along Co[1$\bar{1}$00]‖W[1$\bar{1}$0] [121]. Co adopts the W-lattice constant along the W[1$\bar{1}$0] direction. The giant stress along W[001] direction is avoided by forming a "floating layer" along this direction, where approximately 5 Co lattice spacings correspond to 4 W lattice spacings [118, 121, 122]. This results in a superstructure which is visible in LEED-measurements. A typical LEED-image of this superstructure taken on a 3.3 ML thick Co-film is shown in Fig. 3.11. The superstructure has been followed up to 8 ML Co using a high resolution LEED-apparatus [121]. Assuming the above mentioned ratio of 5 over 4, the Co-lattice is compressed by about 1% along W[001] compared to the bulk lattice constant. In the following, the small distortion from a hcp lattice will be neglected. The hcp stacking sequence has been confirmed up to the twelfth ML Co [118]. Due to the shape anisotropy and the deviation from the hcp structure, the magnetic easy axis lies not along the c-axis but in the surface plane along the [1$\bar{1}$00] Co-axis [121]. This direction of the easy axis remains up to 50 ML thick Co-films [123]. At a coverage of 1 ML, Co is not magnetic [124]. The Curie temperature strongly increases with increasing Co-film thickness [123, 125], as in the case of Co on Cu(001).

The single crystal W(110)-substrate was cleaned by flashing it to high temperatures

by electron bombardment. The initial cleaning of W was done by heating the crystal to about 1700 K (as determined by a pyrometer) for 15 seconds in an O_2-atmosphere of 5×10^{-8} mbar several times. During this procedure, the C which was present at the surface formed CO and desorbed from the surface. Afterwards, the crystal surface was free from any C, but contaminated with O. This O was desorbed by heating the crystal once to higher temperatures > 2200 K for 10 seconds. For new crystals, C diffused from the bulk to the surface at these high temperatures. Therefore, the complete procedure had to be repeated several times to deplete the near surface region from C. Once this depletion is achieved, the cleaning procedure before each sample preparation was rather simple. Metal films as well as contaminations were removed by flashing. If after several heating cycles additional C was present again, it was removed by heating the W-crystal in O_2-atmosphere. The above described procedure is well established and is described for example in Ref. [126].

The film thickness was calibrated by MEED-experiments. The MEED-oscillations are stronger at 100 K [118] than at room temperature. Thus, for the calibration of the Co-source the substrate was cooled down to about 100 K with liquid nitrogen before Co was deposited. For films that were used for SPEELS-measurements, the first ML of Co was deposited at about 600 K, directly after flashing. The additional Co-layers were deposited at temperatures below 400 K. This procedure is known for good growth conditions [118]. In addition, we found that the amount of adsorbates detected by SPEELS was reduced compared to the case where the W-surface was left uncovered during cooling. Before the SPEELS-measurements, the Co was magnetized in a defined direction. MOKE-loops recorded during this procedure confirmed that the sample is uniformly magnetized at remanence. After the SPEELS-measurements, the samples were characterized by MOKE and AES. Cleanliness of the surface was also checked during SPEELS-measurements, since EELS is known to be sensitive to small amounts of adsorbates. Although care was taken to avoid surface contaminations, vibrational losses of small amounts of adsorbates were always detected during SPEELS-measurements on Co on W(110).

Chapter 4

Results

In this chapter, the results of our investigations of spin waves measured by SPEELS are presented. Within the scope of this work, we showed that a clear spin wave signal can be observed in SPEELS experiments. Because of the new method, some measurements were performed which concerned the experiment itself as well as the scattering process of an electron from a spin wave excitation. Most of the experiments, however, were performed to explore the "terra incognita" of spin waves in ultrathin films at high wave vectors. In the first part of this chapter, the results obtained for the spin wave excitations in Co on Cu(001) are shown. The results of the investigations of Co on W(110) are presented in the second part. A detailed discussion of the experimental results is given in chapter 5.

4.1   SPEELS-measurements on Co on Cu(001)

For the SPEELS-measurements performed on fcc Co on Cu(001), the [110]-direction of the Cu-crystal was oriented parallel to the scattering plane. Thus, the measured wave vector transfer was along the $\overline{\Gamma} - \overline{X}$ direction in the surface Brillouin zone (see Fig. 4.1). The magnetization direction of the Co-film was perpendicular to the scattering plane, along [1$\bar{1}$0], if not quoted otherwise. Fig. 4.2 shows a representative example of the spectra measured by SPEELS. In this case, 8 ML Co on Cu(001) were investigated. The intensities of the scattered electrons for the two directions of the spin of the incoming electrons are plotted as a function of the energy loss for a wave vector transfer of $\Delta K_{\parallel} = -0.81$ Å^{-1}. This wave vector corresponds approximately to the position of the green arrow in Fig. 4.1. The open red (blue) symbols mark the measured intensities of the $I_{\downarrow}$-spectrum (incoming electron spin of minority character) and the $I_{\uparrow}$-spectrum (incoming electron spin of majority character), respectively. In the $I_{\downarrow}$-spectrum a prominent loss feature centered at about 170 meV is visible. This peak is caused by the excitation of spin waves by the inelastic scattering of electrons, as will be shown in the following.

The strong peak at zero loss energy is caused by elastic scattering processes. Because of the high intensity of the elastic peak, its foot extents up to about 100 meV. The background is caused by the excitations of electron hole pairs, which can be assumed to be partially Stoner excitations. The intensity scale on the left axis of Fig. 4.2 displays the
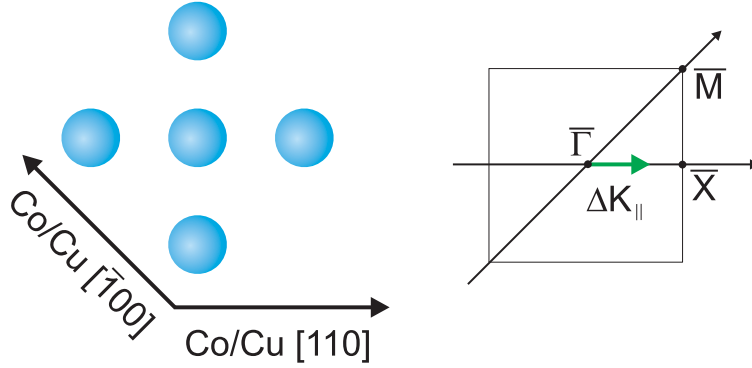
Figure 4.1: Real space and reziprocal space representation of the fcc Co(001) and Cu(001) surface. All SPEEL-spectra were taken with the scattering plane parallel to the [110] direction of the crystal. The wave vector transfer is thus along $\overline{\Gamma} - \overline{X}$ in the surface Brillouin zone. The zone boundary is at $\overline{X} = \frac{\sqrt{2}\pi}{a_0} = 1.23$ Å^{-1}.

count rate in electron counts per second. This scale shows that the spin wave intensity is about $2*10^3$ counts per second under this scattering conditions (for details see figure caption). These high intensities allow relatively short measuring times. The spectra shown in Fig. 4.2 were measured in about 30 minutes. The right intensity scale in this figure shows the normalized intensity. For this scale, the measured intensity at each energy loss was divided by the intensity of the elastically scattered electrons. This axis shows that the spin wave intensity is of the order of a few percent of the elastically scattered intensity.

The strained GaAs-cathode does not produce a completely polarized electron beam. This incomplete polarization of P can be compensated by calculating:

$$I_{\uparrow(\downarrow)} = \frac{P+1}{2P}\, \tilde{I}_{\uparrow(\downarrow)} + \frac{P-1}{2P}\, \tilde{I}_{\downarrow(\uparrow)}. \tag{4.1}$$

Here, I is the intensity corrected for the incomplete polarization and $\tilde{I}$ is the measured intensity. In the measurement shown in Fig. 4.2, the polarization was $P = 0.79 \pm 0.1$. The solid triangles in Fig. 4.2 represent the intensities which are corrected for this incomplete polarization. The error bars illustrate the uncertainty in the correction caused by the uncertainty in P. All spectra shown in the following are corrected for the incomplete polarization of the incoming electron beam.

As can be seen from the polarization corrected intensities shown in Fig. 4.2, the energy loss at 170 meV is only present in the $I_\downarrow$-spectrum within the error bar. This spin selective excitation can be understood on the bases of the considerations given in chapter 2 (see Fig. 2.7). A spin wave is a quantum of *reversed* spin which is spread over the crystal [19]. Since the total magnetic moment is conserved during the scattering process, the incoming electron has to flip its spin from minority to majority character. Therefore, an energy loss caused by the excitation of a spin wave is only possible for an incoming electron of minority spin character. This spin selective excitation process is a first strong indication that the loss feature visible in the $I_\downarrow$-spectrum in Fig. 4.2 can be attributed to spin wave excitations.
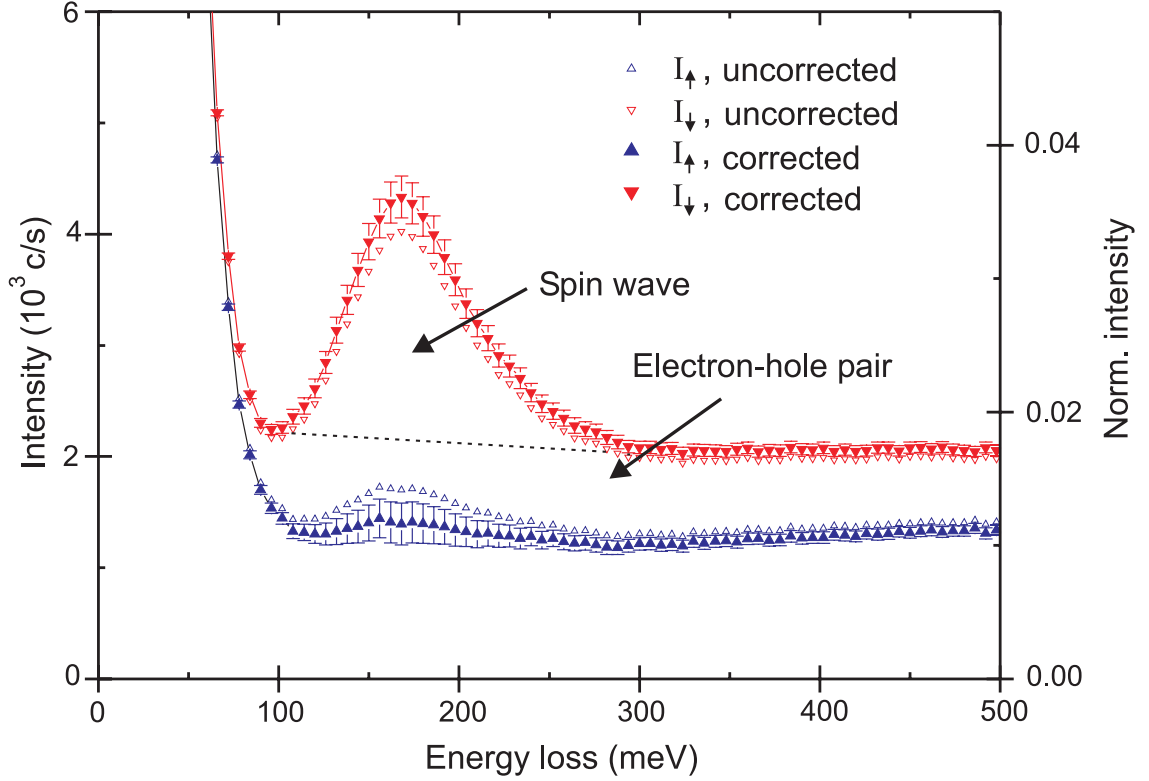
Figure 4.2: SPEEL-spectra measured on 8 ML Co on Cu(001) for $\Delta K_\parallel = -0.81$ Å^{-1}, $E_{kin} = 7$ eV and $\theta_0 = 80°$. The open triangles represent the measured intensities. The solid triangles show the intensities, which were corrected for the incomplete polarization of the incoming electron beam. In this measurements $P = 0.79 \pm 0.1$. The error bars indicate the error caused by the uncertainty in the polarization degree. The energy resolution in this scan was $\Delta E = 39$ meV.

The energy resolution in this scan was $\Delta E = 39$ meV (FWHM) and the peak width of the spin wave signal is about 70 meV (FWHM). As will be discussed later, the finite wave vector resolution has only little effects on the energy width of the loss peak. The measured width is therefore not determined by the spectrometer resolution, but by the intrinsical width of the loss feature. This allowed measurements with relatively low energy resolution. Most of the SPEEL-spectra were measured with an energy resolution of about 40 meV. This way it was possible to fully resolve the spin wave loss features and in addition to perform fast measurements (due to relatively high intensities). In the following, the spectrometer resolution is only mentioned when it is different from about 40 meV.

Beside the spin wave excitations, also the electron hole pair excitations depend on the spin direction of the incident electron. This is visible in the different background for the $I_\downarrow$- and $I_\uparrow$-spectra in Fig. 4.2. Each of the intensities, $I_\downarrow$ and $I_\uparrow$, contains spin flip and non spin flip processes. Because the spin polarization of the scattered electrons was not measured, these different spin channels cannot be separated. Studies with a "complete" experiment
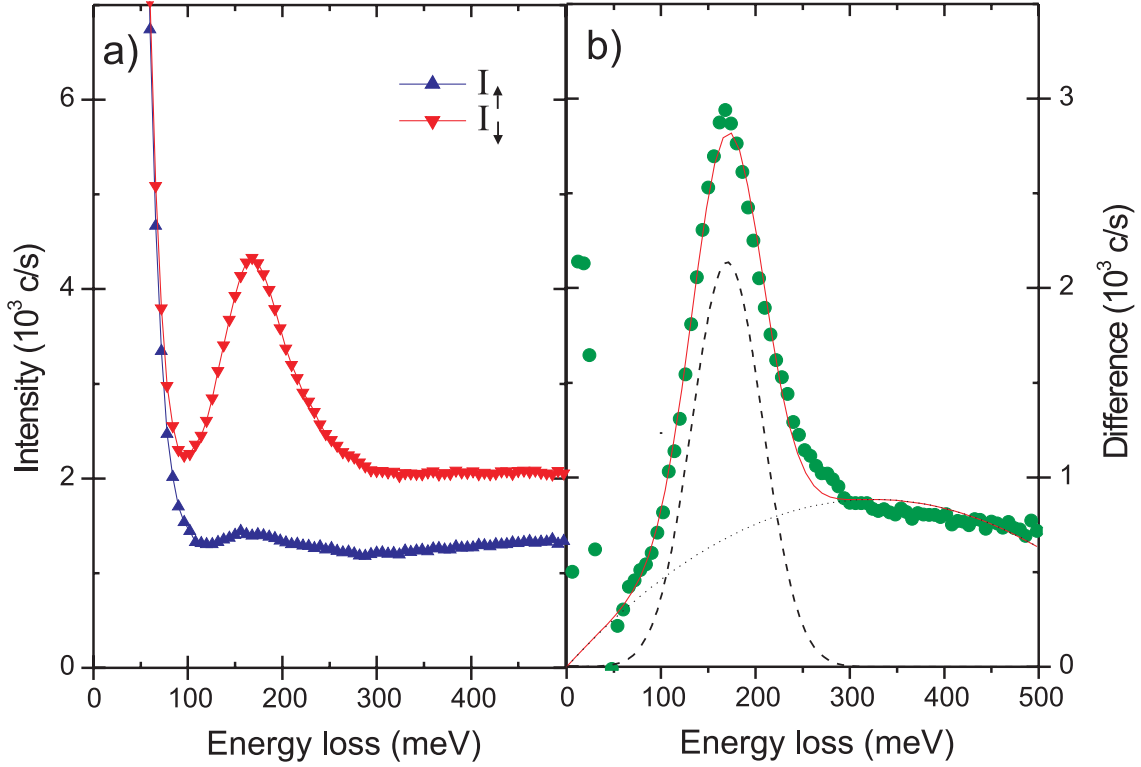
Figure 4.3: In a) the (corrected) intensities of the two spectra shown in Fig. 4.2 are presented, again. In b) the difference $(I_\downarrow - I_\uparrow)$ of the two spectra (green points), and a fit to the difference spectrum are shown (see text for details).

have this possibility [34, 86, 87, 127]. One of these experiments was performed on Co on Cu(001) [34]. It was found that all four spin channels contribute to the intensities at energy losses higher than 300 meV. The energy resolution in this experiments was about 300 meV so that the measurements below this loss energy are difficult to interpret. If one assumes that all spin channels contribute to the background also in the low energy loss range, a significant amount of Stoner excitations should be possible in the energy range of spin waves. The damping of the spin waves due to the decay into these Stoner excitations provides a likely explanation for the measured spin wave width.

Fig. 4.3 a) shows the polarization corrected intensities of the two spectra presented in Fig. 4.2, again. The difference $I_\downarrow - I_\uparrow$ of these two spectra is plotted in Fig. 4.3 b). Because the spin wave signal is the only completely polarized feature in the spectra, it is more prominent in the difference spectrum. The difference of the background of electron hole pair excitations for the $I_\uparrow$- and $I_\downarrow$-spectra produces a background in the difference spectrum, as well. In the difference, the contributions from the elastic peak and from vibrational losses (if present) is drastically reduced. This is due to the fact that these scattering processes do not strongly depend on the spin of the incident electrons. Nevertheless, as can be seen from Fig. 4.3 b), the difference in the elastic peak is not zero. Because this peak has a high intensity, small effects can easily become large on the scale of

the spin wave intensities. Therefore, care has to be taken in interpreting the data around the zero loss condition in the energy loss range of about two times the energy resolution. This sets a low energy limit to the loss energies that can be explored in the experiments.

The difference spectrum can be fitted by considering a spin wave peak and a background. The elastic contribution to the difference is cut by a low energy limit. The spin wave peak is fitted with a Gaussian and the background with a second order polynomial, so that the difference can be written as

$$D(E_{loss}) = A * e^{-(\frac{E_{SW} - E_{loss}}{\sigma})^2} + b * E_{loss} + c * E_{loss}^2. \tag{4.2}$$

Here, the fit parameters are: the spin wave intensity A, the spin wave energy E_{SW}, $\sigma = \frac{W}{2\sqrt{\ln(2)}}$ where W is the FWHM of the spin wave, and b and c parameters for the background. Thus, five parameters have to be determined during the fitting procedure. The resulting fit curve of the spectrum presented in Fig. 4.3 b) is added as a red line in the figure. The two contributions for the spin wave and the background are indicated separately as a black dashed and a dotted line, respectively. At first sight, the fitting curve reproduces the data very well, especially in the region of the spin wave peak. We are therefore able to explain the spectra with a single, broadened spin wave peak of Gaussian shape and a smoothly varying background. This holds also for the other spectra shown later.

When having a closer look, one notices small deviations between the fit and the experimental data. Some extra intensity is observed at the high energy foot of the spin wave peak, which leads to a small overestimation of the spin wave energy and spin wave width. These deviations are systematically observed in many spectra. The deviation is possibly due to physical effects, as will be discussed later. It can, however, be drastically reduced by increasing the amount of fit parameters for the background. Since the true shape of the background is unknown, we use only the two parameters mentioned above and consider the uncertainty as one source of error. To estimate the total error, we used the reproducibility of the values and the uncertainty of the fit parameters. For wave vector transfers within the first Brillouin zone, we estimate the total error in the determination of the spin wave energy to about 10 meV. The spin wave width reacts more sensitive to uncertainties in the background especially in the case of low spin wave intensities. Depending on this intensity, the error in the width is estimated to be between 11 and 15 meV.

We continue by testing the magnetic origin of the loss peak that we attribute to spin wave excitations. An important consequence of the above discussed spin selective excitation of spin waves is that when the magnetization of the sample is reversed the peak of the spin wave loss feature should appear in the "opposite" spin channel. This is simply because the definition of majority and minority spin reverses. The proof of the magnetic origin of the loss feature is shown in Fig. 4.4.[1] Here, two spectra were measured under identical conditions, except that the sample magnetization was reversed. The

---

[1]The spin wave intensities are not the same in Fig. 4.2 and Fig. 4.4. As will be discussed later, this is due to the different scattering conditions (θ_0) used in the two measurements.
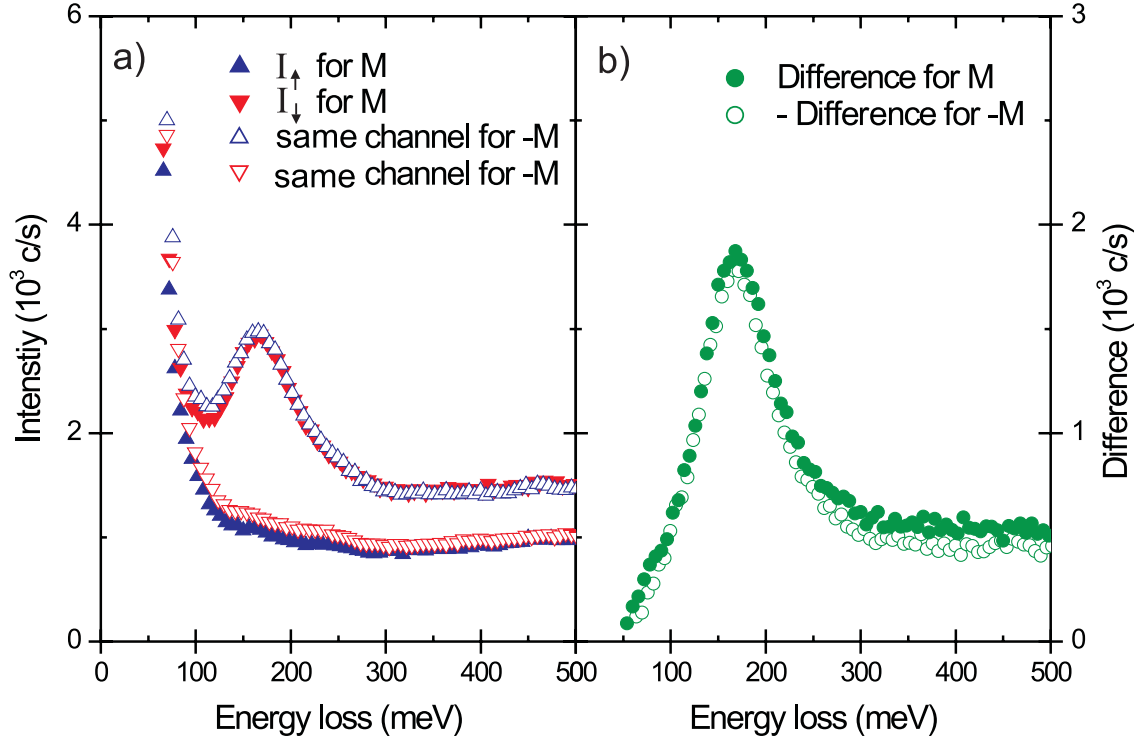
Figure 4.4: a) Comparison between SPEEL-spectra and their differences (b)) measured on oppositely magnetized films. In the measurements marked with M the magnetization lay in the "normal" direction, along $[1\bar{1}0]$. For the measurements labeled as -M, the magnetization was rotated by 180°. Note that for the spectra recorded with -M the negative difference is shown. Both measurements are taken on 8 ML Co, with $\Delta K_{\parallel} = -0.81$ Å^{-1}, $E_{kin} = 7$ eV and $\theta_0 = 90°$.

spectra indicated with M are measured on a Co-film which had the "normal" direction of magnetization. In this case, the normal notation of majority and minority spin character is used. These spectra are presented as solid symbols. The open symbols show the spectra measured on the reversely magnetized Co-film (-M). For these spectra the notation majority and minority is confusing. Therefore, the spectra are assigned as "the same"-channel. This means, the spin direction of the incident electrons was the same for both blue and both red marked spectra. The main result of these measurements is that by reversing the magnetization of the sample, the spectra measured for the two incoming spin directions interchange almost ideally. This holds true in particular for the spin wave feature. Thus, we have proven that the spin-selective excitation is of magnetic origin, as expected for a spin wave excitation. In addition, scattering contributions to these spectra caused by spin-orbit coupling are seen to be quite small because this contributions do not change the sign upon magnetization reversal. Since the spin-orbit contribution is small in Co, it is not considered in the following.

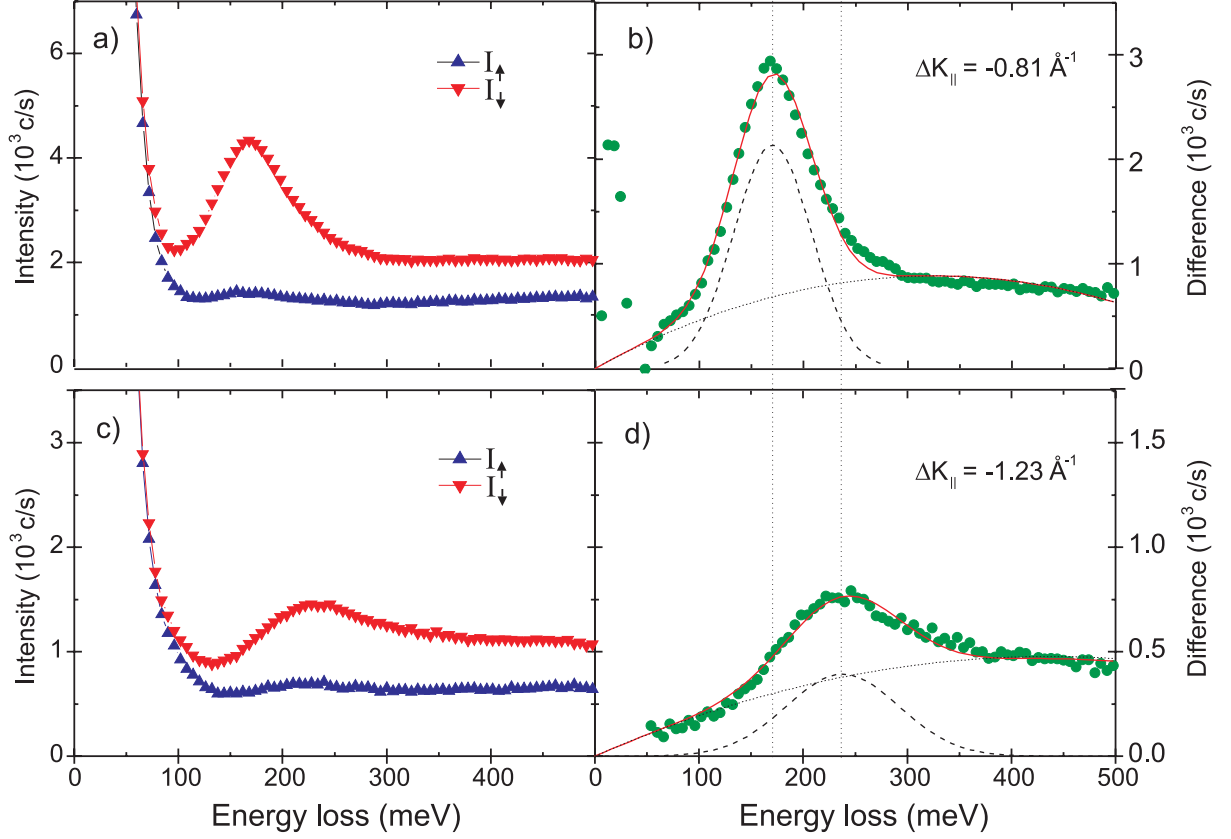Another important characteristics of spin waves is their dispersion. Since the measured

Figure 4.5: In a) and c) SPEEL-spectra are shown for $\Delta K_{\parallel} = -0.81$ Å^{-1} and $\Delta K_{\parallel} = -1.23$ Å^{-1}, respectively. In b) and d) the difference spectrum of each measurement is plotted. The measurements were performed on 8 ML Co on Cu(001). The scattering conditions were $E_{kin} = 7$ eV and $\theta_0 = 80°$. Note that the surface Brillouin zone boundary is at 1.23 Å^{-1} in this system.

loss features are attributed to spin waves, they should move to higher energies for higher wave vector transfers, assuming an acoustic spin wave branch. Two SPEEL-spectra taken at two different wave vector transfers are shown in Fig. 4.5. The spectra were taken at $\Delta K_{\parallel} = -0.81$ Å^{-1} and at $\Delta K_{\parallel} = -1.23$ Å^{-1}, respectively. The latter wave vector transfer corresponds to the surface Brillouin zone boundary in this system ($\overline{X}$-point). From the measured spectra one sees that the spin wave peak shifts to higher energies for higher wave vector transfers, as expected. By fitting the data measured at $\overline{X}$, one obtains a spin wave energy of E = 238±10 meV and a measured FWHM of the spin wave peak of W = 128 ± 13meV. The energy resolution in this scan was $\Delta E = 39$ meV. The dispersion is flat at the surface Brillouin zone boundary, as will be shown later. Therefore, the finite wave vector resolution does not effect the spin wave loss at $\overline{X}$. The measured spin wave width is thus determined by the intrinsic width of the loss feature.

The spin wave intensity is drastically reduced for higher wave vector transfers. Note that the scale in the intensity and in the difference in Fig. 4.5 c) and d) is decreased
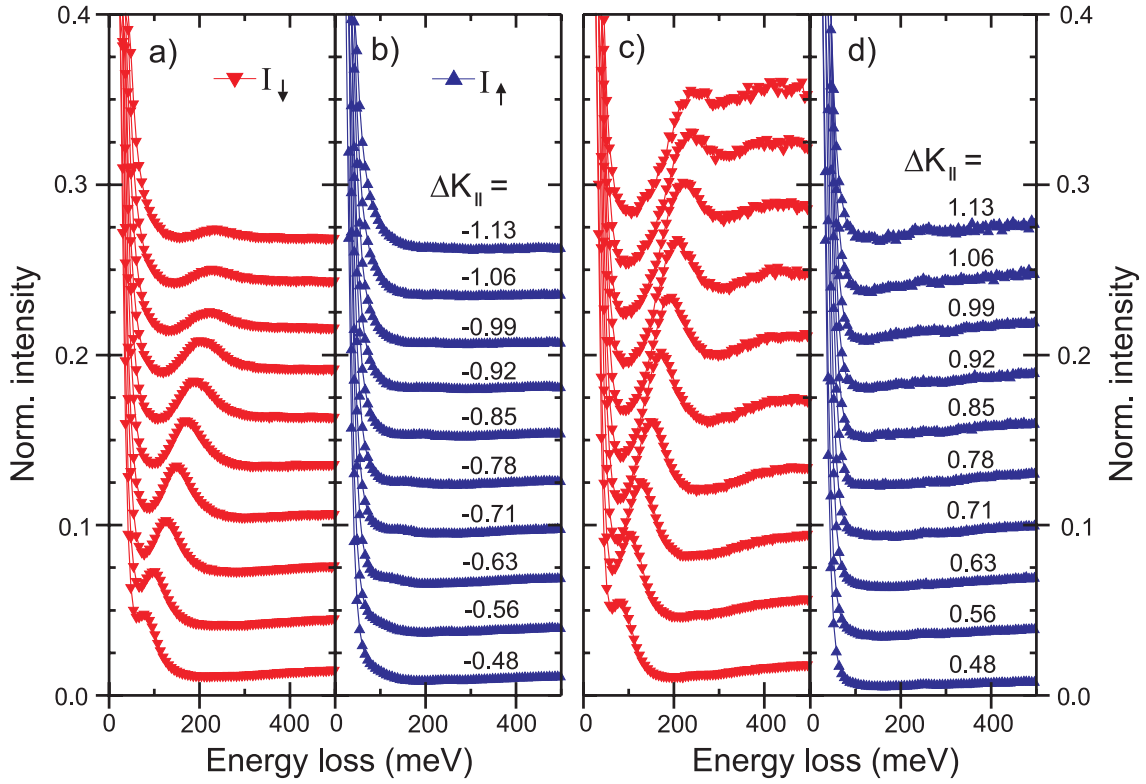
Figure 4.6: Set of SPEEL-spectra taken at different wave vector transfers which are indicated by numbers above the spectra. In a) and b) the spectra for negative and in c) and d) the spectra for positive wave vector transfers are presented. All intensities are normalized with respect to the intensities of their elastic peaks. Each adjacent spectra has an offset of 0.025 (one minor tick) to allow a better comparison. All spectra were measured on 8 ML Co on Cu(001) with $E_{kin} = 6.5$ eV and $\theta_0 = 90°$.

by a factor of two, compared to Fig. 4.5 a) and b). The spin wave intensities measured for these two wave vector transfers are different by about a factor of 5.5. Interestingly, the ratio between the spin wave intensity and the elastic peak intensity remains roughly the same (about one percent). The intensity of the background, however, drops only by about a factor of two over the same wave vector range. Thus, the ratio of the spin wave intensity to the background signal changed.

Fig. 4.5 c) shows that in the SPEELS-experiments the spin wave peak can be followed up to the surface Brillouin zone boundary. The Co-thickness was 8 ML in this case. This illustrates the capability of SPEELS to investigate high wave vector spin waves in ultrathin films.

An overview of several SPEEL-spectra which were taken at different wave vector transfers is presented in Fig. 4.6. All spectra were taken on an 8 ML Co-film on Cu(001). Fig. 4.6 a) and b) show the measured intensities for negative and c) and d) for positive wave vector transfers. For low absolute values of the wave vector transfer, the spin wave

losses appear as a shoulder in the elastic peak. For higher wave vector transfers, the spin wave loss feature shifts to higher loss energies which is a result of the dispersion. A comparison of the spectra in Fig. 4.6 a) and c) and b) and d) shows that the normalized intensities at positive and negative wave vector transfers are different in the $I_\downarrow$-spectra, but similar in the $I_\uparrow$-spectra. In the $I_\downarrow$-spectra both, the relative spin wave intensities and relative background intensities, are higher for positive wave vectors. Also the shape of the background is different in Fig. 4.6 a) and c). The absolute intensities are higher by roughly a factor of two for the negative wave vector side (visible by the better statistics in Fig. 4.6 a) and b)). We attribute the differences in the spectra taken at positive and negative wave vector transfers to the differences in the scattering geometries. More grazing incidence was used for negative and more normal incidence for positive wave vector transfers. In the different scattering geometries, the various scattering processes could change their relative excitation probability. An interesting feature is the pronounced minimum of the background between the elastic peak and the spin wave excitations in the $I_\downarrow$-spectra for high wave vectors on the positive wave vector side. To attribute this drop in the background to a particular feature in the band structure is reliably possible only in a complete experiment. Measurements on Co on Cu(001) with such a complete experiment have been performed by Kämper et al. [34]. The energy resolution used in this experiment, however, was to poor to resolve the structure shown in Fig. 4.6.

From the SPEEL-spectra shown in Fig. 4.6, one can determine the energy position of the spin waves as a function of the wave vector transfer. The resulting dispersion curve is presented in Fig. 4.7. In principle, the complete physical information is contained in half of the surface Brillouin zone, i.e. between $\overline{\Gamma}$ and $\overline{X}$. To confirm the reliability of our measurements, however, we measured the spin wave energies for both sides of the surface Brillouin zone. As expected, the dispersion for negative and positive wave vector transfers is the same, within the error bars. A closer look shows that the spin wave energies systematically lie at slightly higher values for positive wave vector transfers compared to the values at negative wave vector transfers. We attribute this behavior to errors caused by the fitting procedure, mainly due to the different shape of the background. Nevertheless, within the given errors the data are consistent. To confirm that the measured spin wave dispersion obeys the periodicity of the surface Brillouin zone, we also performed measurements beyond $\overline{X}$ for negative wave vector transfers.

In section 2.2.1, the spin wave dispersion within a nearest neighbor Heisenberg model was calculated for a semi-infinite fcc crystal along the $\overline{\Gamma} - \overline{X}$-direction. The resulting dispersion relation of the surface spin wave mode was given by equation 2.16. We have fitted this dispersion relation to the measured data (black line in Fig. 4.7). A surprisingly good agreement is found between the experimental data and the derived dispersion of the surface spin wave mode. Note that the shape of the calculated dispersion is defined by the crystalline structure and geometry of the system. The only fit parameter used in this model is the product of the exchange coupling constant and the magnetic moment (JS). It defines the amplitude of the dispersion, in other words, the spin wave energy at the surface Brillouin zone boundary. The value of JS resulting from the fit shown
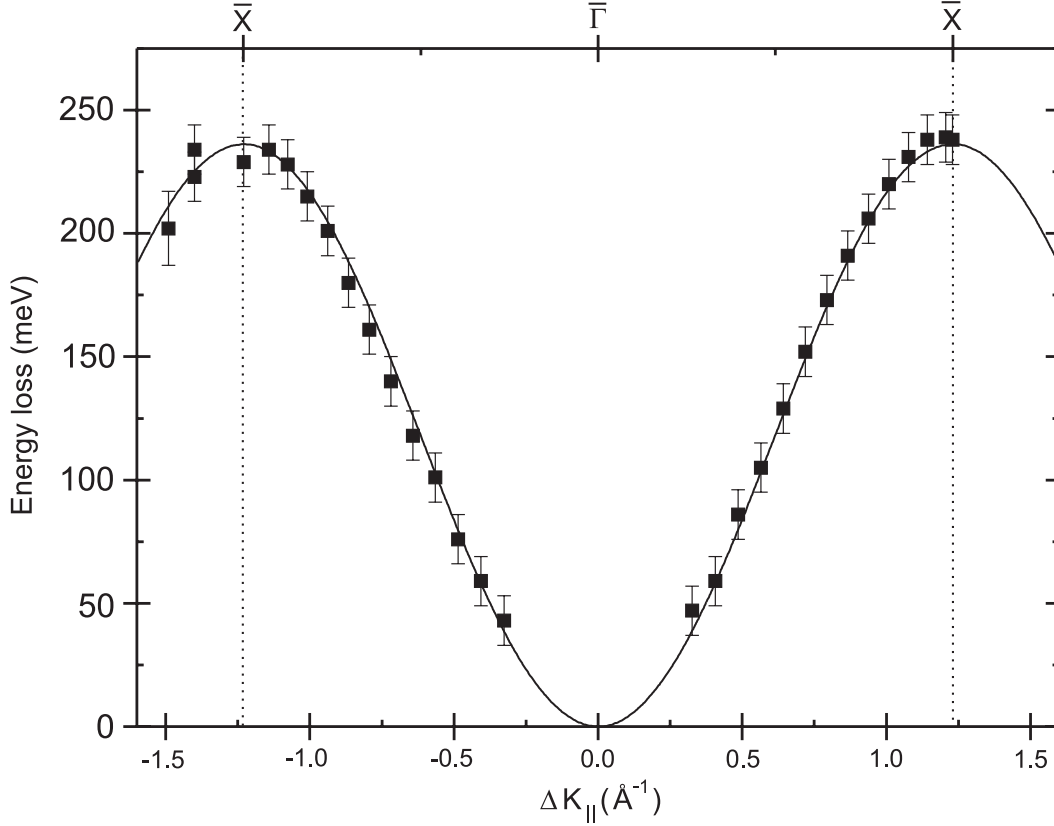
Figure 4.7: Spin wave dispersion of 8 ML Co on Cu(001) measured by SPEELS. The data points represent the energy position of the maxima of the spin wave peaks, as determined by fitting. The solid line is a fit to the data with the surface mode of a nearest neighbor Heisenberg model (details in the text). Measurements with wave vectors below $\overline{X}$ (spectra shown in Fig. 4.6) were taken with $E_{kin} = 6.5$ eV and $\theta_0 = 90°$, at $\overline{X}$ and at $\Delta K_\parallel = -1.40$ Å^{-1} with $E_{kin} = 7$ eV and $\theta_0 = 80°$, and at $\Delta K_\parallel = -1.49$ Å^{-1} with $E_{kin} = 8$ eV and $\theta_0 = 80°$.

in Fig. 4.7 is JS $= 15 \pm 1$ meV.[2]This value is in perfect agreement with the value of JS $= 14.7 \pm 1.5$ meV which was obtained by neutron scattering experiments for bulk spin waves in fcc Co (with 8% Fe to stabilize the fcc phase at room temperature) [128,129]. We consider this agreement as a strong evidence that the loss features in the SPEEL-spectra are caused by the excitation of surface spin waves.

In addition to the spin wave energy, the analysis of the measured spectra yields values for the spin wave intensity and the spin wave width. The spin wave intensity and width

---

[2]From the dispersion relation, one can estimate the additional broadening of the energy loss spectra caused by the finite wave vector resolution. As has been mentioned already, the dispersion is flat close to the surface Brillouin zone boundary. At this point, the finite wave vector resolution has almost no effect. For the spectra shown in Fig. 4.3 measured at $\Delta K_\parallel = -0.81$Å^{-1}, the wave vector resolution yields an additional contribution to the energy resolution of about 12 meV. This has only little influence on the measured spin wave width.
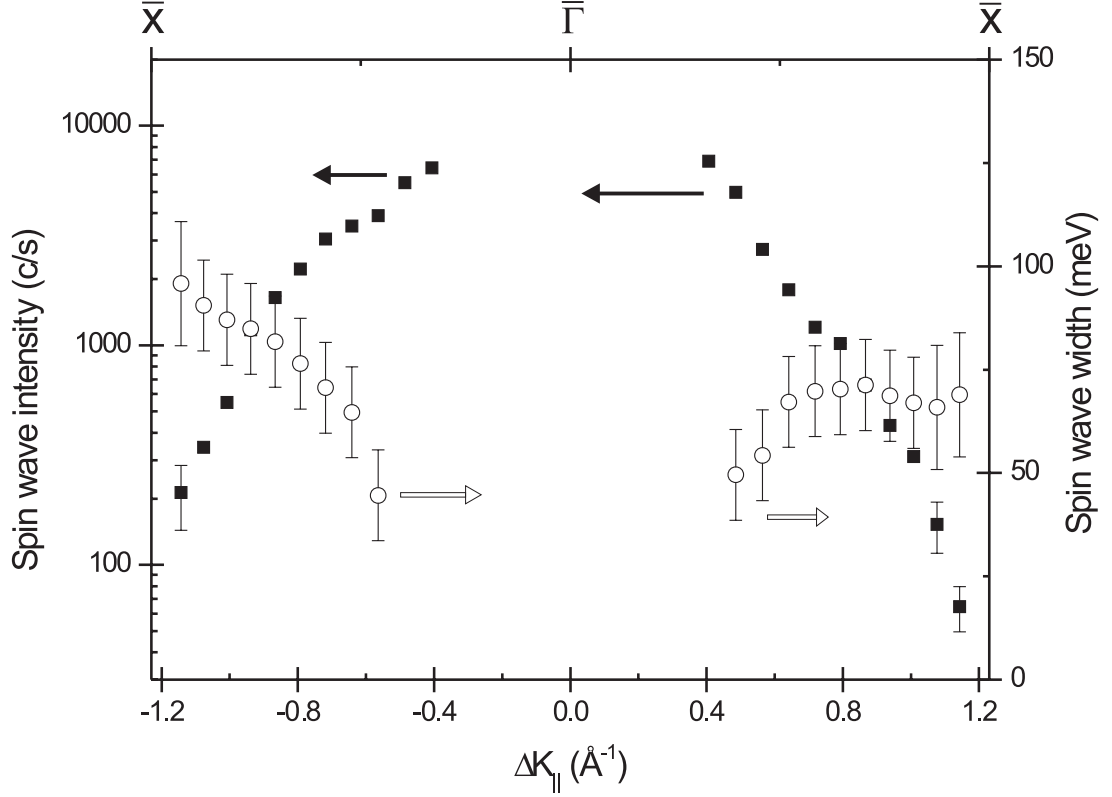
Figure 4.8: Intensity (■/left scale) and width (○/right scale) of the spin wave peak for different wave vector transfers. Note that the spin wave intensity is shown in a logarithmic scale. The spin wave width (FWHM) is corrected for the instrumental energy resolution. All measurements were taken with E_{kin} = 6.5 eV and θ_0 = 90°. The error bars in the intensity are shown when they are significantly larger than the size of the data points.

obtained from the spectra shown in Fig. 4.6 is presented in Fig. 4.8. The main result is that the spin wave intensity drops fast with increasing wave vector transfer. This is likely due mainly to a drop of the cross section for spin wave excitation for increasing wave vector transfers. This interpretation is supported by the observation that the spin wave intensity drops continuously beyond the first surface Brillouin zone boundary. The data points beyond the surface Brillouin zone boundary are not shown in Fig. 4.8. Their absolute values are difficult to compare to the values shown in Fig. 4.8 because of the different scattering conditions used. The spin wave width, shown in Fig. 4.8, increases for higher wave vector transfers. Unexpected differences occur for positive and negative wave vector transfers. These differences are most probably due to the errors caused by the fitting. For some spectra taken at the lowest wave vector transfers, the measured spin wave widths were determined by the spectrometer resolution. These data points have not been included in Fig. 4.8.

The process of the excitation of a spin wave in electron scattering is not fully understood. In particular, the dependence of the cross section of this excitation on the wave
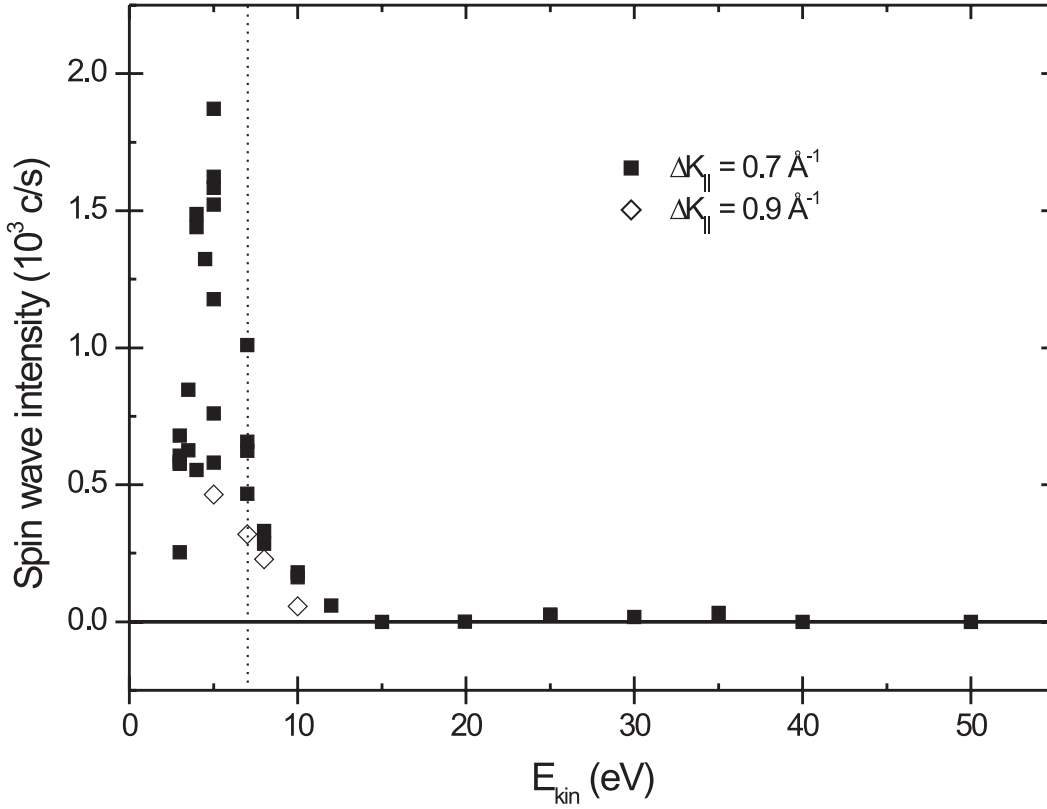
Figure 4.9: The spin wave intensity in the SPEEL-spectra strongly depends on the kinetic energy of the incoming electrons E_{kin}. The solid points are for measurements with $\Delta K_\parallel = 0.7$ Å^{-1} and the open symbols for $\Delta K_\parallel = 0.9$ Å^{-1}. In all measurements shown here $\theta_0 = 90°$. The dotted line marks $E_{kin} = 7$ eV where most measurements have been performed.

vector and energy transfer is unknown. From the measured spectra alone it is difficult to distinguish a drop of the cross section from a drop of the spin wave intensity in the material itself. As has been mentioned already, it is, however, likely that the cross section for spin wave excitations drops with increasing wave vector transfers. We found in our experiments that the excitation probability depends not only on the wave vector transfer but also on the incident electron energy and on the scattering conditions. This makes it rather difficult to compare spectra measured under different conditions.

The spin wave intensities measured at two fixed wave vector transfers ($\Delta K_\parallel = 0.7$ Å^{-1} and $\Delta K_\parallel = 0.9$ Å^{-1}) as a function of the primary energy of the incoming electrons are shown in Fig. 4.9. The key feature in this graph is the strong enhancement of the spin wave intensities below $E_{kin} = 10$ eV. At these low primary energies the intensity of the spin wave signal is enhanced by more than an order of magnitude. This allowed the clear detection of the spin wave loss features. Finding this enhancement has to be considered as the break through of this work. Though, this enhancement is crucial for the experimental results, its origin is not completely understood. As will be discussed in chapter 5, it is
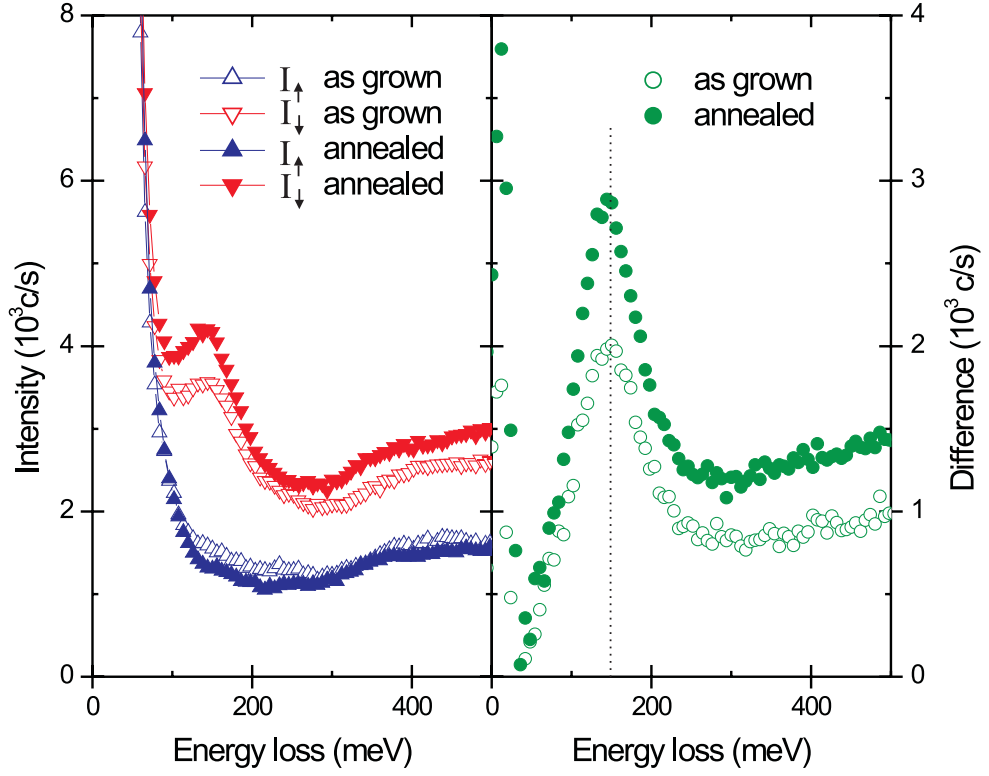
Figure 4.10: Changes of the SPEEL-spectra caused by the annealing of an 8 ML Co-film. The spectra indicated as "as grown" were taken directly after Co-deposition. Those spectra labeled by "annealed" were measured after heating the same film to 450 K for 5 minutes. Both measurements were performed for $\Delta K_{\parallel} = 0.7$ Å^{-1}, with $E_{kin} = 7$ eV, and $\theta_0 = 90°$.

presumably caused by the energy dependence of the exchange scattering process. The data have a relatively large scattering which we mainly attribute to the differences in the optimizations of the potentials applied to the spectrometer. The absolute intensity scale depends on the scattering geometry, for example on the scattering angle θ_0. The enhancement of the spin wave intensities at low primary energies of the incoming electrons, however, is similar in all cases studied. The phenomenon shown in Fig. 4.9 is also not limited to the system of fcc Co on Cu(001). We obtained similar results for fcc Fe on Cu(001) [15] and hcp Co on W(110), as well. The latter results are shown in section 4.2.

Another aspect that was mentioned before is the influence of annealing of the Co-films before the SPEELS-measurements. As described in chapter 3.3, films of Co-thicknesses above 4 ML were annealed to 450 K for 5 minutes. In Fig. 4.10, a comparison is made between the SPEEL-spectra measured on an as-grown film and on the same film after annealing. The main effect of the annealing process is the increase of the intensity of the "magnetic signal" at the energy loss positions of the spin waves and Stoner excitations. After annealing, the difference signal at these loss energies increased by about 50%. No influence of the annealing process on the energy position of the spin wave signal could be
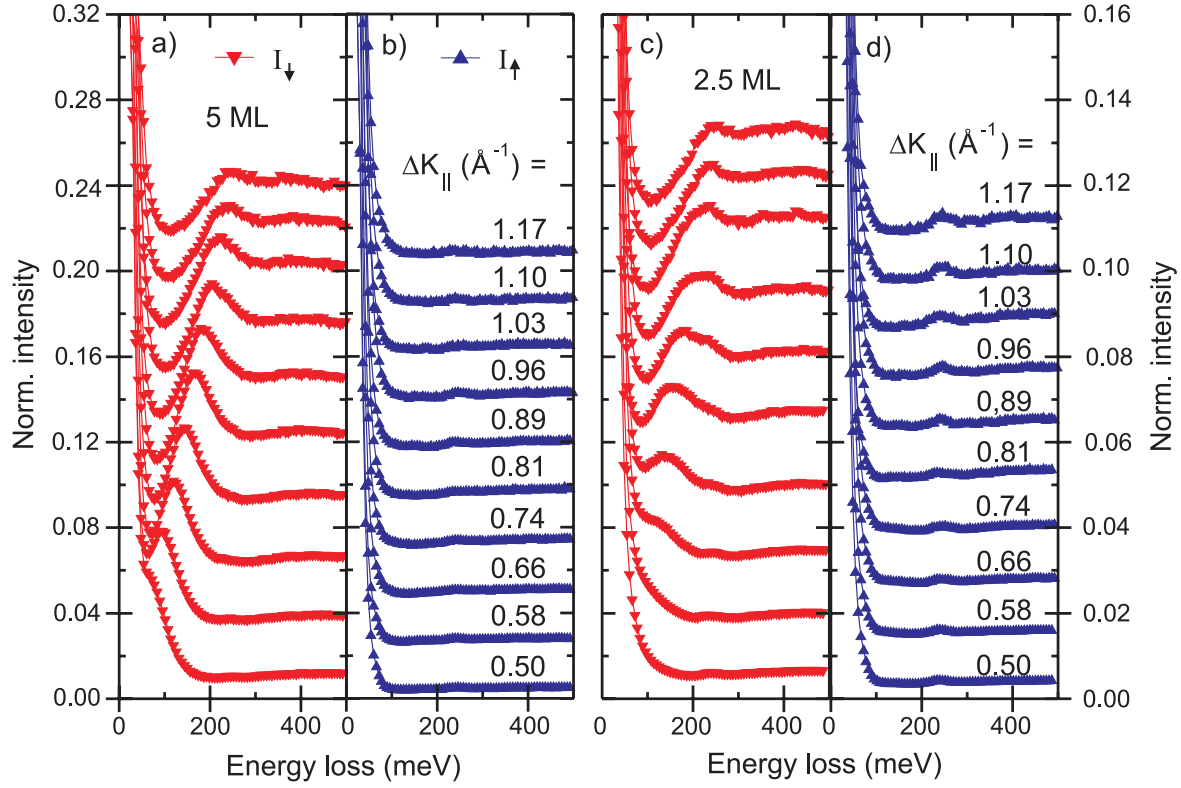
Figure 4.11: Set of SPEEL-spectra measured on 5 ML (a) and b)) and 2.5 ML (c) and d)) Co-films on Cu(001). The different wave vector transfers are indicated by the numbers above the spectra. The intensities are normalized to the intensity of the elastic peak. Each adjacent spectra has a vertical offset of $\frac{1}{16}$ of the total scale (one minor tick) to allow better comparison. All spectra were taken with $E_{kin} = 7$ eV and $\theta_0 = 90°$.

found. This is indicated by the vertical line in Fig. 4.10. Also, only small changes were found in the MOKE-hysteresis taken on these two Co-films. In particular, the remanence and the saturation values were similar in both cases.

An increase of the annealing temperature to values higher than 450 K resulted in a drastic reduction of the difference signal. This is probably caused by the diffusion of Cu to the surface. Annealing of Co-films with a thickness below 4 ML resulted in a decrease of the difference signal already for annealing temperatures below 400 K. These films were therefore not annealed before the SPEELS-measurements.

So far, the presented results were measured on 8 ML Co on Cu(001). Because of the short mean free path of low energy electrons, this can be considered as a relatively thick film. We performed SPEELS-measurements on thinner Co-films to investigate the influence of reduced dimensions and to test the capabilities of this method. As an example, SPEEL-spectra measured on 5 ML and on 2.5 ML Co-films on Cu(001) are shown in Fig. 4.11 a),b) and c),d), respectively. Even for 2.5 ML Co, the spin wave loss features are clearly visible in the spectra, though the spin wave intensities are reduced (note that

the normalized intensity scales for the two film thicknesses differ by a factor of two). This effect is partially caused by the reduced thickness but also the normalization to the elastic peak and the different film preparations are of importance. As already mentioned, the 2.5 ML thick Co-films were measured as grown, while the 5 ML thick films were annealed, which resulted in an increased spin wave signal. Though the spin wave intensity is smaller for the film of 2.5 ML thickness, the spin wave loss features are still quite prominent, especially for wave vectors around the middle of the surface Brillouin zone. From the measured signal to noise ratio one could speculate that it should be possible to investigate spin wave excitations by SPEELS in one monolayer thick magnetic films. As discussed in section 3.3, a well-defined monolayer of Co on Cu(001) does not exist, which prevented the experimental proof on this system.

Beside the spin wave signal, other loss features are present in the spectra, especially in the spectra of 2.5 ML Co. These losses were excited for both spin directions of the incoming electrons and do not show a dispersion. They can be attributed to vibrational losses caused by traces of adsorbates on the surface. For the spectra shown in Fig. 4.11, mainly a loss feature at about 230 meV is visible. This can be assigned to CO [83], which was confirmed by additional adsorbtion studies.

In both series of spectra presented in Fig. 4.11, a clear dispersion of the spin wave peak is visible. From the spectra, the spin wave dispersion can be extracted as in the case of the 8 ML Co-films. The resulting spin wave dispersions are shown in Fig. 4.12. For completeness, also the dispersion measured on the 8 ML Co-film is included. At first glance, the dispersions of the three different film thicknesses are similar. A closer look shows that there are small but noticeable differences between the dispersions of the different films. Although there is some scattering in the data, a clear tendency is visible that the spin wave energies are reduced for thinner films for wave vectors not to close to the surface Brillouin zone boundary. Close to the surface Brillouin zone boundary, the spin wave energies are independent on the thickness within the error bars. As a comparison, the dispersions of the surface mode of a semi-infinite crystal and of a 2 ML slab are added in Fig. 4.12 as a solid and a dashed line, respectively. The two dispersions were derived within the nearest neighbor Heisenberg model. For both calculated dispersions, we used JS = 15 meV. For intermediate wave vectors, the calculated spin wave energies for the 2 ML slab lie below the one for the semi-infinite crystal. At the surface Brillouin zone boundary, however, both curves meet. This behavior describes the experimental findings very well. Although JS is the same, the calculated dispersions are different because of the surface localization of a surface spin wave mode. This localization increases with increasing wave vector of the spin waves (see equation 2.15). In the nearest neighbor Heisenberg model, the spin wave is completely localized in the surface layer at the surface Brillouin zone boundary. Since the interactions in the model are limited to the nearest neighbors, it does not make any difference at $\overline{X}$ wether the film is only 2 ML thick or semi-infinite. For lower wave vectors, the spin wave is less localized at the surface and therefore the absence of magnetic atoms below the second layer in the slab configuration reduces the spin wave energy.

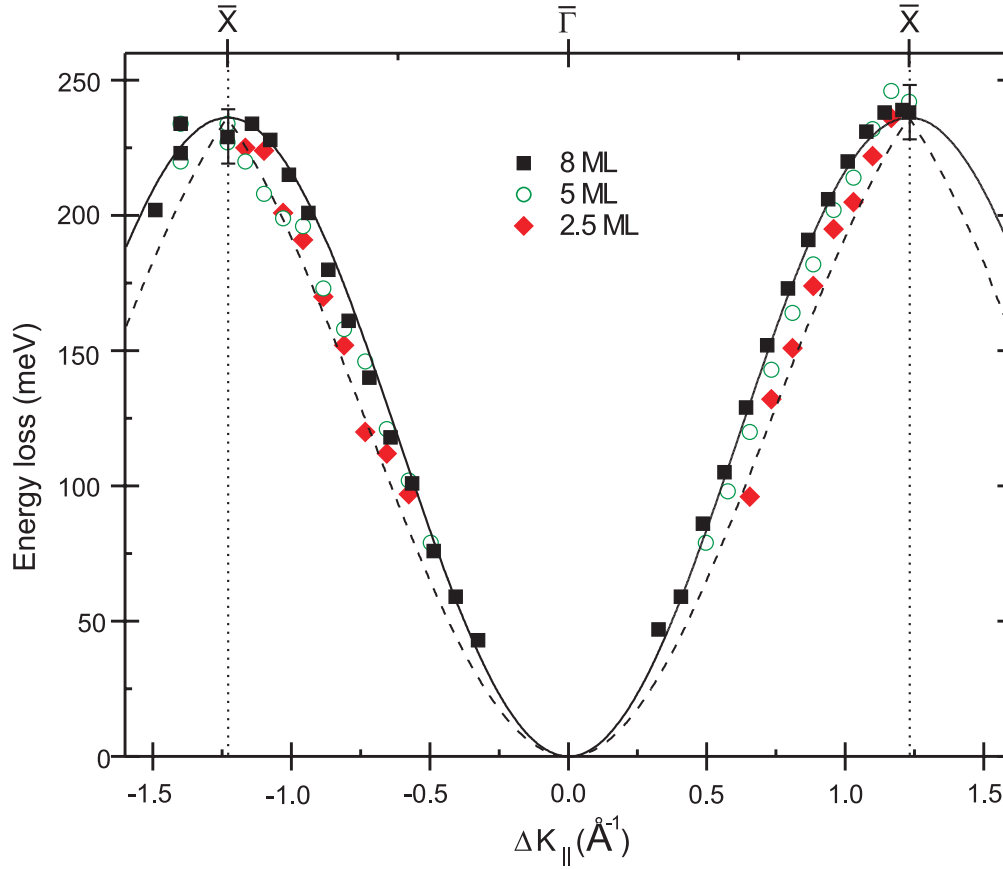The Curie temperature is drastically different for 8 and 2.5 ML thick Co-films. For

Figure 4.12: Spin wave dispersion for 8, 5, and 2.5 ML Co on Cu(001). The error bar is ± 10 meV for each point within the first surface Brillouin zone (indicated for $|\Delta K_{\parallel}| = 1.23$ Å^{-1}). The solid and the dashed lines are dispersions of the surface spin wave mode calculated within a nearest neighbor Heisenberg model with JS = 15 meV for a semi-infinite film and a 2 ML slab, respectively.

the 2.5 ML thick Co-films, T_C can be estimated to be about 650 K [115]. T_C of an 8 ML Co-film is close to the bulk value (1388 K) [16]. All measurements were performed at room temperature. Thus, the effective temperature changed from about $\frac{1}{4}$ T_C for 8 ML to about $\frac{1}{2}$ T_C for 2.5 ML thick Co-films. To exclude influences of the temperature on the spin wave energies, we performed additional low temperature measurements at 110 K. The measurements were done on a 2.5 ML thick Co-film, for which the strongest changes as a function of temperature are expected. In these experiments, the effective temperature was changed from about $\frac{1}{2}$ T_C at room temperature to less than $\frac{1}{5}$ T_C at 110 K. Thus, the change in the effective temperature between these two measurements is larger than the changes in the effective temperature caused by the changes of the Co-layer thicknesses. The results of the experiments are shown in Fig. 4.13 a) and b) for the room temperature and the low temperature measurements, respectively. At 110 K, the sticking coefficients of adsorbates are drastically enhanced. Because the measuring time was the same in both
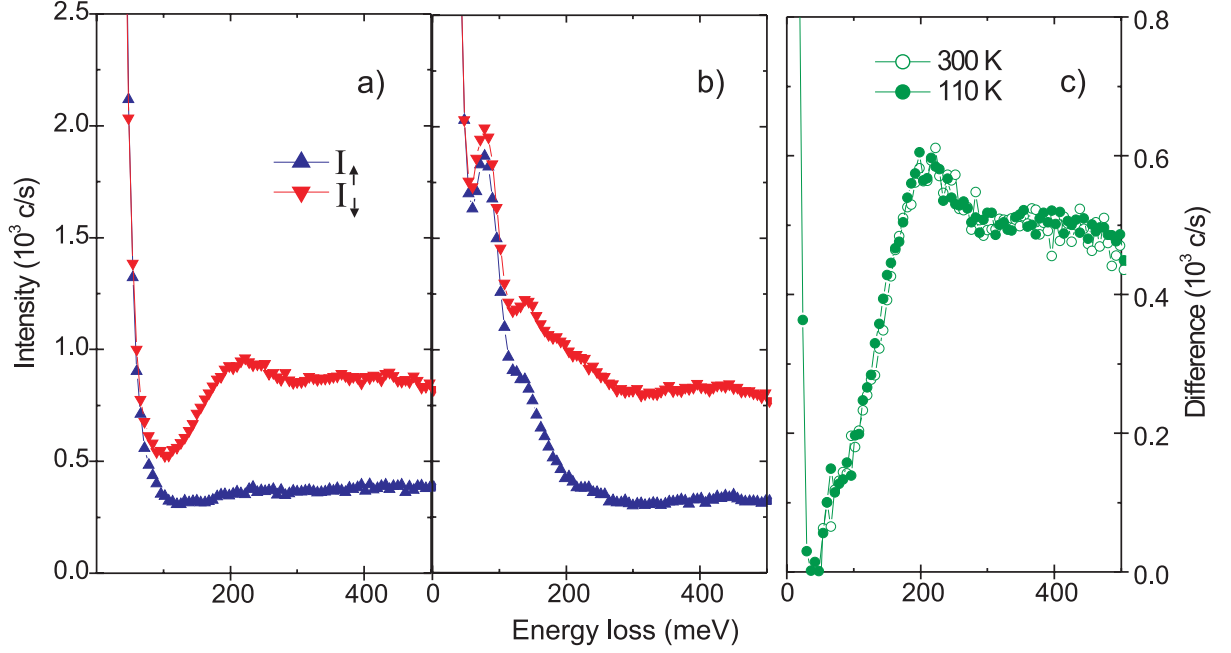
Figure 4.13: SPEEL-spectra for 2.5 ML Co on Cu(001) measured at room temperature (a)) and at 110 K (b)). In c) the difference spectra for both measurements are shown. The spectra were measured with $\Delta K_{\parallel} = 1.03$ Å^{-1}, $E_{kin} = 7$ eV, and $\theta_0 = 90°$.

cases, the low temperature spectra are dominated by vibrational losses caused by the adsorbates O and H. The spin wave loss is hardly visible in the spectra in Fig. 4.13 b).[3] In the difference spectra shown in Fig. 4.13 c), the losses caused by the adsorbates (nearly) cancel out. Despite the additional adsorption peaks visible in the intensity spectra, the difference spectra for the two different temperatures are almost identical. Therefore, an influence of the temperature on the spin wave energies can be excluded in the temperature range under investigation.

---

[3]The influence of adsorbates on the spin wave excitation will be shortly discussed in the next section. For the moment, it is sufficient to mention that H does not change the spin wave spectra significantly and that O changes mainly the spin wave intensity in the spectra.
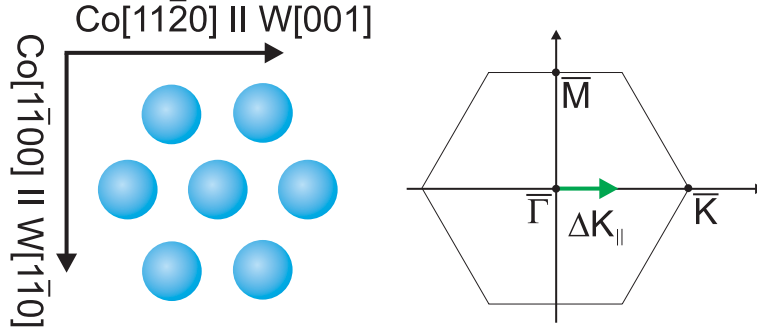
Figure 4.14: Real space and reciprocal space representation of the Co(0001)-surface. All SPEEL-spectra were taken with the scattering plane parallel to the Co[11$\bar{2}$0]-axis, which is parallel to W[001]. The wave vector transfer is along $\overline{\Gamma} - \overline{K}$ in the surface Brillouin zone. The zone boundary is at $\overline{K} = 1.64$ Å^{-1}.

4.2   SPEELS-measurements on Co on W(110)

We now turn to the results obtained on hcp Co on W(110). For this system, the scattering plane was chosen along the Co[11$\bar{2}$0]-axis, which is parallel to the W[001]-axis (see Fig. 4.14). This corresponds to the $\overline{\Gamma} - \overline{K}$-direction in the reciprocal space.

In Fig. 4.15, SPEEL-spectra are compared which were taken on 8 ML hcp Co on W(110) (a) and b)) and 8 ML fcc Co on Cu(001) (c) and d)) for the same wave vector transfer of $\Delta K_{\parallel} = 0.78$ Å^{-1}. In the spectra of hcp Co, a well-defined spin wave loss feature is visible, as well. The spin wave energy and shape are similar for both spin wave loss features. The background of electron hole pair excitations is different for the two crystalline structures. An other aspect is the different amount of vibrational losses present in the spectra. More and stronger vibrational losses are visible in the spectra measured on Co on W(110). The vacuum conditions were nearly identical in both studies. We conclude that either the sticking coefficients are higher on hcp Co on W(110) or that the sample preparation of Co on W(110) could not be done as clean as in the case of Co on Cu(001). In the spectra shown in Fig. 4.15 a), the vibrational loss features can be attributed to a H-metal vibration (140 meV) and probably to an H$_2$O-vibration (450 meV). The energy values are in agreement with literature values [83]. The H-vibration was crosschecked by adsorption studies. From these adsorption studies, it is also possible to estimate the amount of adsorbates. The H-loss peak in Fig. 4.15 a) corresponds to a coverage of about 10% of the saturation coverage. The effect of contaminations of the surface on the spin wave signal is discussed later. At the moment, it is sufficient to note that this level of contaminations has little effects on the spin waves.

To measure the spin wave dispersion for hcp Co on W(110), several spectra were recorded for different wave vector transfers. One series of measurements is shown in Fig. 4.16. In general, a similar behavior of the spin wave loss feature compared to the case of Co on Cu(001) was measured. The spin wave loss feature shifts to higher energies for increasing wave vector transfers due to a strong dispersion. From the normalized
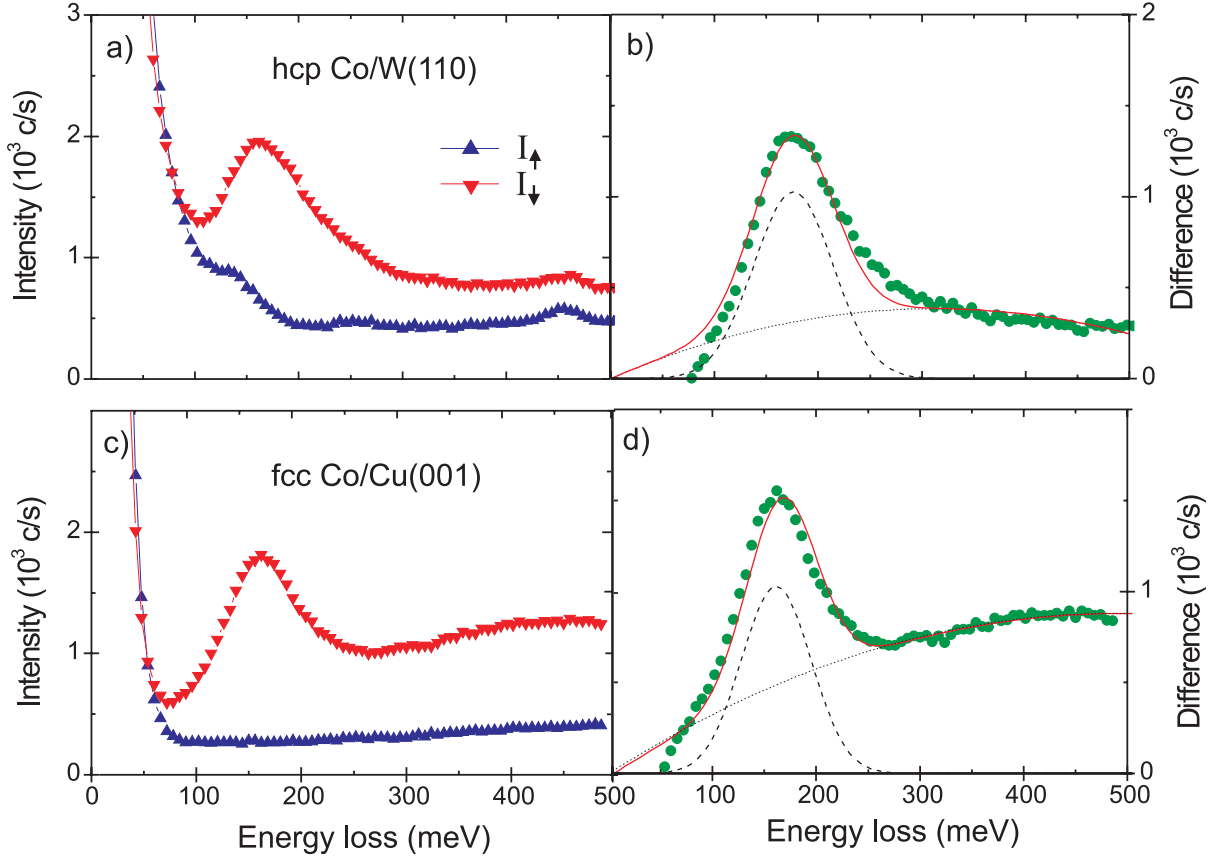
Figure 4.15: In a) SPEEL-spectra and in b) difference spectrum measured on 8 ML hcp Co on W(110) are shown in comparison to spectra obtained on 8 ML fcc Co on Cu(001) shown in c) and d). The spectra for hcp Co were taken with $\Delta K_\parallel = 0.78$ Å^{-1} along $\overline{\Gamma} - \overline{K}$, $E_{kin} = 4$ eV, and $\theta_0 = $ -80° and for fcc Co with $\Delta K_\parallel = 0.78$ Å^{-1} along $\overline{\Gamma} - \overline{X}$, $E_{kin} = 6.5$ eV, and $\theta_0 = 90°$. The red solid curves in b) and d) are fits to the difference spectra. The dashed and the dotted lines show the separate contributions of the spin wave and the background obtained from fitting.

intensity scale one can see that the measured spin wave intensity is of the order of a few percent of the elastic peak, again. As in Fig. 4.15 a), small amounts of adsorbates cause additional loss features in the spectra.

The spectra of the hcp Co-films were measured at a kinetic energy of the incident electrons of $E_{kin} = 4$ eV. As already discussed, the measured spin wave intensities on fcc Co strongly depend on the incident electron energy. We have also measured the spin wave intensities in hcp Co for different E_{kin} and a fixed wave vector transfer of $\Delta K_\parallel = 0.88$ Å^{-1}. The result is shown in Fig. 4.17. In these studies, the influence of the film thicknesses and the scattering conditions were also investigated. Generally, the spin wave intensities in hcp Co on W(110) show a similar behavior as a function of E_{kin} as the one in fcc Co on Cu(001). Again, the highest intensities were measured with low energy electrons. The
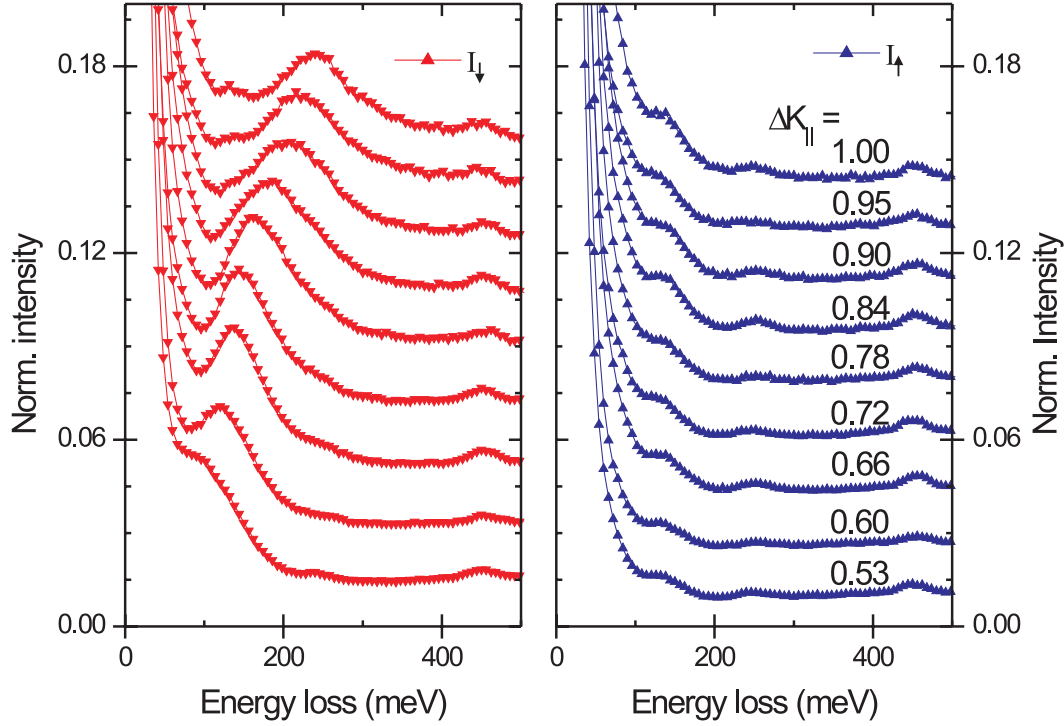
Figure 4.16: Series of spectra measured on 8 ML hcp Co on W(110) for different wave vector transfers indicated by numbers in the $I_\uparrow$-spectra. The intensity of each spectrum was normalized to the elastic intensity and adjacent spectra have been shifted by one minor tick. All spectra shown were taken with $E_{kin} = 4$ eV, and $\theta_0 = -80°$.

energy position of the high spin wave intensities is slightly shifted to lower energies in the case of Co on W(110). Fig. 4.17 shows that the absolute intensity values depend on the scattering conditions. The general behavior, however, stays the same. Several parameters influence the measured spin wave intensities. The parameter space consists of at least E_{kin}, $\Delta K_\parallel$, θ_0 and parameters of the material scattered from, like crystallographic and electronic structures. Since the effect is of unclear origin and a theoretical description is not available, such a large parameter space is an experimental challenge. Finding the optimum conditions for a particular scan is a task of at least several days. To allow maximum comparison between different spectra, an incoming energy of $E_{kin} = 4$ eV was chosen for the investigation of Co on W(110), wherever possible. Due to this relatively low primary energy, the available wave vector transfer range is limited to $|\Delta K_\parallel| = 1.06$ Å^{-1}, in our geometry. Assuming bulk lattice constants in the hcp Co-film, the surface Brillouin zone boundary $\overline{K}$ is at 1.64 Å^{-1}. For spectra taken with high wave vector transfers, we used $E_{kin} = 25$ eV and $\theta_0 = -90°$.

To compare changes in the SPEEL-spectra measured with different incoming electron energies, Fig. 4.18 shows spectra taken with $E_{kin} = 4$ eV and $\Delta K_\parallel = 1.06$ Å^{-1} (Fig. 4.18 a) and b)) and $E_{kin} = 25$ eV and $\Delta K_\parallel = 1.12$ Å^{-1} (Fig. 4.18 c) and d)). The spectra measured with $E_{kin} = 4$ eV look rather similar to the spectra shown in Fig. 4.16, except

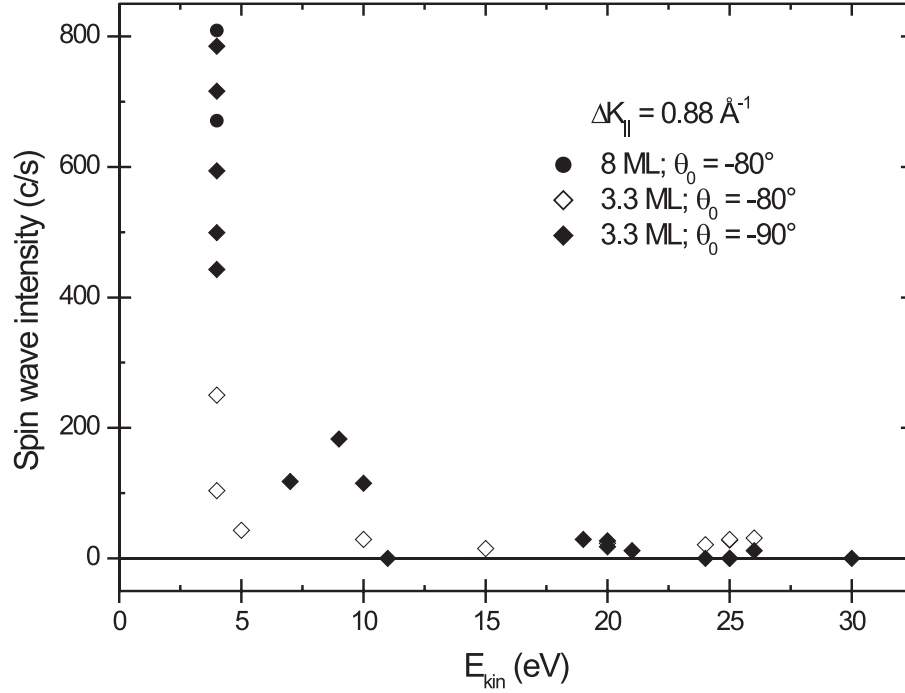Figure 4.17: Spin wave intensity as a function of E_{kin} of the incoming electrons for hcp Co on W(110). All spectra were measured at $\Delta K_{\parallel} = 0.88$ Å^{-1}. The influence of the film thickness and the scattering geometry was also investigated.

for the shift of the spin wave loss feature to higher energies resulting from the dispersion. The spectra measured with $E_{kin} = 25$ eV differ significantly from the spectra measured with $E_{kin} = 4$ eV. The intensity spectra shown in Fig. 4.18 c) are dominated by vibrational losses of H (140 meV) and CO (240 meV). Due to the similar energies of the CO-vibration and the spin wave, the spin wave loss appears only as a small shoulder in the CO-peak in the $I_{\downarrow}$-spectra. The spin wave loss is better visible in the difference in Fig. 4.18 d). The intensity of the loss peak is about a factor of seven smaller than the loss peak in the difference spectrum measured with $E_{kin} = 4$ eV. This ratio between the spin wave loss peaks depends on the wave vector transfer (see for example Fig. 4.17). In general, the spin wave signal is significantly reduced in the spectra taken with $E_{kin} = 25$ eV. Not only the spin wave signal changed for different E_{kin}, but also the intensity of vibrational losses. The change in the intensity of the H-vibrational loss may be related to additional contaminations that were adsorbed during the five times longer measurement for the spectra in Fig. 4.18 c). The CO-vibration, however, is not visible in the spectra in a) and vis-versa the small H_2O-peak is not present in the spectra in c). This could be attributed to the different excitation probability of different vibrational losses as a function of E_{kin}. Another effect is the variation of the background of electron hole pairs as a function of E_{kin}. The background of the spectra shown in Fig. 4.18 changes drastically, quantitatively as well as qualitatively.

To measure the spin wave dispersion in this system, several spectra for different wave
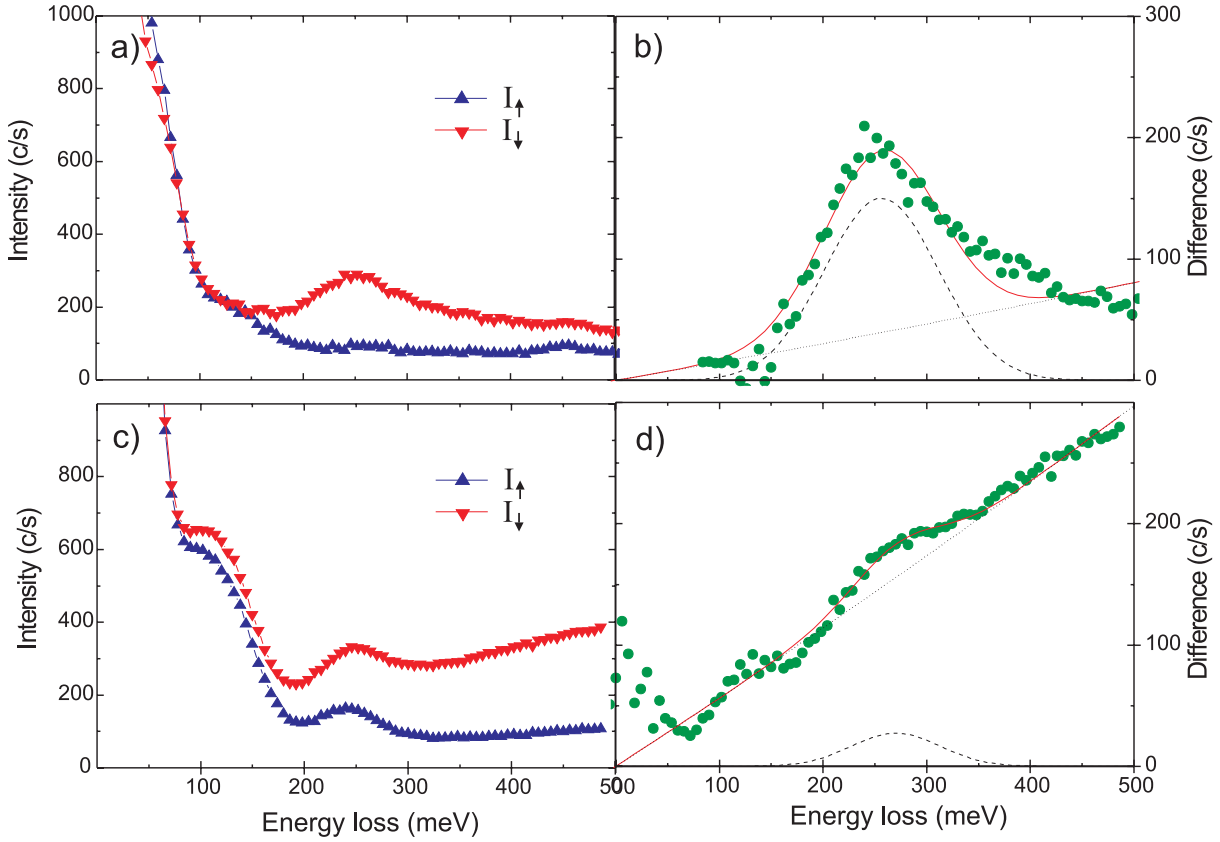
Figure 4.18: a) SPEEL-spectra and b) difference spectra for 8 ML Co on W(110) for $E_{kin} = 4$ eV, $\Delta K_{\parallel} = 1.06$ Å^{-1} and $\theta_0 = -80°$, and c)-d) for $E_{kin} = 25$ eV, $\Delta K_{\parallel} = 1.12$ Å^{-1} and $\theta_0 = -90°$. For the spectra in a), each data point is averaged over 10 s and in c) over 50 s. In the latter case, a longer averaging time was needed to allow a clear identification of the spin wave, despite the lower signal.

vector transfers were recorded. For wave vector transfers below 0.6 Å^{-1}, the spectra were measured with a higher energy resolution (Δ E $\leq$ 25 meV) of the spectrometer. This allowed a better separation of the spin wave loss peak from the foot of the elastic peak. The resulting dispersion determined from the measurements is shown in Fig. 4.19. The dispersion shows that for hcp Co much higher spin wave energies are measured than for fcc Co. The large error bars for spin wave energies in region C are caused by the low spin wave intensities in the SPEEL-spectra in this region. The low intensity is due to the combined effect of a drop of excitation probability with both larger E_{kin} and higher wave vector transfer.

One can calculate the dispersion relation for the hcp crystal within the nearest neighbor Heisenberg model as described in chapter 2.2.1. For the surface mode of a semi-infinite hcp crystal along $\overline{\Gamma} - \overline{K}$ one obtains

$$E_{SW}(Q_{\parallel}) = \frac{16}{3} JS[3 - \cos(a_0 Q_{\parallel}) - 2\cos(\frac{a_0 Q_{\parallel}}{2})]. \tag{4.3}$$
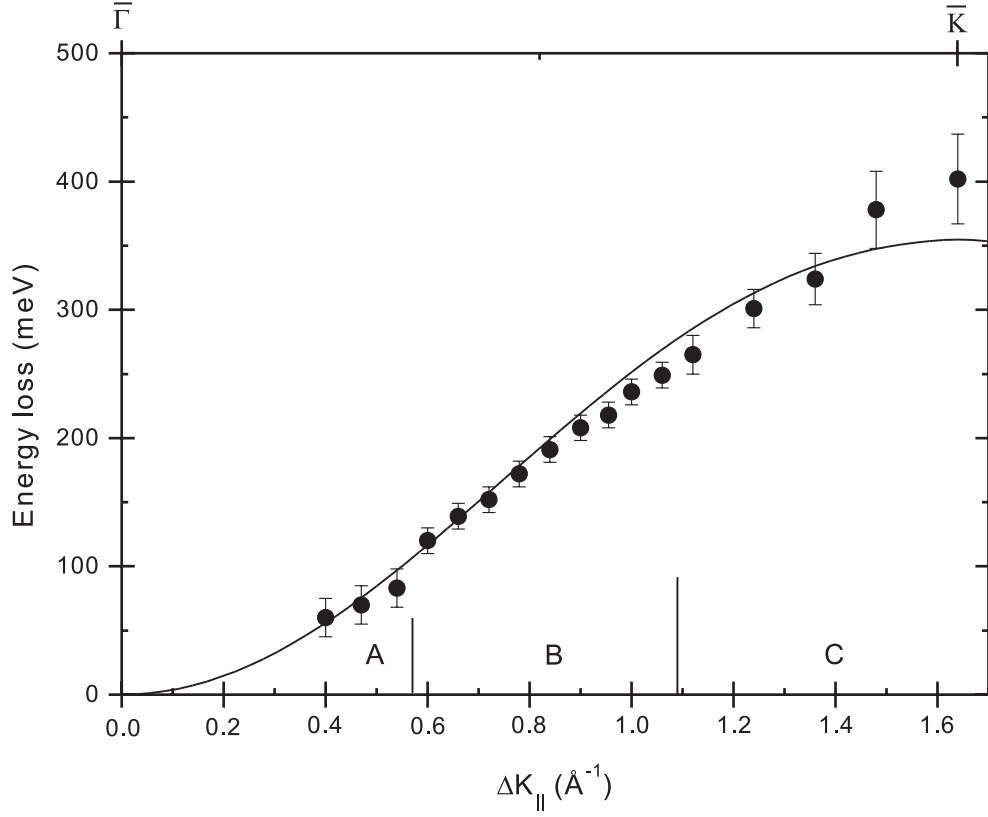
Figure 4.19: Spin wave dispersion of 8 ML Co on W(110) measured by SPEELS. The spectra for the wave vector ranges labeled with A, B, and C have been scanned with different parameters. In region A: E_{kin} = 4 eV and spectrometer energy resolution ΔE = 20-25 meV; in B: E_{kin} = 4 eV and $\Delta E \approx 40$ meV; and in C: E_{kin} = 25 eV and $\Delta E \approx 40$ meV. The solid line represents a fit to the data with the dispersion of the surface mode of a semi-infinite crystal calculated within a nearest neighbor Heisenberg model (see text for details).

This dispersion relation has been fitted to the measured data. The result is added as a black line in Fig. 4.19. From the fit of the measured dispersion, we obtain a value of JS = 14.8±1 meV. The agreement between the experimental data and the Heisenberg model is fairly good. The value of JS is similar to the value obtained from the dispersion in fcc Co on Cu(001). Because of the more extended surface Brillouin zone in hcp Co, the spin wave energies at high wave vectors are higher compared to fcc Co. The value of JS obtained from Co on W(110) is in relatively good agreement to neutron scattering experiments performed on bulk hcp Co. A detailed comparison between our data and the results obtained by other techniques is given in section 5.4.

From the measured spectra at different wave vector transfers one can determine the spin wave intensity and width as a function of this parameter. Because of the different conditions used, it is, however, difficult to combine the information over the complete
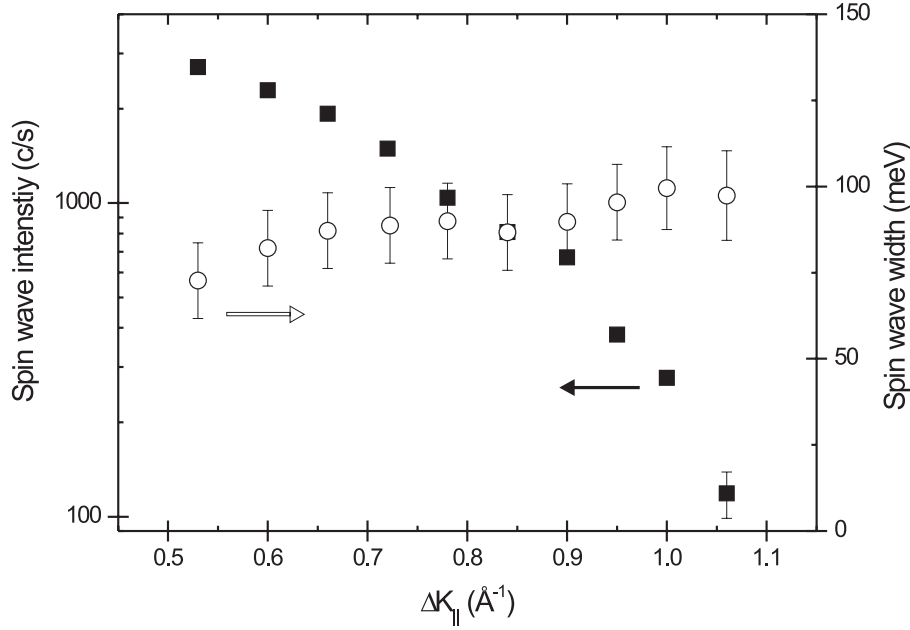
Figure 4.20: Spin wave intensity and spin wave width for different wave vector transfers measured on 8 ML Co on W(110) by SPEELS. Note that the spin wave intensity scale is logarithmic. The data points were taken from range B shown in Fig. 4.19. All points were measured with $E_{kin} = 4$ eV, $\theta_0 = -80°$.

measured wave vector range. Therefore, in Fig. 4.20 the spin wave intensities and widths are shown only for the intermediate wave vector range (range B in Fig. 4.19). In the other ranges, similar observations were made. The drop in the spin wave intensities with increasing wave vector transfer is large, as in the case of Co on Cu(001). Also the absolute values of the spin wave intensities measured on fcc Co with $E_{kin} = 7$ eV and $\theta_0 = 90°$ (see Fig. 4.8) are similar to the one obtained for hcp Co on W(110) measured with $E_{kin} = 4$ eV and $\theta_0 = 80°$ (see Fig. 4.20). The width of the spin wave loss feature is constantly higher by about 15 meV in hcp Co compared to fcc Co.

As has been mentioned already, we also studied the influence of some adsorbates on the spin waves measured by SPEELS. So far, studies have been performed for H_2, O_2 and CO adsorbed on the Co-surface. By increasing the amount of adsorbates in small steps from clean to saturated surfaces, it was possible to study the response of the spin waves in detail. Here, SPEELS is particularly suited, because it allows the simultaneous measurement of spin wave excitations and vibrational losses. The main result of these studies is that the spin wave intensities can be largely suppressed by adsorbing high amounts of O_2 or CO. The spin wave intensity was found to decrease approximately linear with the increase of the intensity of the vibrational loss of these adsorbates. For the adsorption of H only little effects on the measured spin wave loss feature were found. These studies are not part of the present work, therefore, details will be published elsewhere [130]. It should, however, be mentioned again that these studies reveals little if any changes of the inherent

properties of the spin waves (i.e. energy and width) for the small amounts of adsorbates present in the spectra shown here.

Chapter 5

Discussion

The results presented in the previous chapter showed that high wave vector and high energy spin waves can be studied by SPEELS. Several strong arguments support the view that the loss feature in the spectra can be attributed to spin wave excitations. These arguments are summarized in the following section. In section 5.2, the results of our investigations are treated. The experimental data are discussed in the framework of the nearest neighbor Heisenberg model in section 5.3. The results of the SPEELS-measurements are then compared to experimental findings obtained by other methods in section 5.4. At the end, our experimental results are discussed in the context of several recent theoretical studies of spin wave excitations.

5.1 Evidence of spin wave signals in the SPEEL-spectra

A rigorous proof that the measured loss feature in the SPEEL-spectra are correlated to the excitation of spin waves requires the analysis of the spin of the scattered electrons. These measurements are not possible in our current experimental set-up. Several experimental facts, however, support the interpretation of the loss feature as caused by spin wave excitations. The sum of these experimental findings can be considered as a proof.

As we have seen in the spectra shown in chapter 4, the scattering probability of several excitations depend on the spin of the incoming electrons. The expected dependence of the spin wave excitations is exceptional, because spin waves can solely be excited by incident electrons that have a spin of minority character. This spin selective excitation was indeed found for the loss feature under investigation. By reversing the magnetization of the sample, it was also confirmed that the spin selectivity is of magnetic origin (see Fig. 4.4). The unique spin selectivity of the excitation process is the fingerprint of a spin wave.

A second indication that the loss features are spin waves is the strong dispersion of the measured excitations. This dispersion is expected for spin waves. Also the measured energy loss range, from zero to a few hundred meV, is typical for spin waves in 3d-metals. Phonon excitations for example show a dispersion as well, but the phonon energies are

relatively low. In the case of Co-films on Cu(001), the maximum phonon energy is below 30 meV [131, 132].

The third point which supports our interpretation is the agreement between our experimental data and other experimental and theoretical results for spin waves in Co. This agreement is very satisfying within the approximations made. In addition, we observed similar loss features in SPEELS-measurements on Fe. Thus, the effect is not limited to Co.

Each of the above mentioned arguments is a strong indication towards the interpretation of the loss feature as spin wave excitations. The sum of the three gives a solid basis for this interpretation. Therefore, we believe to have proven that by inelastic electron scattering one is able to study high wave vector spin waves in ultrathin films.

5.2 SPEELS-investigation of high wave vector spin waves

A compact representation of the main results of the SPEELS-measurements is a contour plot of the measured intensity of the spin waves as a function of the wave vector and energy transfer.

Fig. 5.1 shows a contour plot of the spin wave losses obtained from the spectra shown in Fig. 4.6 measured on 8 ML fcc Co on Cu(001). The plotted intensity shows the difference of the $I_\downarrow$- and $I_\uparrow$-spectra after the substraction of the electron hole pair background. Here, the lines connect points of the same intensity in energy and wave vector space. They are interpolated linearly between the measured points. Each crossing point of the underlying grid corresponds to a measured data point.

The contour plot allows to follow how the spin wave excitations evolve in the spectra with increasing wave vector transfers. For low wave vectors, the spin wave losses start as an intense and relatively narrow feature and they end as low intensity broad humps at high wave vectors. The dispersion derived from the nearest neighbor Heisenberg model for JS = 15 meV is added as a red solid line in Fig. 5.1. As already shown, this dispersion matches the measured dispersion nicely (compare also Fig. 4.7). Deviations between the experimental data and the calculated dispersion occur mainly for high wave vectors on the negative wave vector side. In this region, these deviations can be partially related to the underestimation of the background of electron hole pair excitations by the fitting routine (see for example Fig. 4.3).

In principle, the contour plot shown in Fig. 5.1 contains the complete measured information about the spin wave excitations in the system. The interpretation of this graph is, however, rather difficult. For example, the excitation mechanism of the creation of a spin wave by an electron is unknown. Therefore, the drop of the spin wave intensity for higher wave vectors can be related to either a drop the of excitation probability or a drop of the spin wave intensity itself. As will be discussed later in more detail, the drop can be assumed to be mainly caused by the scattering process itself. The unknown excitation process also leads to the difficulty that spectra taken at different scattering conditions
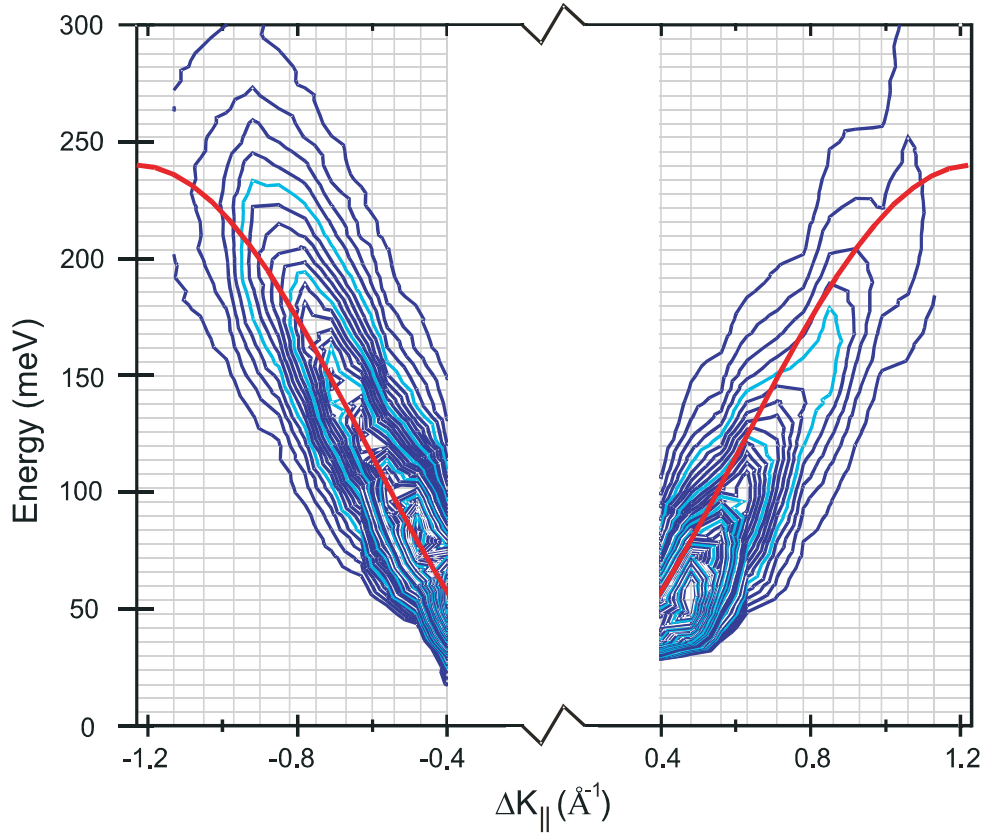
Figure 5.1: Contour plot of the spin wave intensities measured by SPEELS. The graph represents the difference spectra measured on 8 ML Co on Cu(001) from which the background of electron hole pair excitations was subtracted. The original spectra were shown in Fig. 4.6. The blue lines connect points of the same intensity. Between the measured points, the intensity was linearly interpolated. The density of the measured data is illustrated by the underlying grid. Between adjacent dark (light) blue contour lines the intensity changes by 200 (1000) counts per second. The outermost contour line marks the intensity of 200 counts per second. The red line represents the surface spin wave dispersion derived from the nearest neighbor Heisenberg model for JS = 15 meV (see also Fig. 4.7).

cannot be transformed one into each other. Therefore, in the graph shown in Fig. 5.1 only spectra are presented which were taken with the same E_{kin} and θ_0. Nevertheless, Fig. 5.1 gives a good summary of the results obtained by the SPEELS-measurements on fcc Co.

In many of the spectra shown in chapter 4, the spin wave intensities and therefore the observed probability of an electron to scatter from a spin wave was rather large. Typically, the spin wave intensity is of the order of a few hundred to a few thousand counts per second (see Fig. 4.8). As has been shown by the normalized intensity scale (for example in Fig. 4.2), the intensity of the spin wave signal is typically of the order

of a few percent of the intensity of the elastic peak. The total background intensity can be calculated by integrating the background signal over the entire energy range up to the incident electron energy. The total background intensity is of the same order of magnitude as the intensity of the elastically scattered peak. Therefore, in the measured $I_{\downarrow}$-spectra about one electron of 100 to 1000 detected electrons was scattered from a spin wave. For the moment we assume that a similar relation holds over the entire wave vector range. For metals, typically a few percent of the incoming electrons are reflected from the sample. Therefore, we can estimate the probability that an incoming electron of minority character is scattered from a spin wave to be about 10^{-4}. Another approach can be used to estimate the probability that a spin wave is excited from an incoming electron. One can estimate the total spin wave intensity in the available wave vector space by extrapolating the measured spin wave intensities. In this approach, one has to consider the finite energy and wave vector resolution of the spectrometer. The resulting total spin wave intensity has to be divided by the incoming electrons flux of about 50 nA which corresponds to about $3*10^{11}$ electrons per second. From this estimation a similar probability of about 10^{-4} results.[1] Both estimations can be treated as an upper limit because close to the specular condition, other scattering mechanisms may play an important role which will suppress the relative spin wave intensities. The estimation is also only valid for low primary energies of the incoming electrons. At other primary energies, we observed orders of magnitude lower excitation probabilities (see Fig. 4.9 and Fig. 4.17).

The enhancement of the spin wave intensity at low energies and the new spectrometer are the reasons, why spin waves appear prominently in the shown spectra. There are three explanations why in "normal" EELS-studies (using an unpolarized electron beam) such features were never observed. The most obvious reason is the missing spin information in these studies which does not alow to separate spin wave losses from other excitations. In these studies, the experimental interest lay typically on vibrational losses and the spectrometers were used with much high energy resolution at the expense of intensity. Because the spin wave losses are intrinsically broad, the spin wave signals obtained with these settings would be hardly distinguishable from the background. In addition, only few EELS-studies systematic investigated the impact scattering regime [133]. With the knowledge obtained from the present work, however, it seems possible to study spin waves also with a standard EELS. Such measurements could be used for example to extent the investigations of spin waves to lower energy losses.

As has been discussed above, the rigorous proof that the loss features in the spectra are related to spin wave excitations requires the analysis of the spin of the scattered electrons. In principle, with the available count rates of a few thousand counts per second and the latest generation of spin analyzers, a "complete" experiment seems feasible. A new experimental set-up to accomplish this task is in planning [134].

Several experiments in the present work were performed to investigate the process of an electron scattered by the excitation of a spin wave. In the following the results from these investigations are summarized.

---

[1]In this estimation, the transmission probability of the analyzer enters the calculation. The two estimations agree best, when the transmission probability is in between 1 and 0.1, which seems reasonable.

The interaction that allows the excitation of spin waves by electron scattering is the exchange interaction [76]. The probability of an exchange process is known to decrease with increasing incident electron energy [82, 85]. Mills and Hong have calculated the spin dependent inelastic mean free path in ferromagnetic metals. They have explicitly considered exchange processes that lead to the excitation of electron hole pairs and of spin waves [135, 136]. In their calculations, they found a strong increase in the probability of exchange processes for minority electrons at low incoming electron energies. These findings are in qualitative agreement with our results. Therefore, the measured enhancement of the spin wave intensities at low energies of the incoming electrons can in principle be explained by the energy dependence of the exchange processes.[2] The calculations predict, however, that exchange processes of electrons with energies greater than 5 eV above E_F (that is equivalent to $E_{kin} \approx 0$ eV in our experiments) mainly lead to Stoner excitations. In these calculations, spin wave excitations are probable only for primary energies lower than the work function. This energy regime is not accessible to SPEELS-experiments. Although the energy dependence of the exchange process seems to be described correctly in the theoretical calculations, the probability to excite a spin wave by exchange processes appears to be underestimated.

The above discussed theoretical results indicate that the measured strong enhancement of the spin wave signals in SPEELS-experiments is caused by the dependence of the exchange processes on the primary energy of the incoming electrons. Quantitatively, however, the theoretical model and the measurements disagree. The model does not quote any explicit correlation between the excitation probability and the wave vector transfer. In the calculations, the bare Coulomb-potential was used in the interaction process. As discussed by the authors, screening effects are modest in the high wave vector transfers region [135, 136]. The cross section for a charged particle scattered from a Coulomb potential of a point charge drops as $\frac{1}{\sin^4(\frac{\alpha}{2})}$, where α is the angle of deflection of the incoming electron [137]. We have used this dependence as a first approach to compare it to the measured drop of the spin wave intensity. The drop in the cross section expected from the bare Coulomb potential for the scattering conditions used in our experiments is shown in Fig. 5.2 as a solid line. The data points presented by solid symbols represent the spin wave intensities measured on 8 ML Co on Cu(001) (see Fig. 4.8). In the calculations, we have assumed that the spin wave peak measured by SPEELS is dominated by surface spin waves, which have $k_\perp = 0$. The agreement is good considering the simplicity of the model, however, one has to note that the cross section is scaled arbitrarily.[3] Nevertheless, the drop of the spin wave intensity with increased wave vector transfer seems to be described well by this model.

---

[2]The theory described above does not include any multiple scattering effects. In separate studies, Mills and coworkers have shown that such multiple scattering effects lead to a periodic modulation of the scattering probability as a function of E_{kin} [89].

[3]One should also mention that not only the excitation process but also a drop of the spin wave intensity itself can lead to a reduction of the measured intensity. The continued decrease of the measured intensity beyond the first surface Brillouin zone indicates that the drop is mainly caused by the reduction of the cross section.
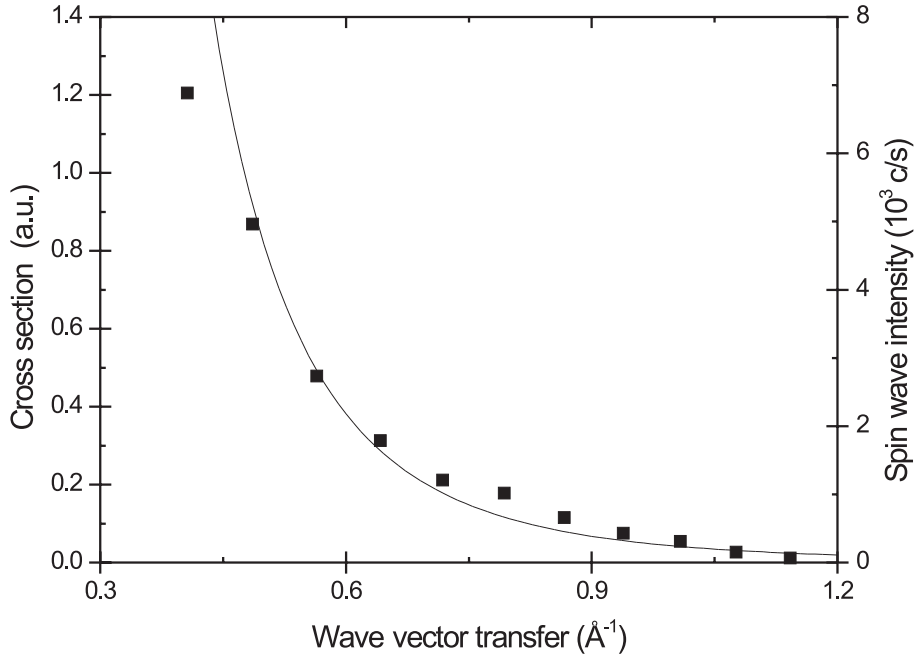
Figure 5.2: Cross section of a charged particle scattered from a Coulomb potential of a point charge as a function of the wave vector transfer (solid line) compared to the spin wave intensities measured on 8 ML Co on Cu(001) (solid symbols) (see text for details).

Another point directly visible from the spectra or from the contour plot shown in Fig. 5.1 is that the measured spin waves are rather broad. For high wave vectors, the ratio of the spin wave energy to the spin wave width is about two to three. This is in agreement with the behavior expected for high wave vector spin waves in itinerant systems, especially at surfaces [36, 51] (for a detailed discussion see 5.5). As has been shown for example in Fig. 4.3, it is possible to fit the spin wave loss feature by one single broad peak of Gaussian shape. In principle, several spin wave modes could contribute to the broad peak, which are smeared out because of damping. The broadening could also be caused by multiple scattering effects where an electron that excites a spin wave is scattered with high probability by other low energy excitations, as well. Some evidences are given in section 5.3 that the measured feature is dominated by a single spin wave mode.

If one assumes that the total width of the spin wave loss feature is reflecting the damping of a single mode, it is straight forward to calculate quantities like the life time of the spin waves. This assumption may be rather crude, however, it should allow an estimation of the order of magnitude. In this approximation, the behavior of the spin wave excitations in real space and time can be calculated from the measured spectra. Fig. 5.3 shows such a representation in space and time for spin waves with $\Delta K_{\parallel} = 0.81$ Å^{-1}. To obtain this representation, one has to perform a Fourier transformation from wave vector
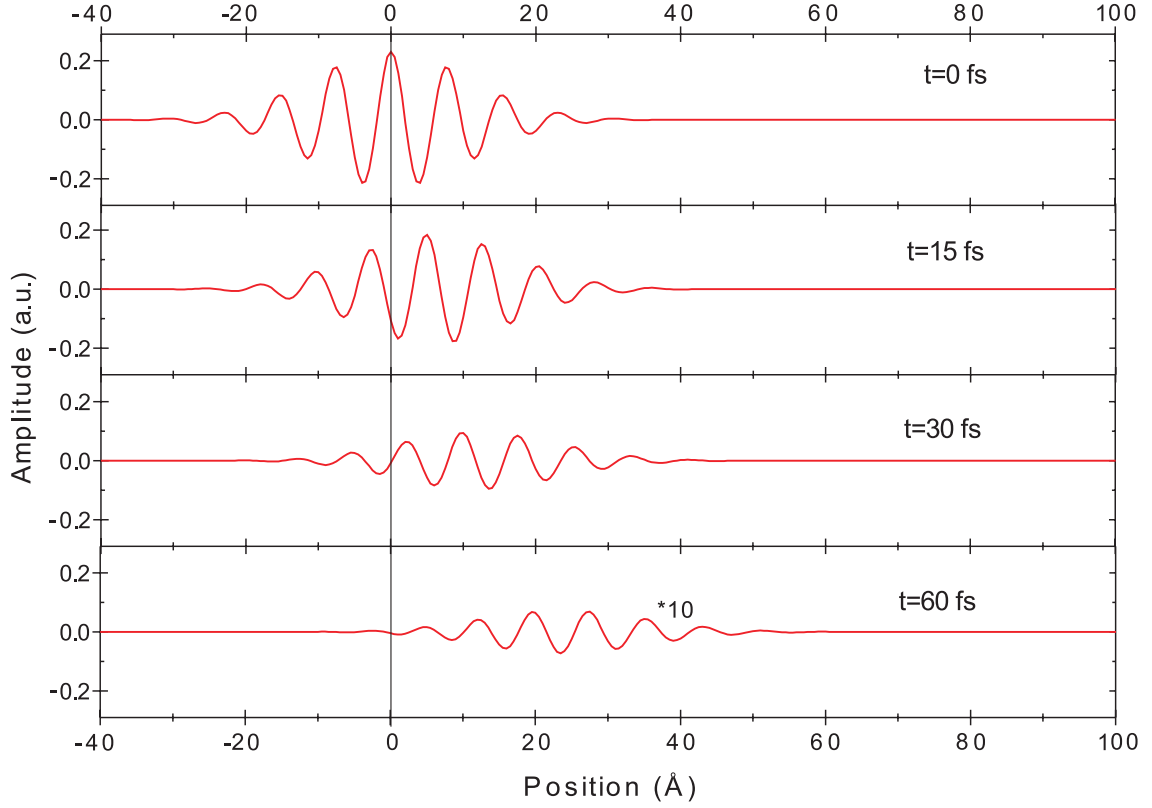
Figure 5.3: Classical representation of the measured spin waves in real space and time obtained from a Fourier transformation of the wave vector/energy data (see text for details). The graph represents a spin wave with $\Delta K_{||} = 0.81$ Å^{-1} in fcc Co. The spin wave is created at time t = 0 and x = 0. Its decay length in space is about 15 Å. The decay time is about 30 fs. The amplitude for the curve at t = 60 fs has been multiplied by a factor of 10.

to real space and from energy to time. For a Gaussian peak one obtains:

$$f(x) = e^{-\left(\frac{x-x_0}{\sigma}\right)^2} \quad \xrightarrow{Fourier} \quad F(y) \propto e^{-\left(y\frac{\sigma}{2}\right)^2} e^{-ixy}. \tag{5.1}$$

For the graphs shown in Fig. 5.3, we have assumed Gaussian peaks in energy and wave vector space which are mirror symmetric around zero.[4] For the Fourier transformation, one has also to consider the link between the wave vector and the energy of the spin waves. The decay in time and space is inversely proportional to the width of the spin wave in energy and wave vector space (see equation 5.1). For the example shown in Fig. 5.3, the amplitude of the spin wave in real space drops to e^{-1} of its initial value after about ≈ 15 Å, only. Since the wavelength is about 8 Å, the spin wave is already damped out after a

---

[4]The latter assumption simplifies the graphical representation, because in this case the Fourier transformed spectrum has no imaginary part. The conclusion drawn from the graphs are not effected by this assumption.

few oscillations. The lifetime of the spin wave is also rather short, about 30 fs. From the dispersion, the group (v_G) and phase velocity (v_P) of the excitation can be calculated by $v_G = \frac{dE}{dq}$ and $v_P = \frac{E}{q}$. For fcc Co at $\Delta K_\parallel = 0.81$ Å^{-1} one obtains values of $v_G \approx 40\frac{km}{s}$ and $v_P \approx 39\frac{km}{s}$. Due to the similar group and phase velocity and the short life time of the spin wave, the spin wave diverges only little in space. By multiplying v_G with the life time, the distance which the center of mass of the spin wave travels can be estimated. It is about 12 Å, which is also visible in Fig. 5.3. This means that the spin wave is highly confined in time and space due to the strong damping. Thus, the spin wave is not the well-defined long living excitation discussed in section 2.2.1.

5.3   Comparison between the SPEELS-data and the Heisenberg model

In this work, the nearest neighbor Heisenberg model was used several times to calculate properties related to spin waves, for example the dispersion. As mentioned in chapter 2, it is believed that this model is applicable to rare earth metals, but not to 3d-ferromagnets. Nevertheless, several aspects of the measured data are in surprisingly good agreement with the model. In this section, a short comparison between the experimental data and the expectations within a nearest neighbor Heisenberg model is given.

As has been shown in the last chapter, in particular the measured dispersion is in excellent agreement to the dispersion of a surface mode calculated within the nearest neighbor Heisenberg model. We attribute this agreement mainly to the fact that deviations between the model and the true system may be taken into account by an effective exchange coupling constant. The Heisenberg model is an adiabatic approach, in which the damping of the spin wave is neglected. Therefore, there is a strong disagreement between this model and our data concerning the spin wave width.

Within the Heisenberg model, one expects N spin wave modes for a thin film of N layer thickness at each wave vector parallel to the surface (see Fig. 2.2). In the SPEELS-measurements, we performed "constant $\Delta K_\parallel$"-scans corresponding to a vertical line in Fig. 2.2. Thus, we should have detected a peak in the spectra at every energy position at which this line crosses a spin wave branch. In our experiments, we do not find any evidence for these structures, except maybe a tiny high energy shoulder in the spin wave peaks (see for instance Fig. 4.3). This could, however, also be attributed to the background.

The above discussion considers only inherent properties of the magnetic system and neglects the excitation process. As shown in Fig. 5.2, the measured spin wave intensity drops significantly over the measured wave vector range. It was shown in the last section that this drop in the spin wave intensity can be described by a drop of the cross section for a charged particle scattering from a Coulomb potential.[5] The essential argument is that the excitation probability drops with increasing the three dimensional wave vector

---

[5]For the following arguments, the knowledge of the exact dependence of the excitation probability on the wave vector transfer is not necessary. Other functions that are able to interpolate monotonically between the measured data points would yield similar results.
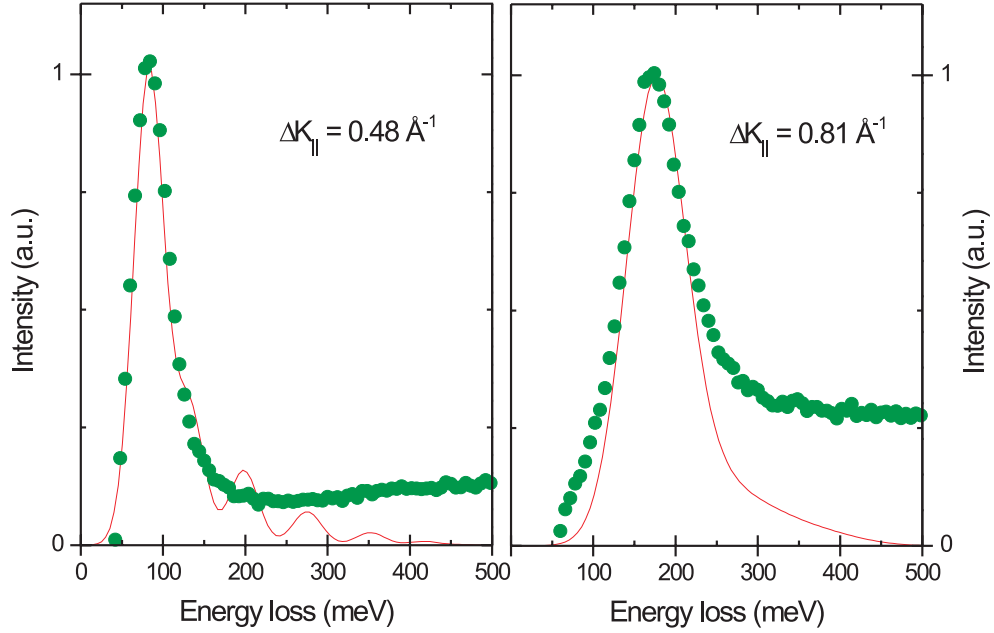
Figure 5.4: Difference spectra (green points) of 8 ML fcc Co and calculated spin wave intensity for $\Delta K_\parallel = 0.48$ Å^{-1} in a) and $\Delta K_\parallel = 0.81$ Å^{-1} in b). The spin wave intensities were calculated within the Heisenberg model by weighting each spin wave mode by its amplitude at the surface layer and a factor that takes into account that the spin wave intensity drops with increasing wave vector (see text for details). The spin wave modes have been artificially broadened to approximate the measured width. The original measured SPEEL-spectra from which the difference spectra were taken are shown in Fig. 4.6.

$|\Delta k|$. The acoustic surface mode has only a $\Delta K_\parallel$-component, whereas all other modes have additional $\Delta k_\perp$-components and thus a higher $|\Delta k|$. This means, the drop of the cross section is expected to result in a smaller intensity of the higher energy modes in the measured spectra. In addition, not every mode has the same amplitude in the surface layer. Since SPEELS is a surface sensitive technique, it seems reasonable to weight the excitation probability of each mode by the corresponding amplitude at the surface.[6] By taking into account the scattering process, one can then calculate a SPEEL-spectra from the Heisenberg model. The result of these calculations in the case of an 8 ML fcc Co-film is shown in Fig. 5.4 for two wave vector transfers. To allow a comparison, the difference spectra measured for the same wave vector transfers are added. For the calculated spectra, the spin wave intensity is scaled and the spin wave width is artificially broadened so that the width of the surface mode fits the measured spin wave width. The main result of Fig. 5.4 is that within the assumptions made, also the spectra calculated from a Heisenberg

---

[6]Equation 2.11 contains information about the eigenvalues (ω) and the eigenvectors (A) of a spin wave mode, wave vector and layer resolved. The square of the eigenvector gives the amplitude of this mode in each layer [20].

model are dominated by the surface modes. The agreement is rather satisfying and perfect agreement cannot be expected from this model. The above mechanism gives a possible explanation why the measured SPEEL-spectra are dominated by one single mode. As will be discussed later, more elaborated calculations show that high energy spin wave modes are also intrinsically strongly suppressed in the system, due to damping [20].

In conclusion, the results of the nearest neighbor Heisenberg model are generally in good agreement to the experimental data. Disagreement is mainly found in the broad measured spin wave width indicating strong damping. Since the Heisenberg model is an adiabatic model, one expects a peak of zero width. Of course, the agreement between the measured dispersion and the predictions of an effective nearest neighbor Heisenberg model does not guaranty that the underlying physics is properly taken into account within this model. Up to now, other available theoretical approaches have relatively large uncertainties, for example concerning the calculated dispersion. Therefore, when a model description is necessary in this work, the Heisenberg model is used due to its easy handling and missing alternatives.

5.4   Comparison between spin waves measured by SPEELS and by other experimental techniques

In the following, the results of this work are compared to other experimental investigations of spin waves. Since SPEELS is a new technique to study spin waves and explores spin waves in a region which has not been accessible to other techniques, a direct comparison is difficult. INS is the only technique which allows the study of a similar wave vector range as the one investigated by SPEELS. Thus, the following comparison will focus on the results obtained by INS. The measurement of spin wave excitations with high wave vector transfers by INS is not an easy task in 3d-ferromagnets, due to the high spin wave energies in these systems. Therefore, only a few INS-studies have been performed on this subject.

In the case of fcc Co, which is not stable in bulk at room temperature, no INS experiments that examine high wave vector spin waves have been published. For this system, we limit the discussion to single crystal alloys, that contain a few percent of Fe [128, 129] to stablize the fcc phase at room temperature. Because in these studies only low wave vector transfers were measured, one way to compare the results from these measurements with our data is to use the nearest neighbor Heisenberg model. The values of JS obtained from neutron scattering on bulk fcc Co (using crystals with 8% and 6% Fe) are JS = 14.7 ±1.5 meV [128, 129]. This is in excellent agreement with the value of JS = 15 ± 1 meV obtained by SPEELS.

For bulk hcp Co, only one publication exists where the spin wave dispersion was measured up to high wave vector transfers [59]. The results of this measurement were shown in Fig. 2.4. A comparison between the spin wave dispersion obtained by this INS-
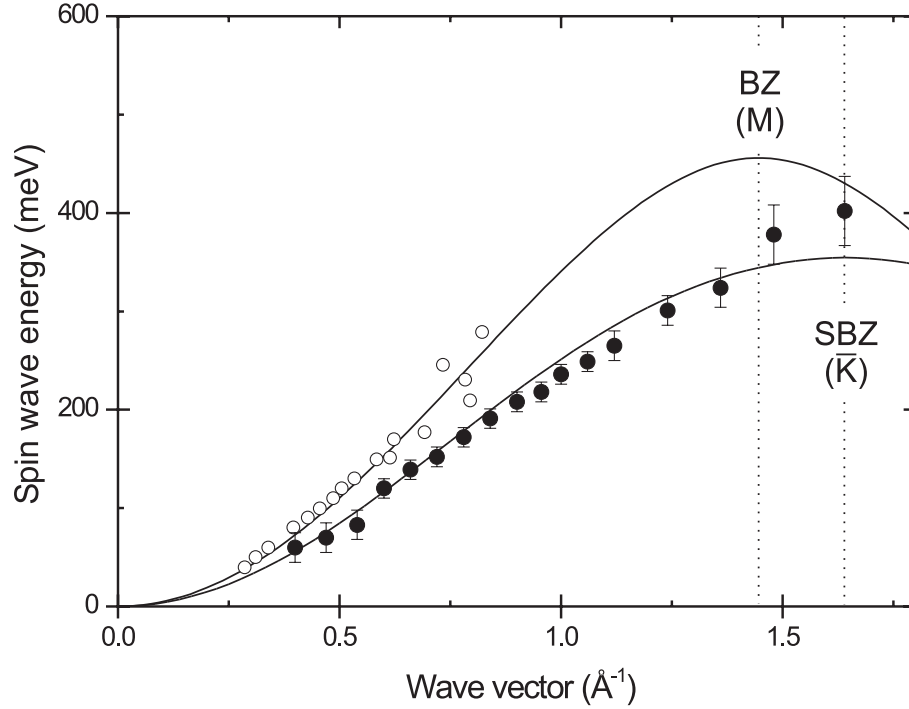
Figure 5.5: Comparison between the spin wave dispersions measured by SPEELS (●) on 8 ML hcp Co on W(110) along $\overline{\Gamma} - \overline{K}$ and by INS (○) on bulk hcp Co [59] along $\Gamma - M$. The scan directions are along the two different symmetry axes of the basal plane. Note that the x-axis is for two different quantities. In the case of neutron scattering, it marks the three dimensional wave vector transfer, whereas for the electron scattering, it marks the two dimensional in-plane wave vector transfer. In the particular case that the spin waves in SPEEL-spectra are surface spin waves, however, $q_{\perp} = 0$. The (surface) Brillouin zones in the particular directions are marked by (SBZ) BZ. The solid lines in the two curves are fits of the dispersions derived within the nearest neighbor Heisenberg model.

experiment [59] and the data obtained by SPEELS on hcp Co is shown in Fig. 5.5.[7] The SPEELS-data show the spin wave dispersion of the surface mode along $\overline{\Gamma} - \overline{K}$ while the neutron measurements show the dispersion of the bulk spin wave mode along $\Gamma - M$ [59]. These are the two different symmetry directions in the basal plane. The spin wave energies obtained by INS lie at higher energies. To compare the two different modes along the different directions in more detail, we use the nearest neighbor Heisenberg model, again. A fit of the neutron data with the bulk dispersion yields a value of $JS = 19.2\pm0.6$ meV (see Fig. 5.5) [59]. For the SPEELS-data we obtain $JS = 14.8\pm1$ meV. Within the Heisenberg model, it is also possible to estimate the influence of the different crystallographic

---

[7]The wave vector axis represents a three dimensional vector in the case of the neutron experiments and a two dimensional vector for the SPEELS-measurements. It is, however, possible to compare the two dispersions assuming that the spin wave peak measured by SPEELS is dominated by the surface spin wave mode for which $q_{\perp} = 0$.

directions on the spin wave dispersion. In the case of an isotropic exchange[8], no drastic changes are expected for the wave vector range investigated by INS. Also the bulk and surface modes are at similar energies at these wave vector transfers. Therefore, within the Heisenberg model the differences between the two data sets are mainly caused by the differences in JS. One could speculate about possible reasons for this deviation, like the different properties of thin films and bulk Co. Considering the differences in the two experiments, however, in our view the agreement is rather satisfying. One should note that even within the results obtained by different INS-studies on hcp Co (typically for lower wave vectors) the observed values for JS range from 17.3 meV to 20.2 meV, see Ref. [59, and references therein].

Another important point is the amount of Co used in the experiments to detect spin wave losses. In the case of INS-measurements, about 100 g of single crystalline Co was used to obtain the data shown in Fig. 5.5 [59]. As we have seen, high wave vector spin waves can be studied by SPEELS on a few atomic layers of Co. The electron beam used in the experiments has a lateral extension of about 1 mm^2. Therefore, the amount of material scattered from is about a factor of 10^{10} different between both experiments. For much lower wave vector and energy transfers, it is possible to reduce the amount of material needed in INS drastically. One example is the work of Schreyer and colleagues [6]. They have studied spin waves using only about 10 mg Dy [6]. Nevertheless, this amount of material is still higher by a factor of 10^6 compared to the SPEELS-experiments.

By BLS and FMR the exchange stiffness D can be measured in magnetic films. Within the nearest neighbor Heisenberg model, one can determine JS from D (see equation 2.17). In Ref. [139], BLS measurements were performed on about 100 nm thick Co-films of different crystalline structures. The authors found values of JS = 17.9±0.6 meV for fcc and JS = 17.3±1.4 meV for hcp Co. Therefore, in qualitative agreement to our data, no changes of JS were found for the different Co-structures. The reported absolute values for JS, however, are higher than what was obtained by SPEELS. Other BLS-studies report values of JS = 13.5±3 meV [140] and JS = 18.3±2.8 meV [141]. The low value reported in Ref. [140] was obtained by BLS-measurements on poly-crystalline films. In a FMR-study also a low value of JS = 13.5±0.7 meV was measured on poly-crystalline Co-films [74]. One may speculate that these low values are partially due to the film quality. In general, the agreement between the BLS- and FMR-results and SPEELS-data is fairly good. One should consider the difference of about two orders of magnitude in the investigated wave vector range and the uncertainty introduced by the Heisenberg model.

In summary, to compare the experimental findings obtained by the above mentioned techniques[9], the different wave vector regimes or the differences between surface and bulk

---

[8]This seems to be a reasonable approximation, because the basal plane has a sixfold symmetry and even in fourfold symmetries the anisotropy in the exchanges are typically very small [138].

[9]One should maybe mention once more the variety of interactions used to excite spin waves by these different techniques. In INS the spin of the neutron couples to the spin wave, while in FMR the coupling is to an externally applied magnetic field. In BLS the electrical field of the photon couples by the spin-orbit interaction. In electron scattering, the excitation takes place by an exchange process. The properties of the spin waves are intrinsic, of course, and do not depend on the excitation process.

spin waves have to be considered. This is possible in the nearest neighbor Heisenberg model. Within this model, fairly good agreement between all experimental results is obtained. Typically, the deviations of the literature values to our experimental findings are of the same size as the deviations of literature values among themselves. Generally, the SPEELS-values tent to lie slightly below the values obtained by other techniques.

5.5 Comparison between the SPEELS-data and theoretical calculations

In this section, the results of the spin wave excitations measured by SPEELS are compared to theoretical calculations. The section is split into two parts. In the first part, the experimental data are compared to theoretical models that rely on the adiabatic approximation. In the second part, theories that go beyond this approximation are discussed. It is widely accepted that calculations using the adiabatic approximation may only give a crude estimate for high wave vector spin waves in 3d-ferromagnets [36, 44]. Nevertheless, most calculations are performed within this approximation, because it is non trivial to go beyond. Several recent ab initio calculations map itinerant magnetism on an effective Heisenberg model to calculate the spin wave dispersion. This allows a direct comparison between the calculated exchange coupling constants and the experimental findings, as well as a comparison between the dispersion relations. Because no damping is included in these theories, they fail to predict the correct broad spectral shape of the measured spin waves. Calculations that examine spin wave properties in thin films regularly obtain a strong enhancement of the exchange coupling constant in the surface layer, see for example Ref. [20, 42, 45, 142]. To the best of our knowledge, no calculations for thin hcp Co films have been published. Therefore, the discussion is limited to fcc Co. In their calculations, Pajda and coworkers found an enhancement of the nearest neighbor exchange coupling constant for one ML Co on Cu(001) of about a factor of two compared to the bulk value [42, 143]. In calculations by Razee et al. [45], it was observed that this enhancement persists in the surface layer for films up to 7 ML Co-thickness. Other exchange coupling constants, as well as the magnetic moment are also enhanced close to the surface [45]. These effects are, however, typically much smaller than a factor of two. SPEELS seems especially suited to study such effects, because the energy of surface spin waves at high wave vectors strongly depends on the strength of the exchange coupling at the surface. As we have seen in chapter 4, we are able to describe our measured dispersions for both, fcc and hcp Co, by the nearest neighbor Heisenberg model using only one value of JS for all film thicknesses investigated. Within the description of the Heisenberg model, we therefore do not find any evidence for such an enhancement of the exchange coupling constant at the surface. As has been discussed in the last section, the spin wave energies measured by SPEELS are typically lying slightly below the ones measured by other techniques. Following the above argument, we can bring our data in perfect agreement to other experimentally observed values of JS by assuming that the exchange coupling constant is reduced at the surface. If the exchange coupling constant at the surface is
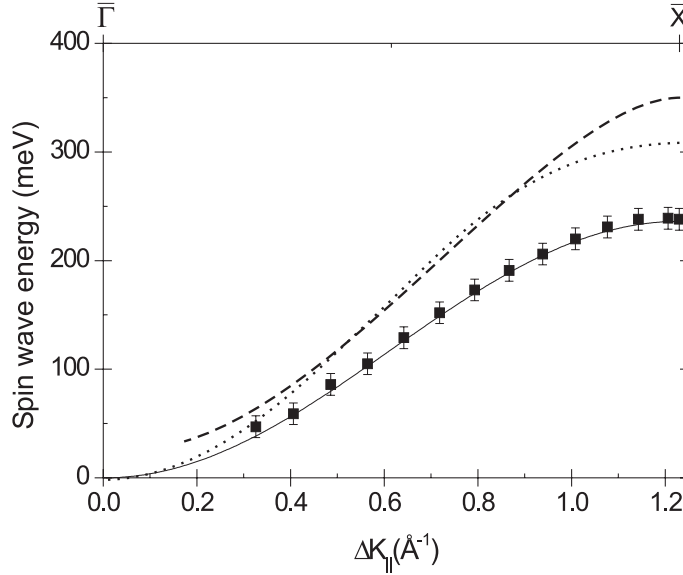
Figure 5.6: The dashed and the dotted lines show the calculated spin wave dispersions for 8 ML Co [20] and 1 ML Co [44] on Cu(001), respectively. Both models used an ab initio calculated electronic structure and the adiabatic approximation. The SPEELS-data (■) are shown together with a the fit from the nearest neighbor Heisenberg model (solid line)

different from the bulk value, then our experimental findings point in the direction of a reduction and not of an enhancement. It was also shown in Fig. 4.13 that the spin wave energy does not change for lower temperatures. Hence, the difference between experimental values and theoretical expectations cannot be explained by temperature effects. The entire argument is, however, based on the nearest neighbor Heisenberg model, which limits possible conclusions. For a more detailed discussion see Ref. [12].

Since the theoretically predicted enhancement of the surface exchange is not observed in the experiments, it can be expected that the surface spin wave energies are overestimated in the calculations. The dispersion curves that have been calculated for fcc Co on Cu(001) within the adiabatic approximation are shown in Fig. 5.6 together with the measured data. The dashed line represents the dispersion calculated by Costa and colleagues [20] for 8 ML Co on Cu(001). In this calculation, an enhanced surface exchange coupling is present. The dotted line shows the dispersion calculated by Udvardi and coworkers [44] for one ML Co on Cu(001). In this publication, no statement was made about the surface exchange coupling. As visible, both calculations overestimate the spin wave energies in the high wave vector range. When comparing the calculations of Ref. [44] to our measured data, one has to note that the calculations were performed for one ML Co. From the crude argument of the number of nearest neighbors, one would expect an increase of the spin wave energy at the surface Brillouin zone boundary by a factor of two between a one ML thick and thicker films. The dispersion taken from Ref. [20] displays the "optical" surface mode, see also Fig. 2.2 for comparison. Thus, as the wave vector decreases to zero, the spin wave energy remains finite instead of approaching zero. For
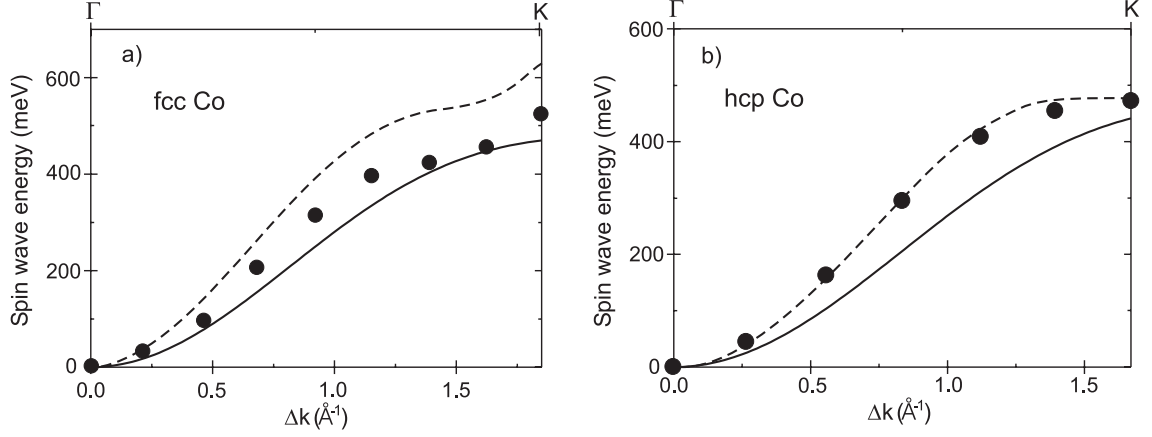
Figure 5.7: Dispersion curves for bulk fcc (a)) and for bulk hcp Co (b)). In a) the calculations are taken from Ref. [143] (dashed line) and Ref. [40] (points) and in b) from Ref. [43] (dashed line) and Ref. [40] (points). Within the Heisenberg model, the bulk dispersion can be calculated from the surface dispersion measured by SPEELS. This curves are shown as solid lines.

this reason, the dispersion is difficult to compare with the measured data in this range. As already discussed, for the high wave vector range the overestimation of the spin wave energies is rather high. It is interesting to note that using the exchange coupling constant of the sub-surface layers for the entire film, the spin wave energies at the surface Brillouin zone boundary would lie very close to the measured one.

The SPEELS-data can also be compared to calculations of bulk dispersions, if one assumes the validity of the transformation of the surface to the bulk dispersion within the nearest neighbor Heisenberg model. The resulting dispersion estimated from our experimental results is shown in Fig. 5.7 as solid lines. In all theoretical calculations shown in Fig. 5.7, the dispersion was calculated by ab initio methods using the adiabatic approximation. In general, all calculated dispersions tent to moderately overestimate the spin wave energies compared to the predictions of our effective Heisenberg model. The agreement to our data is fairly good considering that the calculations were done fully ab initio. A more detailed discussion seems difficult at this point, because of the uncertainty introduced by the conversion of the surface spin wave mode into the bulk mode by the nearest neighbor Heisenberg model.

So far, the experimental results were compared to theories using the adiabatic approximation. It has already been discussed that this approximation is expected to fail for high wave vector spin waves in the itinerant electron systems. As was pointed out by Mills and coworkers [20, 36, 51], the results from calculations within and beyond the adiabatic approximation can differ qualitatively as well as quantitatively. Full ab initio calculations of the dynamical spin susceptibility including the itinerant character of the underlying electron system have been performed for bulk systems [37], but not for Co. Currently, the calculations seem to be computationally too demanding to be extended to thin films.

In the case of Co, only a few theoretical publications are available that treat the spin
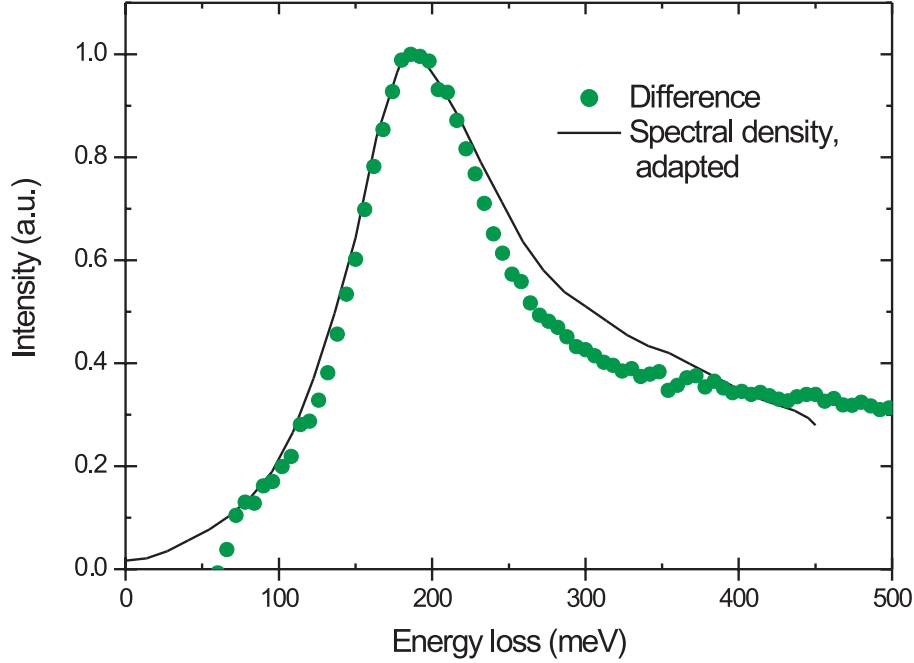
Figure 5.8: Comparison between the calculated spectral density in the surface layer taken from Ref. [20] (solid line) and the difference spectra measured by SPEELS (dots). For both, the wave vector was about $\Delta K_{\parallel} = 0.85$ Å^{-1}. The calculated spectrum is shifted by 50 meV to lower energies and both quantities are normalized to one at their maximum.

wave excitations within a non adiabatic approach [20, 48, 54]. All of them are based on an empirical tight binding description of the electronic structure, with parameters chosen by fitting to ab initio calculated electronic structures. One of the studies [48] has been performed for hcp bulk Co. The result of this study is that high wave vector spin waves are significantly damped, as indicated by a broadening of the structures. Nevertheless, the spin wave energies are similar to the energies shown in Fig. 5.7 b), which were calculated by theories using the adiabatic approximation [40, 43]. Two recent calculations for thin fcc Co films on Cu(001) have been stimulated by our experiments [20, 54]. The calculated quantity in these publications is the layer resolved spectral density of spin fluctuations as a function of the wave vector. This quantity is directly proportional to the imaginary part of the transverse spin susceptibility. The calculations in Ref. [20] illustrate the changes in the spectra shape within and beyond the adiabatic approximation. In the latter case, the spectra shape deviates strongly from the expectations derived from the Heisenberg model except for low wave vectors. For higher wave vectors, the spectral density in the non adiabatic description consists of one single broad feature, instead of several discrete modes as expected from the Heisenberg model. Only some structure in the broad feature reminds of these modes. This behavior is in qualitative agreement with the spectra measured by SPEELS and provides a quite natural explanation of the broad spin wave loss features. This is the strong damping of the spin waves caused by Stoner excitations. It is important
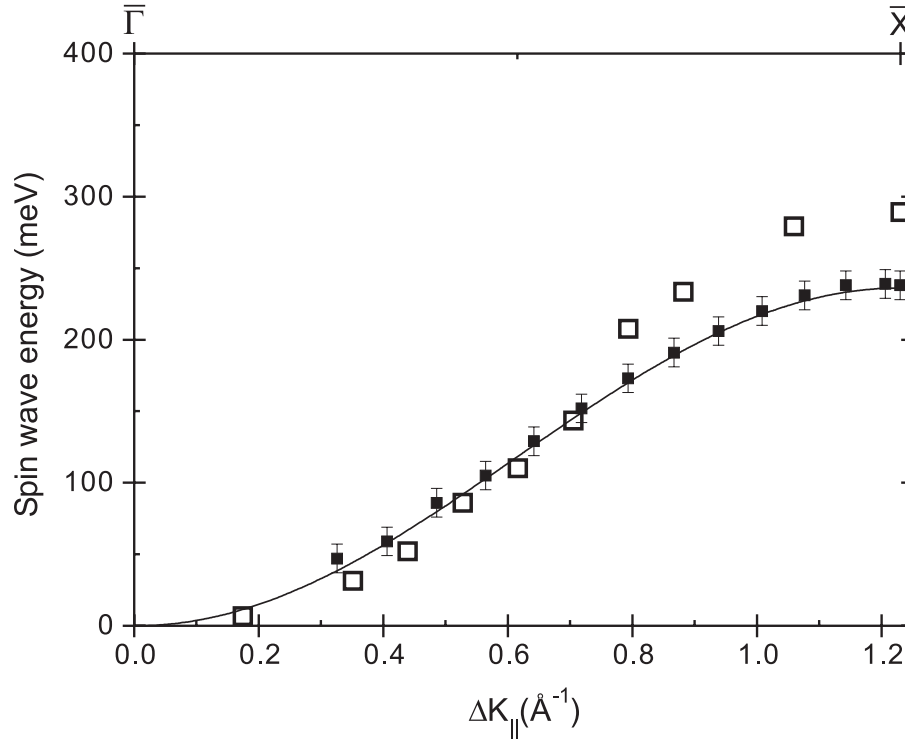
Figure 5.9: The dispersion obtained by the calculations of the spectral density of spin excitations taken from Ref. [20] (□) in comparison to our experimental data (■). The open squares of the theoretically calculated dispersion mark the position of the maximum of the calculated spectral density.

to mention that the spectral density is a quantity that is solely a property of the spin waves and does not take into account the actual excitation process. This leads to two effects, when comparing these calculations to the measured SPEELS-data. As has been shown by Mills and coworkers [144, 145], the spectral weight of Stoner excitations as measured by electron scattering is underestimated in the calculations. In addition, the effect of the reduction of the cross section for higher wave vectors is not included in the theoretical description. In Fig. 5.8, the calculated spectral density in the surface layer for a wave vector of $\Delta K_\parallel = 0.85$ Å^{-1} is compared to the measured difference spectrum taken at about the same wave vector. The calculated peak is shifted to lower energies by 50 meV and the maxima of both curves are scaled to one. The shape of the two spectra is in promising agreement. The high energy shoulder in the calculations is slightly higher in intensity than the measured one. The effect is stronger for lower wave vector transfers and may be attributed to the cross section dependence of the spin wave excitation (see section 5.3). As has been mentioned by the authors in Ref. [20], it is difficult to assign a particular spin wave mode to a structure in the calculated spectral density. In these calculations, however, the lowest energy features are always located in the surface layers. This indicates that a significant part of the low energy spectral density within the surface layer can be

attributed to what has been a well-defined surface spin wave mode in the Heisenberg model. Therefore, these calculations at least do not contradict the interpretation that the loss features measured by SPEELS are dominated by contributions of surface spin waves. One has to mention that the measured difference spectra cannot directly be related to the calculated spectral density. The calculation consider only the $e^{\downarrow\uparrow}$-spin channel. In the measured difference all spin channel contribute. This is expected to lead to differences especially concerning the background in the two cases. Nevertheless, the good agreement between the theoretical and experimental results allow two conclusions. The measured width of the loss peak can to a good extent be reproduced by the calculations. This suggests that the effect of the damping of spin waves by Stoner excitations seems to be taken into account correctly in the theory. The other way around, the agreement with the shape of the calculated spectral density supports the assumption that the loss features in the measured spectra are solely caused by spin wave excitations.

In Ref. [20] also the dispersion of the spin fluctuations is calculated. For this, the position of the maximum in the spectral density in the surface layer is plotted as a function of the wave vector. The resulting calculated dispersion and the dispersion measured by SPEELS is presented in Fig. 5.9. The agreement between the two dispersions is rather satisfactory, however, as has been discussed in detail in Ref. [20], small changes in the choice of the tight binding parameters can change the calculated spin wave energies by a factor of two [20, 54]. Thus, at the current stage of the theory, it is difficult to obtain reliable values from it. Here, full ab initio calculations going beyond the adiabatic approximation would be highly desirable.

Chapter 6

Conclusion and Outlook

In this work, a clear proof was given that spin waves with high energy and momentum can be studied by spin-polarized electron energy loss spectroscopy. In the SPEEL-spectra, the spin waves appear as pronounced loss features. These losses showed a strong dispersion as expected for an acoustic spin wave branch. The SPEELS-measurements allowed the investigation of the spin wave dispersion up to the surface Brillouin zone boundary. The thinnest film under investigation in these studies was only 2.5 atomic layers thick. Therefore, by SPEELS one has access to the "terra incognita" of high wave vector spin waves in thin films. Using SPEELS, we were able investigate spin waves at wave vector transfers about two orders of magnitude higher than what has been accessible by established techniques for thin film studies. Compared to inelastic neutron scattering, several orders of magnitude less magnetic material is required for a detectable spin wave signal. From the good signal to noise ratio observed in the SPEELS-measurements, the detection of high wave vector spin waves in one ML of magnetic material seems possible.

Up to now, different crystalline phases of Co and Fe have been studied by SPEELS, but in this work we concentrated on fcc and hcp Co. The two different phases have been stabilized by the substrates Cu(001) and W(110), respectively. In general, in both systems similar properties of the measured spin wave excitations were found.

High spin wave intensities were measured under certain conditions. A rough estimation of the upper limit shows that about 1 of 10^4 incoming electrons leaves the crystal after the excitation of a spin wave. The probability to excite spin waves by inelastic electron scattering was found to be strongly dependent on the primary energy of the incoming electrons. High spin wave intensities were measured only for primary energies below about 10 eV. The increased probability to scatter via the creation of a magnetic excitation at these low energies can be explained by the dependence of the exchange processes on the primary energy. The results of calculations that examine the energy dependence of exchange processes in electron scattering are, however, only in qualitative agreement to the experimentally observed behavior [135, 136]. In the experiments a drop of the measured spin wave intensity was also found with increasing wave vector transfer. This drop can be explained by the scattering process, as well. In addition, the spin wave intensity was found to be depended on the scattering geometry.

The measured spin waves are intrinsically broad. As expected from bulk measurements [59] and from non adiabatic theoretical descriptions [20, 48, 49, 54], the spin waves seem to be strongly damped by the decay into Stoner excitations.

As discussed above, the spin wave losses showed a pronounced dispersion. For wave vector transfers up to about 0.8 Å^{-1} the spin wave energies in fcc and hcp Co-films are similar. For higher wave vectors, differences in the dispersion occur due to the different crystalline structures. As a result, the dispersions at higher wave vectors become drastically different. The measured spin wave dispersions in both systems are in good agreement with the dispersion of a surface spin wave mode derived from a nearest neighbor Heisenberg model. The product of the effective exchange coupling constant and the magnetic moment is JS = 15 ± 1 eV in the case of fcc Co and JS = 14.8 ± 1 eV in the case of hcp Co. From our measurements, we conclude that the value of JS is independent of the film thickness (in the range of 2.5-8 ML) within the given accuracy. As discussed in the following, the value is similar to the bulk value of JS, too.

A comparison between our measured spin wave energies and the results obtained by other experimental techniques is possible within the nearest neighbor Heisenberg model. Presuming that the spin wave losses in the SPEEL-spectra are dominated by surface spin waves, in general a good agreement to literature values was found [59, 128, 139]. The deviations are surprisingly small considering the differences in the experiments and the different spin wave regimes probed.

All these agreements were only found assuming that the spin wave losses in the SPEEL-spectra are dominated by surface spin waves. Also the thickness dependence of the spin wave energies found for fcc Co can be explained in this context. We have introduced a phenomenological model based on simple considerations of the excitation process by including a wave vector dependent excitation probability and the surface localization of each mode. This model showed that one expects a dominating contribution of the surface modes in the SPEEL-spectra. More elaborate calculations provide similar conclusions [54].

Theoretical calculations of the spin wave dispersion typically overestimate the spin wave energies compared to our measured data. This is especially the case in calculations performed for thin film systems. Here, the theory predicts an enhancement of the exchange coupling at surfaces. In our experiments, however, we found no sign of such an enhancement. The agreement to ab initio calculations for bulk samples is fairly good considering that no adjustable parameters are included in these calculations. These models rely on the adiabatic approximation and therefore cannot describe the measured broadening of the spin wave peaks. In a recent calculation using a dynamical theory that goes beyond the adiabatic approximation, Mills and coworkers studied the spectral density of spin excitations in thin Co-films. The calculations are in good qualitative agreement to the measured data. The theoretical description is, however, based on an empirical tight binding model and it has been shown that the calculated dispersion varies drastically for small changes of the parameters [54]. Full ab initio calculations for thin Co-films that go beyond the adiabatic approximation are desirable.

From the experimental results presented in this work, several future studies seem possible. Other magnetic materials have spin wave energies that are high enough to be

studied by SPEELS, provided that the spin wave intensities are similar to Co. To make use of the spin selective excitation, one only needs a defined magnetization direction at the surface. Therefore, SPEELS-studies of spin waves can possibly be performed even on uncompensated surfaces of antiferromagnets. The study of spin waves by a "complete" SPEELS experiment, using a spin-polarized source and a spin detector, seems possible as well, because of the high spin wave intensities found. Since the feasibility to study spin waves by inelastic electron scattering is now proven, the investigation of spin waves using a "standard" EELS should be straightforward. The higher energy resolution possible in these experiments, may allow measurements of spin waves at lower energies.

In addition, we found that the excitation probability of some vibrational losses are spin depended. In most cases, the dependence is weak, however, for certain geometries it can be of the order of 10% (and possibly stronger). A systematic study of these phenomena may lead to a better understanding of both, the electronic structure of the adsorbates and the excitation process involved.

We hope that the presented work will stimulate further experimental and theoretical efforts in the field of spin waves with high energy and high momentum.

Bibliography

[1] M. Jullière, Phys. Lett. **54A**, 225 (1975).

[2] G. Binasch, P. Grünberg, F. Saurenbach, and W. Zinn, Phys. Rev. B **39**, 4828 (1989).

[3] M. N. Baibich, J. M. Broto, A. Fert, F. Nguyen Van Dau, F. Petroff, P. Eitenne, G. Creuzet, A. Friederich, and J. Chazelas, Phys. Rev. Lett. **61**, 2472 (1988).

[4] B. Hillebrands and K. Ounadjela, Spin Dynamics in confined magnetic structures I, in *Topics in applied Physics, Vol. 83*, Springer Verlag, Berlin Heidelberg New York, 2002.

[5] B. N. Brockhouse, Phys. Rev. **106**, 859 (1957).

[6] A. Schreyer, T. Schmitte, R. Siebrecht, P. Bödeker, H. Zabel, S. H. Lee, R. W. Erwin, C. F. Majkrzak, J. Kwo, and M. Hong, J. Appl. Phys. **87**, 5443 (2000).

[7] M. Henzler and W. Göpel, *Oberflächenphysik des Festkörpers*, Teubner Verlag, Stuttgart, 1994.

[8] R. E. DeWames and L. A. Vredevoe, Phys. Rev. Lett. **18**, 853 (1967).

[9] J. Kirschner, private communication .

[10] M. Plihal, D. L. Mills, and J. Kirschner, Phys. Rev. Lett. **82**, 2579 (1999).

[11] R. Vollmer, M. Etzkorn, P. S. Anil Kumar, H. Ibach, and J. Kirschner, Phys. Rev. Lett. **91**, 147201 (2003).

[12] M. Etzkorn, P. S. Anil Kumar, R. Vollmer, H. Ibach, and J. Kirschner, Surf. Sci. **566-568**, 241 (2004).

[13] R. Vollmer, M. Etzkorn, P. S. Anil Kumar, H. Ibach, and J. Kirschner, J. Magn. Magn. Mater. **272-276**, 2126 (2004).

[14] R. Vollmer, M. Etzkorn, P. S. Anil Kumar, H. Ibach, and J. Kirschner, J. Appl. Phys. **95**, 7435 (2004).

[15] R. Vollmer, M. Etzkorn, P. S. Anil Kumar, H. Ibach, and J. Kirschner, Thin Solid Films **464-465**, 42 (2004).

[16] C. Kittel, *Introduction to solid state physics, seventh edition*, John Wiley and Sons, Inc., New York Chichester Brisbane Toronto Singapore, 1996.

[17] D. L. Mills, in *Surface excitations*, edited by M. Agranovich and R. Loudon, volume 9 of *Modern problems in condensed matter science*, Chap. 3, Elesevier Science Publishers B. V., North-Holland Amsterdam, 1984.

[18] W. Heisenberg, Z. Phys. **38**, 411 (1926).

[19] M. G. Cottam and A. N. Slavin, in *Linear and nonlinear spin waves in magnetic films and superlattices*, edited by M. G. Cottam, Chap. 1, World Scientific, Singapore New Jersey London Hong Kong, 1994.

[20] A. T. Costa, R. B. Muniz, and D. L. Mills, Phys. Rev. B **70**, 54406 (2000).

[21] F. Bloch, Z. Phys. **61**, 206 (1930).

[22] F. Bloch, Z. Phys. **74**, 295 (1932).

[23] W. Nolting, *Quantentheorie des Magnetismus II*, Teubner Verlag, Stuttgart, 1986.

[24] The programm to calculate the spin wave dispersion in a magnetic slab was kindly provided by R. Vollmer .

[25] R. E. DeWames and T. Wolfram, Phys. Rev. **185**, 720 (1969).

[26] E. C. Stoner, Proc. Roy. Soc. A **154**, 656 (1936).

[27] E. C. Stoner, Proc. Roy. Soc. A **165**, 372 (1938).

[28] P. Mohn, *Magnetism in the solid state*, Springer series in solid-state sciences 134, Springer Verlag, Berlin Heidelberg, 2003.

[29] J. C. Slater, Phys. Rev. **52**, 198 (1937).

[30] D. H. Martin, *Magnetism in solids*, MIT Press, Cambridge, 1967.

[31] C. Herring and C. Kittel, Phys. Rev. **81**, 869 (1951).

[32] C. Herring, Phys. Rev. **87**, 60 (1952).

[33] C. Herring, in *Exchange interactions among itinerant electrons*, edited by G. T. Rado and H. Suhl, Vol. IV of Magnetism, Academic Press, New York London, 1966.

[34] K.-P. Kämper, D. L. Abraham, and H. Hopster, Phys. Rev. B **45**, 14335 (1992).

[35] D. R. Penn and P. Apell, Phys. Rev. B **38**, 5051 (1988).

[36] H. Tang, M. Plihal, and D. L. Mills, J. Magn. Magn. Mater. **187**, 23 (1998).

[37] S. Y. Savrasov, Phys. Rev. Lett. **81**, 2570 (1998).

[38] M. I. Katsnelson and A. I. Lichtenstein, Phys. Rev. B **61**, 8906 (2000).

[39] S. Frota-Pessôa, R. B. Muniz, and J. Kudrnovský, Phys. Rev. B **62**, 5293 (2000).

[40] S. V. Halilov, H. Eschrig, A. Y. Perlov, and P. M. Oppeneer, Phys. Rev. B **58**, 293 (1998).

[41] M. van Schilfgaarde and V. P. Antropov, J. Appl. Phys. **85**, 4827 (1999).

[42] M. Pajda, J. Kudrnovský, I. Turek, V. Drchal, and P. Bruno, Phys. Rev. Lett. **85**, 5424 (2000).

[43] O. Grotheer, C. Ederer, and M. Fähnle, Phys. Rev. B **63**, 100401 (2001).

[44] L. Udvardi, L. Szunyogh, K. Palotás, and P. Weinberger, Phys. Rev. B **68**, 104436 (2003).

[45] S. S. A. Razee, J. B. Staunton, L. Szunyogh, and B. L. Györffy, Phys. Rev. B **66**, 094415 (2002).

[46] J. F. Cooke, J. A. Blackman, and T. Morgan, Phys. Rev. Lett. **54**, 718 (1985).

[47] J. A. Blackman, T. Morgan, and J. F. Cooke, Phys. Rev. Lett. **55**, 2814 (1985).

[48] K. N. Trohidou, J. A. Blackman, and J. F. Cooke, Phys. Rev. Lett. **67**, 2561 (1991).

[49] J. M. Bass, J. A. Blackman, and J. F. Cooke, J. Phys.: Condens. Matter **4**, L275 (1992).

[50] J. Hong and D. L. Mills, Phys. Rev. B **61**, R858 (2000).

[51] R. B. Muniz and D. L. Mills, Phys. Rev. B **66**, 174417 (2002).

[52] R. B. Muniz, A. T. Costa, and D. L. Mills, J. Phys.: Condens. Matter **15**, S495 (2003).

[53] A. T. Costa, R. B. Muniz, and D. L. Mills, Phys. Rev. B **68**, 224435 (2003).

[54] A. T. Costa, R. B. Muniz, and D. L. Mills, Phys. Rev. B **69**, 064413 (2004).

[55] D. McKinzie Paul, P. W. Mitchell, H. A. Mook, and U. Steigenberger, Phys. Rev. B **38**, 580 (1988).

[56] H. A. Mook, D. Mck. Paul, and S. Hayden, Phys. Rev. B **38**, 12058 (1988).

[57] M. Yethiraj, R. A. Robinson, D. S. Sivia, J. W. Lynn, and H. A. Mook, Phys. Rev. B **43**, 2565 (1991).

[58] T. G. Perring, A. T. Boothroyd, D. McK. Paul, A. D. Taylor, R. Osborn, R. J. Newport, J. A. Blackman, and H. A. Mook, J. Appl. Phys. **69**, 6219 (1991).

[59] T. G. Perring, A. D. Taylor, and G. L. Squires, Physica B **213-214**, 348 (1995).

[60] G. P. Felcher, Phys. Rev. B **24**, 1595 (1981).

[61] E. Balcar and S. W. Lovesey, Theory of magnetic neutron and photon scattering, in *Oxford Series on neutron scattering in condensed matter*, Vol. 2, Oxford Science Publications, Oxford New York Tokyo, 1989.

[62] C. Kittel, *Quantum Theory of the solids, secound edition*, John Wiley and Sons, Inc., New York Chichester Brisbane Toronto Singapore, 1987.

[63] R. Kubo, T. Izuyama, D. J. Kim, and Y. Nagaoka, J. Phys. Soc. Jap. **17**, 67 (1962).

[64] T. Izuyama, D. J. Kim, and R. Kubo, J. Phys. Soc. Jap. **18**, 1025 (1963).

[65] H. A. Mook, Spin waves and magnetic excitations, in *Modern Problems in Condensed Matter Sciences*, edited by A. S. Borovik-Romanov and S. K. Sinha, Chap. 7, Vol. 22, Elsevier Science Publisher, North-Holland Amsterdam Oxford New York, 1988.

[66] H. A. Mook and M. D. Paul, Phys. Rev. Lett. **54**, 227 (1985).

[67] J. H. E. Griffiths, Nature **158**, 670 (1946).

[68] C. Kittel, Phys. Rev. **71**, 270 (1947).

[69] B. Heinrich and J. A. C. Bland, *Ultrathin Magnetic Structures II*, Springer Verlag, Berlin Heidelberg New York, 1994.

[70] J. R. Dutcher, Linear and nonlinear spin waves in magnetic films and superlattices, Chap. 6, World Scientific, Singapore New Jersey London Hong Kong, 1994.

[71] L. Brillouin, Ann. Phys. (Paris) **17**, 88 (1922).

[72] M. H. Grimsditch, Light scattering in solids V, volume 66 of *Topics in apllied physics*, Chap. 7, Springer Verlag, Berlin Heidelberg New York, 1989.

[73] J. R. Sandercock and W. Wettling, Soild State Commun. **13**, 1729 (1973).

[74] P. E. Tannenwald and R. Weber, Phys. Rev. **121**, 715 (1961).

[75] M. Grimsditch, A. Malozemoff, and A. Brunsch, Phys. Rev. Lett. **43**, 711 (1979).

[76] R. Feder, *Polarized electrons in surface physics*, World Scientific, Singapore, 1985.

[77] G. Schönhense and H. C. Siegmann, Ann. Phys. **2**, 465 (1993).

[78] M. Getzlaff, J. Bansmann, and G. Schönhense, Solid State Commun. **87**, 467 (1993).

[79] H. Lüth, *Solid surfaces, interfaces and thin films*, Springer Verlag, Berlin Heidelberg New York, 2001.

[80] M. A. van Hove, W. H. Weinberg, and C. M. Chan, Low-energy electron diffraction: experiment, theory and surface structure determination, in *Springer series in surface sciences*, edited by G. Ertl and R. Gomer, Vol. 6, Springer Verlag, Berlin Heidelberg New York, 1986.

[81] J. Kirschner, D. Rebenstorff, and H. Ibach, Phys. Rev. Lett. **53**, 698 (1984).

[82] H. Hopster, R. Raue, and R. Clauberg, Phys. Rev. Lett. **53**, 695 (1984).

[83] H. Ibach and D. L. Mills, *Electron energy loss spectroscopy and surface vibrations*, Academic Press, New York London Paris, 1982.

[84] D. Venus and J. Kirschner, Phys. Rev. B **37**, 2199 (1988).

[85] J. Kirschner, *Polarized electrons in surface physics*, World Scientific, Singapore, 1985.

[86] J. Kirschner, Phys. Rev. Lett. **55**, 973 (1985).

[87] D. L. Abraham and H. Hopster, Phys. Rev. Lett. **62**, 1157 (1989).

[88] G. Vignale and K. S. Singwi, Phys. Rev. B **32**, 2824 (1985).

[89] M. P. Gokhale, A. Ormeci, and D. L. Mills, Phys. Rev. B **46**, 8978 (1992).

[90] M. Plihal, D. L. Mills, and J. Kirschner, Phys. Rev. Lett. **82**, 2579 (1999).

[91] M. R. Vernoy and H. Hopster, Phys. Rev. B **68**, 132403 (2003).

[92] D. T. Pierce and F. Meier, Phys. Rev. B **13**, 5484 (1976).

[93] *Magnetische Schichtsysteme, 30. Ferienkurs des Instituts für Festkörperforschung*, Forschungszentrum Jülich, ISBN 3-89336-235-5, 1999.

[94] H. Ibach, J. Electron Spectrosc. Relat. Phenom. **64/65**, 819 (1993).

[95] H. Ibach, M. Balden, and S. Lehwald, J. Chem. Soc., Faraday Trans. **92**, 4771 (1996).

[96] H. Ibach, D. Bruchmann, R. Vollmer, M. Etzkorn, P. S. Anil Kumar, and J. Kirschner, Rev. Sci. Instrum. **74**, 4089 (2003).

[97] H. Ibach, M. Balden, D. Bruchmann, and S. Lehwald, Surf. Sci. **269&270**, 94 (1992).

[98] H. B. Michaelson, J. Appl. Phys. **48**, 4729 (1977).

[99] B. G. Johnson, P. J. Berlowitz, D. W. Goodman, and C. H. Bartholomew, Surf. Sci. **217**, 13 (1989).

[100] S.-K. Kim, J.-S. Kim, J. Y. Han, J. M. Seo, C. K. Lee, and S. C. Hong, Surf. Sci. **453**, 47 (2000).

[101] P. Drescher, et al., Appl. Phys. A **63**, 203 (1996).

[102] Y. P. Yashin, private communication .

[103] SPES Ltd. Prof. Mamaev, Head SPES Ltd., Polytekhnicheskaja Str. 29, St. Petersburg, Russia.

[104] R. Feder and J. Kirschner, Surf. Sci. **103**, 75 (1981).

[105] M. Plihal, D. L. Mills, H. J. Elmers, and U. Gradmann, Phys. Rev. B **51**, 8193 (1995).

[106] D. Venus, S. Cool, and M. Plihal, Surf. Sci. **446**, 199 (2000).

[107] Landolt-Börnstein, Zahlenwerte und Funktionen, in *vierter Band, Teil 2: Stoffwerte und Verhalten von metallischen Werkstoffen*, Springer Verlag, Berlin Göttingen Heidelberg, 1964.

[108] L. Gonzalez, R. Miranda, M. Salmerón, J. A. Vergés, and F. Ynduráin, Phys. Rev. B **24**, 3245 (1981).

[109] H. Li and B. P. Tonner, Surf. Sci. **237**, 141 (1990).

[110] E. Navas, P. Schuster, C. M. Schneider, J. Kirschner, A. Cebollada, C. Ocal, R. Miranda, J. Cerdá, and P. de Andrés, J. Magn. Magn. Mater. **121**, 65 (1993).

[111] W. Weber, A. Bischof, R. Allenspach, C. H. Back, J. Fassbender, U. May, B. Schirmer, R. M. Jungblut, G. Güntherodt, and B. Hillebrands, Phys. Rev. B **54**, 4075 (1996).

[112] M. T. Kief and W. F. Egelhoff, Phys. Rev. B **47**, 10785 (1993).

[113] R. Pentcheva and M. Scheffler, Phys. Rev. B **61**, 2211 (2000).

[114] A. K. Schmid, D. Atlan, H. Itoh, B. Heinrich, T. Ichinokawa, and J. Kirschner, Phys. Rev. B **48**, 2855 (1993).

[115] F. Huang, M. T. Kief, G. J. Mankey, and R. F. Willis, Phys. Rev. B **49**, 3962 (1994).

[116] S. Ferrer, E. Vlieg, and I. K. Robinson, Surf. Sci. Lett. **250**, L363 (1991).

[117] J. J. De Miguel, A. Cebollada, J. M. Gallego, S. Ferrer, R. Miranda, C. M. Schneider, P. Bressler, J. Garbe, K. Bethke, and J. Kirschner, Surf. Sci. **211/212**, 732 (1989).

[118] H. Knoppe and E. Bauer, Phys. Rev. B **48**, 1794 (1993).

[119] T. Duden and E. Bauer, Phys. Rev. Lett. **77**, 2308 (1996).

[120] M. Partzer, H. J. Elmers, and M. Getzlaff, Phys. Rev. B **67**, 153405 (2003).

[121] H. Fritzsche, J. Kohlhepp, and U. Gradmann, Phys. Rev. B **51**, 15933 (1995).

[122] T. Duden, R. Zdyb, M. S. Altman, and E. Bauer, Surf. Sci. **480**, 145 (2001).

[123] M. Getzlaff, J. Bansmann, J. Braun, and G. Schönhense, J. Magn. Magn. Mater. **161**, 70 (1996).

[124] M. Partzer and H. J. Elmers, Phys. Rev. Lett. **90**, 077201 (2003).

[125] G. Garreau, M. Farle, E. Beaurepaire, and K. Baberschke, Phys. Rev. B **55**, 330 (1997).

[126] R. W. Joyner, J. Rickman, and M. W. Roberts, Surf. Sci. **39**, 445 (1973).

[127] H. Hopster and D. L. Abraham, Phys. Rev. B. **40**, 7054 (1989).

[128] R. N. Sinclair and B. N. Brockhouse, Phys. Rev. **120**, 1638 (1960).

[129] S. J. Pickart, H. A. Alperin, V. J. Minkiewicz, R. Nathans, G. Shirane, and O. Steinsvoll, Phys. Rev. **156**, 623 (1967).

[130] W. Tang, M. Etzkorn, P. S. Anil Kumar, R. Vollmer, and J. Kirschner, to be published .

[131] L. L. Kesmodel, M. L. Xu, and S. Y. Tong, Phys. Rev. B **34**, 2010 (1986).

[132] M. H. Mohamed, J. S. Kim, and L. L. Kesmodel, Surf. Sci. **220**, L687 (1989).

[133] W. Ho, R. F. Willis, and E. W. Plummer, Phys. Rev. Lett. **40**, 1463 (1978).

[134] R. Vollmer and J. Kirschner, private communication .

[135] J. Hong and D. L. Mills, Phys. Rev. B **59**, 13840 (1999).

[136] J. Hong and D. L. Mills, Phys. Rev. B **62**, 5589 (2000).

[137] E. Rutherford, Phil. Mag. **21**, 669 (1911).

[138] H. A. Mook and R. M. Nicklow, Phys. Rev. B **7**, 336 (1973).

[139] X. Liu, M. M. Steiner, R. Sooryakumar, G. A. Prinz, R. F. C. Farrow, and G. Harp, Phys. Rev. B **53**, 12166 (1996).

[140] S. P. Vernon, S. M. Lindsay, and M. B. Stearns, Phys. Rev. B **29**, 4439 (1984).

[141] M. Grimsditch, E. E. Fullerton, and R. L. Stamps, Phys. Rev. B **56**, 2617 (1997).

[142] S. Morán, C. Ederer, and M. Fähnle, to be published .

[143] M. Pajda, J. Kudrnovský, I. Turek, V. Drchal, and P. Bruno, Phys. Rev. B **64**, 174402 (2001).

[144] M. Plihal and D. L. Mills, Phys. Rev. B **58**, 14407 (1998).

[145] A. T. Costa, R. B. Muniz, and D. L. Mills, Phys. Rev. B **68**, 224435 (2003).

Appendix

Danksagung

Deutsche Zusammenfassung

Spinwellen mit hohen Wellenvektoren können in einzelnen dünnen Filmen und an Oberflächen mit den etablierten Standardmethoden nicht untersucht werden. In der vorliegenden Arbeit konnten Spinwellen in diesem Bereich mit Hilfe der spinpolarisierten Elektronenenergieverlustspektroskopie (spin-polarized electron energy loss spectroscopy, kurz SPEELS) studiert werden. Im Rahmen dieser Arbeit konnten erste Spinwellendispersionen bei hohen Wellenvektoren in dünnen Filmen gemessen werden. Die Spinwellendispersionen konnten bis zur Oberflächen-Brillouinzonenengrenze verfolgt werden. Der Wellenvektorbereich der Spinwellen, die mit SPEELS untersucht wurden, liegt etwa zwei Größenordnungen über dem Bereich, in dem Spinwellen in dünnen Filmen bisher untersucht werden konnten. Andere Methoden, die die Untersuchung von Spinwellen mit hohen Wellenvektorüberträgen erlauben, benötigen viele Größenordnungen mehr an magnetischem Material. Der dünnste Film, an dem Spinwellenanregungen mit Hilfe von SPEELS untersucht wurden, war nur 2,5 atomare Lagen dick. Aufgrund des gemessenen hohen Signal- zu Rauschverhältnis ist zu erwarten, dass sogar atomar dünne magnetische Filme studiert werden können.

In dieser Arbeit wurden Spinwellen in den Sytemen fcc und hcp Co mit SPEELS untersucht. Generell zeigten die gemessenen Spinwellen ähnliche Eigenschaften in beiden Systemen.

In den SPEEL-Spektren wurden unter bestimmten Voraussetzungen sehr hohe Spinwellenintensitäten gemessen. Eine grobe Abschätzung zeigte, dass unter diesen Bedingungen ungefähr eins von 10^4 einfallenden Elektronen den Kristall verlässt, nachdem es eine Spinwelle erzeugt hat. Die Untersuchungen ergaben, dass die gemessene Spinwelleninstensität stark von der Energie der einfallenden Elektronen abhängt. Hohe Spinwelleninstensitäten wurden nur gemessen, wenn die Energie der einfallenden Elektronen kleiner als ungefähr 10 eV war. Diese Abhängigkeit der Anregungswahrscheinlichkeit von der Energie der einfallenden Elektronen kann über die Abhängigkeit des Streuprozesses von der Energie des einfallenden Elektrons erklärt werden. Die experimentellen Ergebnisse sind in dieser Hinsicht allerdings nur in qualitativer Übereinstimmung mit theoretischen Berechnungen [134,135]. Des Weiteren wurde ein Abfall der Spinwelleninstensität mit zunehmendem Wellenvektorübertrag beobachtet. Dieser Abfall kann ebenfalls durch den Streuprozess selbst erklärt werden. Ausserdem zeigten die Messungen unterschiedliche Spinwelleninstensitäten für verschiedene Streugeometrien.

Aus den SPEELS-Experimenten geht hervor, dass die gemessenen Spinwellen intrinsisch verbreitert sind. Dieses Verhalten wurde auch für Volumenspinwellen mit hohen Wellenvektoren beobachtet [59]. Eine solche Verbreiterung wird von nicht-adiabatischen Theorien aufgrund der starken Dämpfung der Spinwellen durch Stoner-Anregungen erwartet [20,54].

Die gemessene Spinwellendispersion in fcc- und hcp-Co-Filmen ist bis zu Wellenvektoren von ungefähr 0,8 Å^{-1} sehr ähnlich. Für höhere Wellenvektoren ergeben sich Un-

terschiede, die auf die unterschiedlichen Kristallstrukturen zurückzuführen sind. Für beide Kristallstrukturen ist die mit SPEELS gemessene Dispersion in erstaunlich guter Übereinstimmung mit der berechneten Dispersion der Oberflächenmode in einem nächsten-Nachbar-Heisenbergmodell. Durch das Anpassen der berechneten Dispersionskurven an die experimentellen Daten ergab sich ein Wert für das Produkt der Austauschkonstanten J und dem magnetischen Moment S von JS = 15±1 eV für fcc-Co und JS = 14,8±1 eV für hcp-Co. Im Rahmen des experimentellen Fehlers ergibt sich der selbe Werte für JS sowohl für beide untersuchten Kristallstrukturen als auch für alle untersuchten Schichtdicken (von 2,5 bis 8 atomaren Lagen für fcc-Co).

Aus den experimentellen Daten und ihrer Beschreibung durch das Heisenbergmodell, wie auch durch den Vergleich zu Literaturwerten ergibt sich, dass die mit SPEELS gemessenen Spinwellenspektren von Beiträgen durch Oberflächenspinwellen dominiert werden. Auch die gemessene Abhängigkeit der Spinwellenenergien von der Schichtdicke in fcc-Co kann in diesem Kontext verstanden werden. Durch ein einfaches phänomenologisches Modell wurde gezeigt, dass unter Berücksichtigung des Anregungsprozesses ein dominierendes Signal von Oberflächenspinwellen in den SPEEL-Spektren zu erwarten ist. Weiterführende theoretische Berechnungen lassen ähnliche Schlüsse zu [20].

Ein Vergleich der Ergebnisse, die durch SPEELS-Messungen und etablierte Messmethoden erhalten wurden, ist im Rahmen des Heisenbergmodells möglich. Im allgemeinen konnte eine gute Übereinstimmung zwischen den SPEELS-Daten und den Literaturwerten gefunden werden [59,127,128,138]. Hierbei wurden einerseits Oberfächen- mit Volumenspinwellen und andererseits Spinwellen mit um zwei Größenordnungen unterschiedlichen Wellenvektoren miteinander verglichen. Die Abweichungen sind erstaunlich klein, wenn man die Unterschiede in den experimentellen Methoden berücksichtigt.

Vergleicht man die SPEELS-Daten mit theoretische Berechnungen, so wird die gemessene Spinwellenenergie von der Theorie typischerweise überschätzt. Dies gilt insbesondere für Rechnugen, die für dünne Filme durchgeführt wurden. In diesen Fällen sagt die Theorie eine Erhöhung der Austauschkonstanten in der obersten Filmlage voraus [20,42,45,141], die experimentel nicht bestätigt werden konnte. Die Übereinstimmung der gemessenen Daten mit ab-initio-Berechnungen, die für Volumenkristalle durchgeführt wurden [40,43,142], ist recht gut, wenn man berücksichtigt, dass in diesen Rechnungen keine frei wählbaren Parameter enthalten waren. Diese Modelle basieren allerdings alle auf der adiabatischen Näherung und können dadurch die beobachtete Verbreiterung der Spinwellensignale nicht beschreiben. Mit Hilfe einer dynamischen Theorie, die über die adiabatische Näherung hinausgeht, haben Mills und Mitarbeiter die spektrale Zustandsdichte von Spinwellenanregung in dünnen Co-Filmen berechnet. Die Ergebnisse sind in guter qualitativer Übereinstimmung mit unseren gemessenen Daten. Die theoretischen Rechnungen basieren jedoch auf einer parametrisierten Beschreibung der zugrundeliegenden Bandstruktur. Es wurde gezeigt, dass durch kleine Veränderungen der Parameter die berechnete Dispersion stark beeinflusst werden kann [20]. Vollständige ab-initio-Rechnungen, die über die adiabatische Näherung hinaus gehen, wären hier wünschenswert.

Die vorgestellten Experimente eröffnen viele Möglichkeiten für zukünftige Untersuchungen. Andere magnetische Systeme haben Spinwellenenergien, die hoch genug sind, um

sie mit SPEELS zu untersuchen. Voraussetzung hierfür ist eine ähnlich hohe Spinwellenintensität wie in Co. Um die Spinpolarisation des einfallenden Elektronenstrahls ausnutzen zu können, ist lediglich eine definierte Magnetisierungsrichtung an der Oberfläche nötig. Folglich könnte es möglich sein, Spinwellen zum Beispiel auch an nicht-kompensierten Oberflächen von Antiferromagneten zu untersuchen. Ein vollständiges Experiment, in dem sowohl die Spinpolarisation des einfallenden Elektronenstrahls als auch die Spinrichtung der gestreuten Elektronen bestimmt wird, scheint möglich und befindet sich zur Zeit in Planung [133]. Aus unseren Ergebnissen läßt sich abschätzen, dass eine Untersuchung von Spinwellen auch mit "Standard"-EELS-Experimenten möglich sein könnte. Wegen der hohen Energieauflösung könnte man mit solchen EELS-Experimenten Spinwellen mit niedrigeren Energien untersuchen.

Wir hoffen, dass die hier vorgestellten Ergebnisse weitere experimentelle und theoretische Untersuchungen auf dem Gebiet der Spinwellen mit hoher Energie und hohem Impuls stimulieren werden.

Erklärung an Eides statt

Hiermit erkläre ich, die vorliegende Dissertation

Spin waves with high energy and momentum in ultra-thin Co-films studied by spin-polarized electron energy loss spectroscopy

selbständig und ohne fremde Hilfe verfasst und keine anderen als die von mir angegebenen Quellen und Hilfsmittel benutzt zu haben. Die den benutzten Werken wörtlich oder inhaltlich entnommenen Stellen sind als solche kenntlich gemacht.

Halle, den 26.8.04

Markus Etzkorn

Lebenslauf

Persönliche Daten:

Name:	Markus Etzkorn
Geburtsdatum:	07.11.1975
Geburtsort:	Bonn/Rhein
Familienstand:	ledig

Allgemeine Hochschulreife:

Juni 1995:	Abitur am Gymnasium Essen Überruhr

Wissenschaftlicher Werdegang:

Oktober 1996 bis Juni 2001:	Studium der Physik an der Ruhr-Universität Bochum
November 2000:	Stipendium der Ruth und Gerd Massenbergstiftung für hervorragende Leistung im Diplom
Juni 2000 bis Juni 2001:	Diplomarbeit mit dem Titel: *Austauschanisotropie an ferromagnetischen und antiferromagnetischen Schichten*
ab August 2001:	Doktorand am Max-Planck-Institut für Mikrostrukturphysik in Halle

Halle, den 26.8.04

Markus Etzkorn